Contents

List of Figures

List of Tables

Preface

This thesis is the culmination of my master degree in Physics. Throughout this journey the destination has never been completely clear although the field of experimental heavy ion physics has been ever present in it. When starting out some years ago it was initially with the intention of graduating in Astronomy, however gradually the focus shifted towards the field of heavy ion physics. One might postulate that I was the last one to notice in what direction I was heading.

I had my introduction to heavy ion physics in 2001; where Mads Toudal Frandsen, Signe Riemer-Sørensen, Christina Østerkryer von Holstein-Rathlou and I wrote the report "The Lifetime of the K-Meson" in the High Energy Heavy Ion (HEHI) group at the Niels Bohr Institute (NBI), which was received very well.

However this was not the end of heavy ion physics for me, since in 2004 Signe Riemer-Sørensen, Hans Hjersing Dalsgaard and I turned in our bachelor project "High p_T Suppression in Au-Au Collisions at RHIC", which was also very well received.

Hans Hjersing Dalsgaard and myself had not escaped the grasp of HEHI yet though, since we decided to continue in the field by studying "Nuclear Stopping in Au-Au Collisions at $\sqrt{s_{NN}} = 62.4\,\text{GeV}$". That work is currently being refined simultaneously with this thesis, and is very close to being submitted for a peer-reviewed journal.

Undertaking these projects in HEHI have been a pleasure, why it was an easy call, when the opportunity presented itself, to decide to write my master thesis in the group.

This thesis revolves around the concept of deuteron coalescence; where a neutron and a proton coalesce into a deuteron in the outer regions of a collision. Coalescence is of interest to physicists mainly since it can be used to estimate the size of the collision zone itself. In this work deuteron coalescence is probed by using data from the BRAHMS experiment, a part of the Relativistic Heavy Ion Collider, located at Brookhaven National Laboratory (BNL), USA. The unique design of the BRAHMS detector allows for identification of charged particles over a large range of rapidity.

Previous coalescence measurements have been restricted to the mid rapidity region, perpendicular to the beam direction. In this work coalescence is probed at both mid and forward rapidities for the first time.

The results presented here are preliminary, and as such, not official published BRAHMS results. Please contact the BRAHMS spokesman[1] and the author[2] before quoting the results.

---

[1]Flemming Videbæk, videbaek@bnl.gov
[2]cnygaard@nbi.dk

During the work on my thesis I have had the privilege of giving talks about this very topic at the Quark Matter 2006, Shanghai, China as well as at the School of Collective Dynamics, University of Berkeley, USA. Both these conferences have been a spectacular experience, which I hold dear.

The structure of this thesis is as follows: Chapter 1 starts out by introducing heavy ion physics in general and the previous results from the RHIC. Chapter 2 focuses on the theory behind deuteron coalescence. Moving further on, chapter 3 presents the experimental setup of the BRAHMS experiment. In chapter 4 the steps of the analysis is presented, before revealing the obtained results in chapter 5. At the end chapter 6 summarises the conclusions of this work.

This work would not have been possible if not for all the people who have helped and supported me along the way.

First off I would like to thank my supervisor Associate Professor Ian G. Bearden and Professor Jens Jørgen Gaardhøje for their guidance and advice throughout this work.

Furthermore special praise goes out to Christian Holm Christensen, Kristjan Gulbrandtsen, Truls M. Larsen and Catalin Ristea along with my two fellow master students Hans Hjersing Dalsgaard and Carsten Søgaard. They have been a joy to be around, helping and constantly giving valuable input.

Also a big thanks to Assistant Professor Michael Murray, University of Kansas, Associate Professor Hans Bøggild and Signe Riemer-Sørensen for reading through my thesis, assisting me with valuable inputs and correcting my English.

Outside the Physics community I owe a great debt to my family and friends, for their love and support all the way through and for having an incredible patience with me in the more stressful periods.

The work presented focuses on the 'old' era of heavy ion physics, that is the era of the RHIC, who have yielded tremendous insights in the inner workings of heavy ion collisions. However experimental heavy ion physics is approaching yet another very interesting era, which is very exciting for a young scientist to participate in. With the coming of the next generation accelerator, the Large Hadron Collider, endless possibilities arise once again to delve further in to the understanding of nuclei. I wish to end this introduction with a quote from renowned theoretician Michio Kaku[3] :

> "...Thus the yeoman work[4] in any science, and especially in physics, is done by the experimentalist, who must keep the theoreticians honest."

Michio Kaku [1]

Enjoy your reading!

---

[3]Kaku is known as the co-creator of string field theory.
[4]Old English expression for regular hard, loyal and often great work.

Copenhagen, July 2007

Casper Nygaard

Chapter 1

Heavy Ion Physics

Ultra-relativistic Heavy ion physics is devoted to studying the properties of matter under extreme temperatures and densities; for instance by colliding heavy ions at very high energies. It is a rapidly evolving field of study with theoreticians and experimentalists building a fuller and more detailed understanding of the physics of these collisions. This chapter presents first general (and fundamental) concepts regarding the field of heavy ion physics, and in the latter part some of the results obtained at the RHIC.

Heavy ion physics is in general a world full of acronyms, why a list of all used acronyms in this thesis can be found in appendix B. Furthermore it is customary to use natural units, in which the speed of light in vacuum (c) and Planck's constant (h) is set to unity. This convention is used throughout this work, unless specified.

1.1 The Standard Model

The standard model of particle physics is a quantum field theory describing three of the four known fundamental interactions between the elementary particles that constitute all matter.

Fermions

The building blocks of matter in the Standard Model are called fermions and have two subgroups; the quarks and leptons. There are six types (often called flavours) of quarks, called the up (u), down (d), charm (c), strange (s), bottom (b) and top (t) quark respectively. Likewise six types of leptons exists, namely the electron (e), electron neutrino (ν_e), muon (μ), muon neutrino (ν_μ), tau (τ) and the tau neutrino (ν_τ). For each quark/lepton there exist an anti-quark/lepton, having the same mass but opposite charges. Anti-particles are denoted like the associated particle, with the addition of a bar above the symbol, e.g. $\bar{u}$ for the anti-up quark.

The fermionic particles all have half-odd integer (e.g. $\frac{1}{2}, \frac{3}{2}, \ldots$) intrinsic spin and follow the Pauli exclusion principle. Furthermore the fermions are grouped in three generations; I, II and III. All the observed matter in the Universe consists solely of the light generation I fermions,

Fermions			
Generation	I	II	III
Quarks	u	c	t
	d	s	b
Leptons	e	μ	τ
	ν_e	ν_μ	ν_τ

Table 1.1: Overview of the fermions in the Standard Model. Each particle has an anti-particle associated with it.

since the higher (and heavier) generations are unstable and decays into lighter fermions. It has been shown by experiments at the Large Electron Positron (LEP) collider that precisely three generations of matter exist [2]. For an overview of the available fermions in the Standard Model see tab. 1.1. For a more detailed study on the various fermions consult [3].

Bosons

Besides the fermions the Standard Model includes bosons, which mediate the fundamental forces. All bosons have integer intrinsic spins, and thus do not follow the Pauli exclusion principle. Currently only three of the known four fundamental forces are incorporated into the Standard Model. The bosons mediating these forces are :

- $\mathbf{W^+, W^-, Z^0}$: These three bosons mediate the weak nuclear interaction between particles of different flavours. It has (as the only force) the ability to change a particle's flavour as seen in the β-decay, where a down quark in a neutron is transmuted to an up quark by emitting a W-boson.

- **Photon (γ) :** Photons mediate the electromagnetic force between electrically charged particles; i.e quarks, electrons, muons, tau, W^+, W^-. They are massless and are described by Quantum Electro-Dynamics (QED) [4]. In addition the photon and the three bosons of the weak interaction have been theoretically connected and can be treated as a single electroweak interaction.

- **Gluon (g) :** Gluons mediate the strong nuclear force between quarks of different colour charge (see sec. 1.2). Gluons are massless and are, contrary to photons and the bosons mediating the weak force, able to interact with themselves. The strong interaction is described by the theory of Quantum Chromo Dynamics (QCD) [5].

The fourth force, gravity, has not yet been incorporated successfully into the Standard Model, but a force carrier boson, the graviton, has been proposed [5], but has so far not been detected.

Finally the so-called Higgs boson ought to be mentioned. It is a hypothetical scalar particle, thus having spin zero (and thereby being a boson), introduced in the Standard Model to explain

Bosons			
Force	Electromagnetic	Weak nuclear	Strong Nuclear
Mediating boson	γ	W^+, W^-, Z^0	g

Table 1.2: Overview of the bosons in the Standard Model.

the masses of the other elementary particles and in particular the mass differences between the massless photon and the heavy W and Z bosons. Together with gluons the Higgs particle is the only bosons capable of self interaction. Currently the Higgs boson has not been observed, but hopes are that the upcoming Large Hadron Collider (LHC) experiments at CERN will be able to measure it in the coming year(s). An overview of the various bosons can be seen in tab. 1.1. Furthermore fig. 1.1 shows a schematic of the interplay between bosons and fermions in the Standard Model.
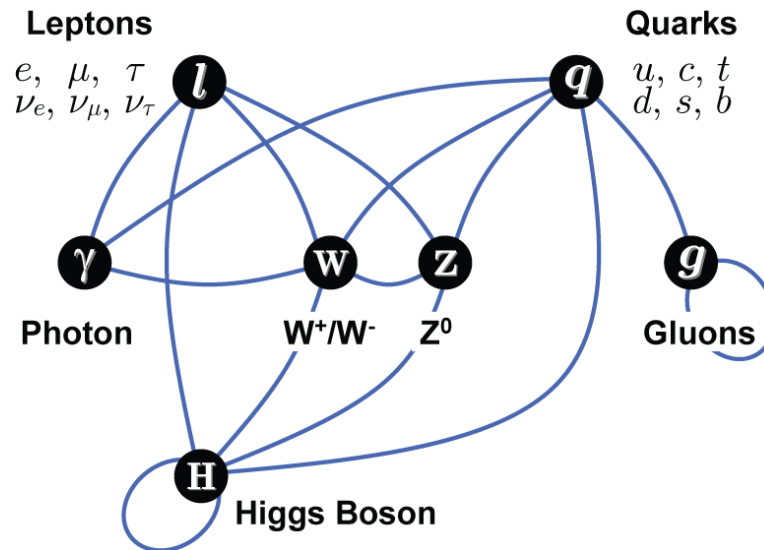
Figure 1.1: Illustration of the particles and the interactions between them as described in the Standard Model. The lines connecting particles show all possible interactions.

Composite Particles

All composite particles made up from quarks and/or anti-quarks are called hadrons. The hadrons are divided into two subgroups, the baryons and the mesons:

- **Baryons:** Baryons are made up of three quarks (or three anti-quarks), and are thus fermions themselves. The most well known baryons are the proton (uud) and the neutron

(udd). Other baryons relevant mentioning for later use in this thesis are the hyperons Λ (uds) and Σ (uus, uds, dds)[5], who decay into detectable protons. Hyperons are a baryonic subgroup having at least one strange quark, and no bottom or charm quarks.

- **Mesons:**   Mesons consists of a quark and an anti-quark, and are therefore bosons. For this thesis, the relevant mesons are the K-mesons (called kaons for short) and the π-mesons (called pions for short). Kaon is a common term for all mesons composed of an (anti-)strange quark and either (anti-)up/down (i.e. $s\bar{u}$, $s\bar{d}$, $\bar{s}u$ and $\bar{s}d$). Likewise pions consists of combinations of (anti-)up/down (i.e. $u\bar{u}$, $u\bar{d}$, $d\bar{d}$ and $d\bar{u}$).

1.2   Quantum Chromo Dynamics

QCD is the theory describing the strong nuclear interaction. All strongly interacting particles carry colour charge. There are three different colour charges for quarks, labelled red, green and blue. The colour charge have no real resemblance to macroscopic colours. The chosen labels merely use the analogy of three primary colours, adding up to be colour neutral (e.g. white 'neutral' light being composed of the primary colours red, green and blue.). Anti-quarks carry anti-colour charge, sometimes labelled anti-red, anti-green and anti-blue[6]. The gluons mediating the strong force carry both colour, and anti-colour. In total eight independent types of gluons exist. For more in depth descriptions see [6].

Mathematically several approaches exist for working with QCD. One of these is pertubative QCD (pQCD), an approach similar to the Feynman approach in QED, where interactions can be calculated as path integrals. Of the non-pertubative approaches the lattice QCD (lQCD) is the most established. lQCD describes space with a set of discrete points (the lattice), thus allowing one to numerically use QCD on supercomputers.

Confinement

According to QCD only colour neutral objects are allowed in nature. Thus for instance the three quarks of a baryon each carry different colour, making the composite particle colour neutral. Thus since individual quarks carry colour charge, they are not allowed outside composite particles; they are confined inside the hadrons. If one tries to separate two quarks by pulling them apart (which is essentially the case in scattering experiments), at one point it becomes energetically favourable to create new quark/anti-quark pairs, thereby producing new hadrons, but also confining the quarks inside these. This effect stems from the fact that the gluon itself carry colour charge, and thus can self-interact [7]. The quark-quark potential has the following form [8]:

---

[5]One might notice that the Σ^0 (uds) have the same quark composition as the Λ. It decays into rapidly into Λ by emitting γ radiation.

[6]and sometimes as complementary colours, cyan, magenta and yellow respectively.

$$V(r) \quad = \quad -\frac{4\alpha_s(r)\hbar c}{3r} + k \cdot r \tag{1.1}$$

Here k is the colour string tension (≈ 1 GeV/fm [7]) and $\alpha_s(r)$ is the strong interaction coupling constant. The coupling constant is not really a constant, since it diminishes for small values of r; a phenomenon known as asymptotic freedom. The quark-quark potential can be seen in fig. 1.2. At large values of r the linear gluon self interaction term becomes dominant. In this way the gluons act like a rubber band, storing more and more energy when stretched. This continues until sufficient energy is available to create the mentioned new quark/anti-quarks.
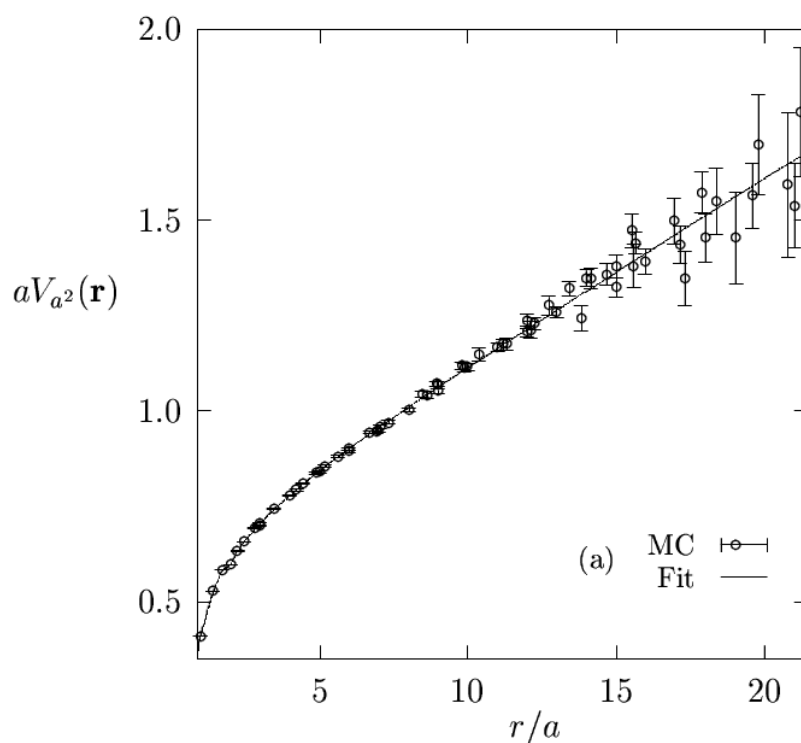
Figure 1.2: The quark-quark potential as a function of the distance between the quarks calculated from lQCD. *a* denotes the lattice constant, i.e. the distance between individual lattice points. Figure is taken from [9].

1.3   Quark Gluon Plasma

The concept of confinement holds true for normal temperatures and nuclear matter densities. A multitude of experiments have verified this in past, as no free quarks have ever been observed.

QCD however, predicts a phase of matter in which the quarks are not confined inside hadrons, called a Quark Gluon Plasma (QGP).

The main idea of a heavy ion physics QGP, sketched in fig. 1.3, is as follows. Consider a fixed volume, in which hadrons are filled. Since hadrons have a non-zero spatial volume [8], there exists a critical point where the hadrons completely fill out the volume. It is believed that adding more hadrons (or diminishing the volume) will then cause the hadronic structure to break down, creating a plasma of 'free' quarks and gluons. It is worth mentioning that the quarks/gluons are still confined inside the plasma, but not inside hadrons.
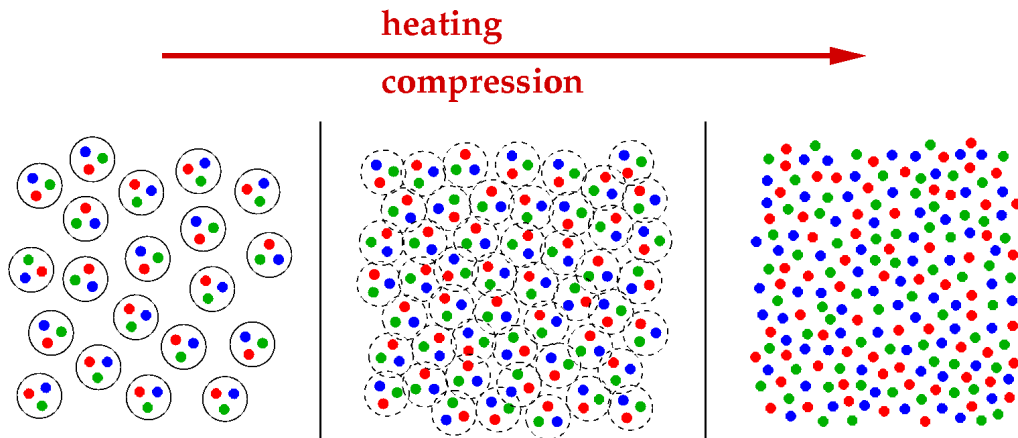
Figure 1.3: The formation of QGP through compression of matter. The hadronic structure breaks down and the quarks are deconfined inside a QGP. Figure taken from [10].

The term plasma suggests a gas-like behaviour with few interactions. Currently the matter created at the Relativistic Heavy Ion Collider (RHIC) at center-of-mass energy $\sqrt{s_{NN}} = 200\,\text{GeV}$ (see Appendix F for an introduction to collision energies) is believed to be a strongly interacting QGP, with more interactions, thus behaving more like a fluid [11].

The phase transition to QGP is predicted to happen at a critical temperature of $T_C = 173 \pm 3\,\text{MeV}$ [12] for a chemical potential of $\mu_B = 0$. An illustration of the QCD phase diagram can be seen in fig. 1.4.

It is obvious from fig. 1.4 that there are essentially two ways of reaching the QGP phase; by raising either the temperature or by raising the chemical potential. At the RHIC (and at the LHC) the former approach is used.

Cosmological Quark Gluon Plasma

Observational evidences in the field of cosmology coherently suggests that our Universe started as a mathematical singularity exploding spectacularly in a Big Bang. All the matter/energy of the Universe thus was concentrated in a volume of high density, temperature and pressure; the needed conditions for a QGP to have formed. As a consequence of the rapid expansion,
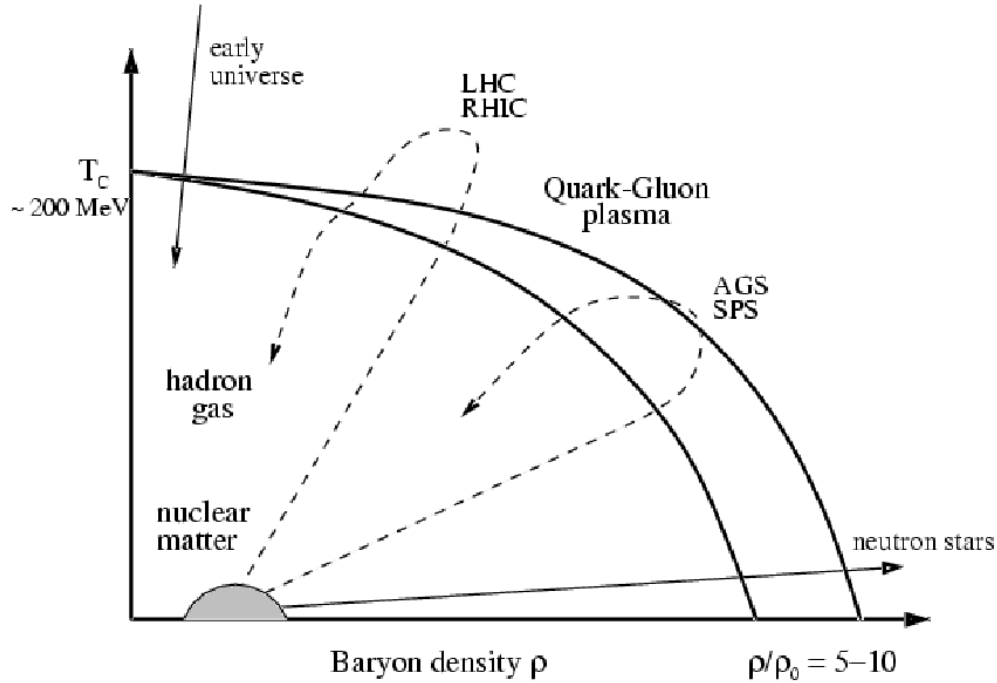
Figure 1.4: QCD Phase Diagram. The paths of several large experiments are shown. Furthermore the conditions in the early Universe, nuclear matter and neutron stars are indicated. It is worth mentioning that plotting the phase space as a function of baryon density or baryon-chemical potential (as used in the text) makes no difference, since the two are thermodynamically conjugate. Figure taken from [10].

the Universe cooled down quickly. At approximately $1\,\mu s$ after the Big Bang the Universe is believed to have been in a QGP phase before undergoing hadronic freeze out.

The cosmological QGP and the QGP seen in heavy ion collisions are not believed to be identical though. Firstly the cosmological QGP existed for a time scale of 10^{-6} s whereas the observed heavy ion QGP have a lifetime of the order of 10^{-23} s [13]. Secondly the baryon densities of the early Universe is thought to be of the order $N_b/N \sim 10^{-10}$ compared to the $N_b/N \sim 10^{-1}$ in heavy ion collisions [13]. N includes all particles, i.e. hadrons, leptons, photons etc.

In the heavy ion collision QGP the baryonic density is sufficiently large, that strong interactions between quarks and gluons will happen regularly; i.e. the medium is strongly interacting. This is believed to be in contrast to the situation in the early Universe where the scarcity of baryons makes strong interactions improbable. Furthermore the lifetime of the cosmological QGP certainly allows it to reach thermal equilibrium at some point. For the heavy ion collision QGP this is still a topic of dispute.

1.4   Relevant Variables

This section introduces kinematic variables and concepts which are fundamental to heavy ion physics in general and to the BRAHMS experiment specifically. We start out by looking at the coordinate systems in the BRAHMS experiment; the global and local systems. The global coordinate system (XYZ) is centered around the collision itself. The Z-axis follows the beam line, and the X-axis always points towards the center of the accelerator ring, thus leaving the Y-axis to point vertically up-wards. Local coordinate systems (X'Y'Z') exists in each sub detector, with the Z'-axis pointing away from the original collision. The Y'-axis of the local system is parallel to the Y-axis of the global system. A sketch of these systems is found in fig. 1.5.
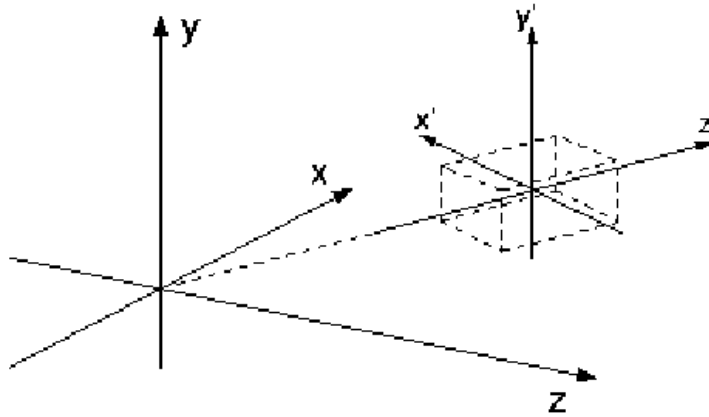
Figure 1.5: Sketch of the coordinate systems used in the BRAHMS experiment. Collisions occur at (0,0,0) in the global XYZ system. The Z-axis follows the beam line, and the X-axis point to the center of the accelerator ring. Each sub-detector have a local coordinate system X'Y'Z' defined.

The momenta of the created particles, is split into a longitudinal component, p_z, along the beam-line and a transverse momentum component, p_T, orthogonal to the beam. The transverse momentum, illustrated in fig. 1.6, is given by:

$$p_T \;=\; \sqrt{p_x^2 + p_y^2} \tag{1.2}$$

Similarly the transverse mass is defined as:

$$m_T \;=\; \sqrt{m^2 + p_T^2} \tag{1.3}$$

Both the transverse mass and momentum are Lorentz invariant making them excellent variables in relativistic systems. Instead of using longitudinal momentum it is common practice to use the rapidity, y, which is defined as:
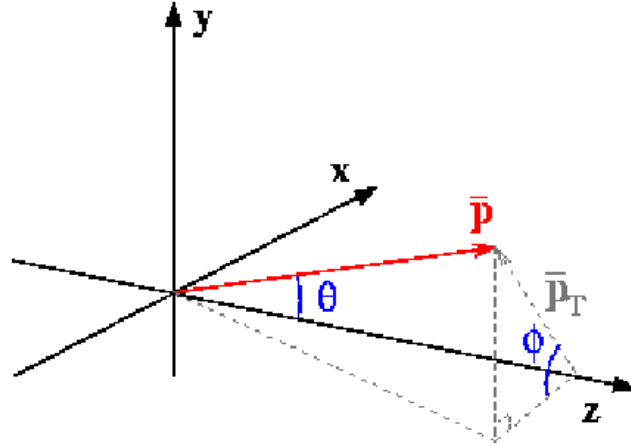
Figure 1.6: Definition of the transverse momentum and the angles θ and ϕ.

$$y = \frac{1}{2}\ln\left(\frac{E+p_z}{E-p_z}\right) \tag{1.4}$$

E is the particle energy, $E = p^2 + m^2$. The rapidity is useful as a longitudinal variable compared to longitudinal momentum, since rapidity differences are Lorentz invariant (see Appendix G.1 for more detail). If the mass is unknown the pseudorapidity, η, is a very useful quantity:

$$\eta = -\ln(\tan(\theta/2)) \tag{1.5}$$

θ denotes the polar angle between the momentum vector, p, and the beam axis, as seen in fig. 1.6. In the case where $\mid p \mid \gg m$ the rapidity reduces to the pseudorapidity:

$$
\begin{aligned}
y &= \frac{1}{2}\ln\left(\frac{E+p_z}{E-p_z}\right) \\
&\approx \frac{1}{2}\ln\left(\frac{p+p_z}{p-p_z}\right) \\
&= \frac{1}{2}\ln\left(\frac{1+\cos\theta}{1-\cos\theta}\right) \\
&= -\ln(\tan(\theta/2)) \tag{1.6}
\end{aligned}
$$

Here it has been used that $E \sim p$ and that $p_z = p \cdot \cos(\theta)$.

For studying the particle production it is useful to express the invariant cross section $E\frac{d^3\sigma}{dp^3}$ in terms of rapidity, transverse momentum and the azimuthal angle, ϕ, which is defined such that $p_x = p_T\cos(\phi)$ and $p_y = p_T\sin(\phi)$. We start out by using the definition of $\cosh(y)$ together with eq. 1.4 and $E^2 = m_T^2 + p_z^2$:

$$
\begin{aligned}
\cosh(y) &= \frac{1}{2}(e^y + e^{-y}) \\
&= \frac{1}{2}\left(\sqrt{\frac{E+p_z}{E-p_z}} + \sqrt{\frac{E-p_z}{E+p_z}}\right) \\
&= \frac{1}{2}\left(\frac{E+p_z+E-p_z}{\sqrt{E^2-p_T^2}}\right) \\
&= \frac{E}{m_T}
\end{aligned} \tag{1.7}
$$

Thus the energy if found to be $E = m_T \cosh(y)$. In a similar fashion it turns out that the longitudinal momentum can be written as: $p_z = m_t \sinh(y)$.

With these quantities in hand the Jacobian is calculated:

$$
\begin{aligned}
\frac{\partial(p_x p_y p_z)}{\partial(y p_T \phi)} &\equiv
\begin{vmatrix}
\partial p_x/\partial y & \partial p_x/\partial p_T & \partial p_x/\partial \phi \\
\partial p_y/\partial y & \partial p_y/\partial p_T & \partial p_y/\partial \phi \\
\partial p_z/\partial y & \partial p_z/\partial p_T & \partial p_z/\partial \phi
\end{vmatrix} \\
&=
\begin{vmatrix}
0 & \cos(\phi) & -p_T \sin(\phi) \\
0 & \sin(\phi) & p_T \cos(\phi) \\
E & \partial p_z/\partial p_T & \partial p_z/\partial \phi
\end{vmatrix} \\
&= E \cdot p_T
\end{aligned} \tag{1.8}
$$

Using the Jacobian it is found that the invariant cross section can be written as:

$$
E\frac{d^3\sigma}{dp^3} = \frac{d^2\sigma}{2\pi p_T \partial p_T \partial y} \tag{1.9}
$$

Here the integration over the azimuthal angle has been done, yielding the factor of 2π. The right hand side of eq. 1.9, called the invariant spectrum, is a very important observable in heavy ion physics, and it is also the core measurement of this work. Sometimes it is presented in the form $\frac{d^2N}{2\pi N_{event} p_T \partial p_T \partial y}$, where N is the measured number of a given particle species, and N_{event} is the number of events.

All results presented later on will be derived from invariant spectra of (anti-)protons and (anti-)deuterons.

1.5   Relativistic Heavy Ion Collisions

In the following sections an introduction to the central pictures and concepts of relativistic heavy ion collisions will be given.

In Figure 1.7 an illustration of a relativistic collision is shown as seen from the Center-of-Mass frame of the nuclei. Each nucleus is highly Lorentz contracted along its direction of motion.
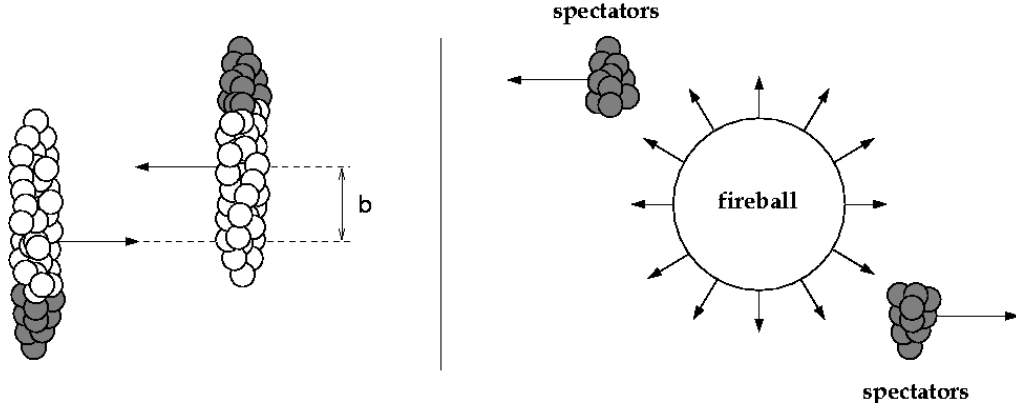
Figure 1.7: Schematic illustration of a relativistic heavy ion collision. The participant nucleons of the overlap region between the colliding nuclei form the high density fireball, whereas the rest of the nucleons continues unaffected as spectators. Picture taken from [52].

Participants and Spectators

The nucleons directly involved in the collision, called participants, interact strongly giving rise to a high density volume, known as the fireball. Nucleons outside the overlapping region of the two nuclei are called spectators. They are unaffected by the collision except for Coulomb-interactions and they retain their initial momentum, flying away from the fireball.

Figure 1.7 also introduces the impact parameter, b, which is the transverse distance between the centers of the two nuclei. A large impact parameter hence corresponds to a peripheral collision, where a small region of the nuclei overlap, whereas a small impact parameter gives a central collision with a large overlapping region.

As it is practically impossible to measure the impact parameter directly an experimental technique is used to distinguish collisions into classes of centrality. This is done based on the multiplicity of the events so that the collisions with highest particle production are defined as most central. In this work only 0-20 % central collisions have been analysed, meaning that these are the collisions with the highest multiplicities accounting for the top 20 % of the total integrated multiplicity.

The impact parameter is correlated to the centrality of the collision in the following way:

$$c \;=\; \frac{\int_0^{b_c} \frac{d\sigma_{in}(b')}{db'} db'}{\sigma_{in}} \tag{1.10}$$

Here $\sigma_{in}, \frac{d\sigma_{in}(b')}{db'}$ and b_c are the total inelastic nuclear reaction cross section, the differential cross section and a cut-off in the impact parameter respectively. Thus the centrality, c, denotes the probability that a collision occurs with a impact parameter of $b \leq b_c$. For a solid sphere

$\frac{d\sigma_{in}(b)}{db} = 2\pi b db$ and thereby under the assumption that nuclei are identical and spherical the centrality becomes:

$$
\begin{aligned}
c &= \frac{\int_0^{b_c} 2\pi b db}{\int_0^{2R} 2\pi b db} \\
&= \frac{b_c{}^2}{4R^2}
\end{aligned}
\tag{1.11}
$$

Here R denotes the radius of the nuclei. Consisting of 197 nucleons, Au is found to have $R = R_0 \cdot A^{1/3} = 1.2 \cdot 197^{1/3}\text{fm} = 7.0\text{fm}$. R_0 is found to be $1.2\,\text{fm}$ [14]. Thus a centrality of 0-20% corresponds to an impact parameter of less than 6.3 fm.

The impact parameter and the number of participants in the collision are of course directly related. Their relation can be estimated using the so-called Glauber model. A short introduction to it can be found in Appendix G.

1.5.1   The Bjorken Picture

A very important contribution to heavy ion physics is a paper from 1983 by Bjorken [15], which deals with a hydrodynamical description of the central rapidity region in heavy ion collisions. The description relies on four important assumptions on collisions between nuclei with nucleon number A:

- **Boost invariance :** The rapidity densities $\frac{dN}{dy}$ are independent of rapidity for at least a few units of rapidity around mid-rapidity in p+p and p+A collisions, from which it is assumed that the same is true for A+A collisions.

- **Transparency :** The nuclei interpenetrates in the A+A collision and the central plateau is formed through particle production from the breaking of colour strings. The fragments of the original nuclei end up some units of rapidity from mid-rapidity. In Lorentz frames with velocities close to the mid-rapidity frame, the nuclei look like receding flat pancakes.

- **Transverse expansion :** The transverse expansion of the source can be ignored for most of the collisions because of the large initial transverse scale of the source compared to its longitudinal scale. This is only true for central collisions and reduces the problem to a 2-dimensional problem in the coordinates z and t.

- **Thermalization :** At some early time, assumed to be of the order of the characteristic hadronic time scale $t \sim 1$ fm/c, the system thermalises and hydrodynamics governs the evolution and expansion of the source.

The proper time τ, which if assumed that at t=0 the longitudinal extension, z, is negligible, is given by:

$$\tau \equiv \frac{t}{\gamma} \;=\; \sqrt{t^2(1 - \frac{z^2}{t^2})}$$
$$=\; \sqrt{t^2 - z^2} \tag{1.12}$$

In a space-time diagram this yields hyperbolas of constant energy densities, which can be used to distinguish different evolutionary phases in heavy ion collisions. In fig. 1.8 a sketch of the space-time evolution of a central collision is shown.
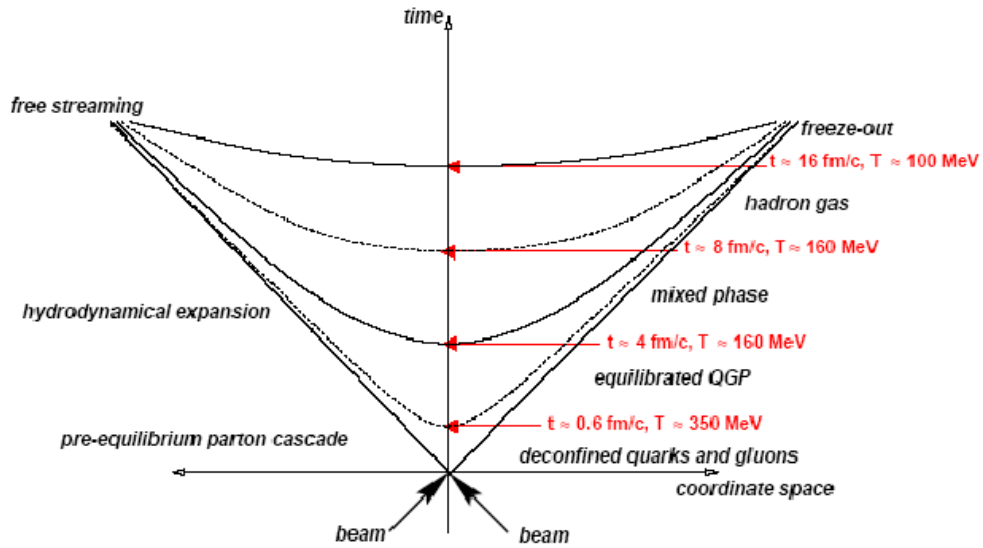
Figure 1.8: Proposed space-time evolution of a heavy ion collision. Quarks and gluon are at first deconfined in a QGP which thermalises; eventually the hadrons freeze out and streams away freely. Picture taken from [16].

In the Bjorken picture the incoming nuclei are transparent to each other as mentioned, allowing them to interpenetrate without loosing much of their initial kinetic energy. However, upon doing so they leave a highly excited colour field between them, in which particle production take place due to the breaking of colour strings. The concept of transparency is illustrated in fig. 1.9.

1.5.2 The Landau Picture

The opposite of the transparent Bjorken picture is a picture where full nuclear stopping is assumed. This picture was proposed by Landau in [17]. Landau argued that:
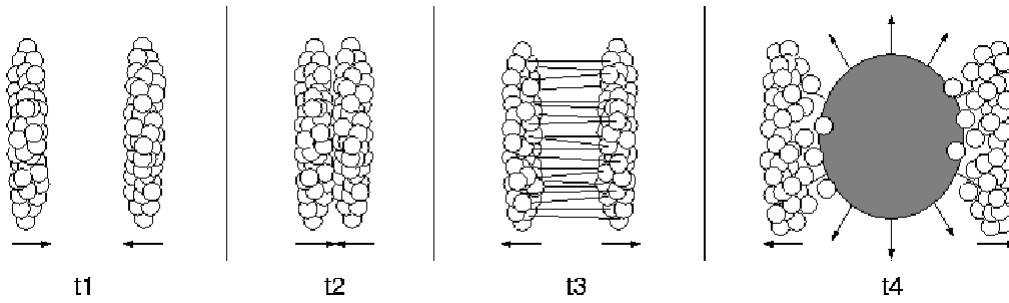
Figure 1.9: Simplistic view of a collision in the transparent picture. Picture taken from [10].
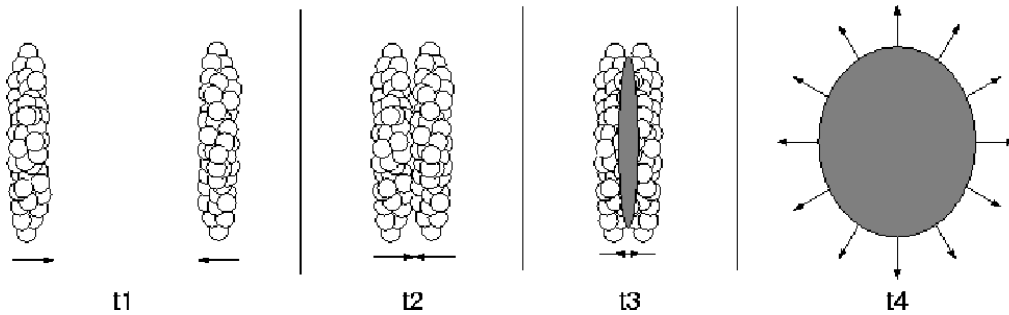
Figure 1.10: Simplistic view of a collision in the stopping picture. Picture taken from [10].

- **Full stopping :** The incoming nuclei are fully stopped when hitting each other. All their initial kinetic energy is deposited in the fireball.

- **Hydrodynamics :** Particles in the fireball have small mean free paths, so that fireball can be treated as an ideal fluid in the sense that it is non-viscous and non-heat conducting.

- **Adiabatic expansion :** The fluid expands adiabatically, i.e. the entropy is constant.

A collision in accordance with the Landau picture is illustrated in fig. 1.10.

These two extreme pictures corresponds to very different macroscopic physical phenomena. The transparent Bjorken picture is reminiscent of the early Universe, with very high temperature and low baryo-chemical potential, μ_B. In the other end of the scale, Landau's stopping picture is reminiscent of the conditions inside stellar objects like neutron stars, with large μ_B and relatively low temperature. At RHIC it is found by nuclear stopping measurements, that the higher the collision energy is, the more transparent the collision is.

1.6 Previous Results from RHIC

During the years of operation, the RHIC have yielded extensive understanding of heavy ion collisions, and in particular of the possible formation of a QGP. In this section some of the experimental highlights from the RHIC are presented.

1.6.1 High p_T Suppression

One of the first indications of a QGP was that high p_T particles in Au-Au collisions were suppressed compared to p-p collisions. Experimentally this is measured by the nuclear modification factor:

$$R_{AuAu} \equiv \frac{d^2N/dp_T d\eta_{AuAu}}{N_{bin} d^2N/dp_T d\eta_{pp}} \tag{1.13}$$

where R_{AuAu} is the transverse particle production of Au+Au collisions relative to p+p collisions scaled by the number of binary collisions, N_{bin}. In fig. 1.11 measurements of R_{AuAu} from the BRAHMS experiment is shown [18]. It is seen that for Au-Au collisions at $p_T > 2\,\text{GeV/c}$ there is a large suppression. It is believed that this effect comes from coloured objects interacting with the medium, by emitting gluons as bremsstrahlung [11]. In comparison it is seen that d-Au collisions are not suppressed, in accordance with expectations.

In fig. 1.12 another measurement of R_{AuAu} is shown; this time from the PHENIX experiment [19]. It was found that also π^0 and η mesons are highly suppressed, but the most exciting part of fig. 1.12 is that direct photons are not suppressed. Since they only couple to the electromagnetic force it shows that the medium suppressing high p_T particles is in fact strongly interacting, but not electromagnetically interacting.

The measurements from R_{AuAu} are not the 'smoking gun' of a QGP, but they are indeed a strong indication of one.

1.6.2 Jet Quenching

Another indication of the presence of a QGP is the measurement of dihadron azimuthal correlations from STAR [20, 21], which is shown in fig. 1.13. In short dihadron azimuthal correlation revolves around observing jets of high momentum particles near the fireball edge. One of the jets are emitted away from the fireball, while the other is emitted in the opposite direction through the fireball. In p-p and d-Au collisions enhancements are measured at $\Delta\phi \sim 0$ and $\Delta\phi \sim \pi$; the directions of each jet. However in Au-Au collisions only the first jet is observed. The jet traversing the longest distance (through the medium) is not detected, supposedly since it has interacted strongly with the medium; it has been 'quenched'; i.e. lost its energy by gluon emission in the medium.
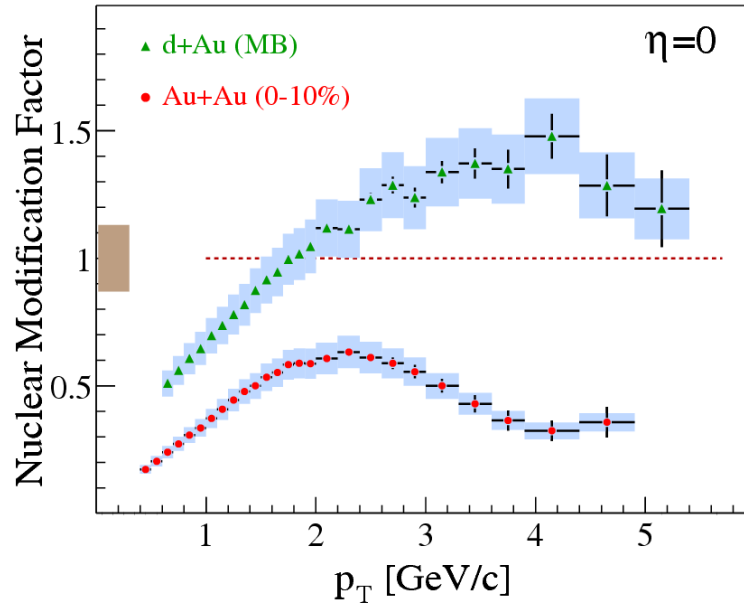
Figure 1.11: Nuclear modification factor for charged hadrons measured by BRAHMS[18]. It is found that charged hadrons in central Au-Au collisions are highly suppressed at high p_T, whereas it is not the case in d-Au collisions. The enhancement, labelled Cronin enhancement, seen in d-Au is believed to stem from multiple scatterings prior to the hard scatterings that produce the high p_T hadrons [22].

1.6.3 Elliptic Flow

The collective motion of particles inside the dense fire ball region of heavy ion collisions is called flow. In general three major types of flow are considered; directed, elliptic and radial flow. Both directed and elliptic flow becomes more profound the more peripheral the collisions is, since in such collisions the initial spatial asymmetry, due to the overlapping nuclei, is more pronounced, causing matter to bounce off (directed) or be squeezed out (elliptic) in certain directions[23]. In completely central collisions the collision symmetry cancels out these effects.

The flow, as proposed by Voloshin and Zhang [24], can be quantified by the harmonic Fourier coefficients, v_n, in the azimuthal distribution of particles relative to the reaction plane (for an illustration of the reaction plane consult Appendix E):

$$E\frac{d^3N}{d^3p} = \frac{1}{2\pi}\frac{d^2N}{p_T dp_T dy}(1 + \sum_{n=1}^{\infty} 2v_n \cos(n(\phi - \Psi_r))) \tag{1.14}$$

Here Ψ_r is the azimuthal angle of the reaction plane. The 2nd harmonic, v_2, is called the elliptic flow and describes the symmetric flow of particles both parallel and perpendicular to the impact parameter [25]. Typically v_2 is the largest of the harmonic coefficients. In fig. 1.14 measurements of the elliptical flow scaled with the number of quark degrees of freedom can be seen [26]. Large elliptic flows (as seen in the figure) requires a high number of interactions in the fireball region, since the asymmetry required for a non-zero v_2 would vanish for a non-interacting system [27]. On basis of the RHIC data it is concluded in [28] that the measured
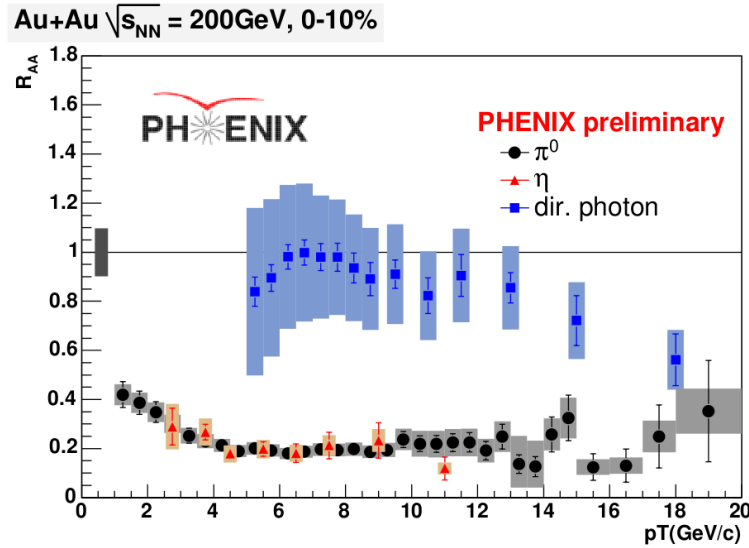
Figure 1.12: Nuclear modification factor for π^0, η and direct photons in PHENIX [19]. It is seen that the photons are not suppressed, indicating that the medium is not electromagnetically interacting, but instead only strongly interacting.
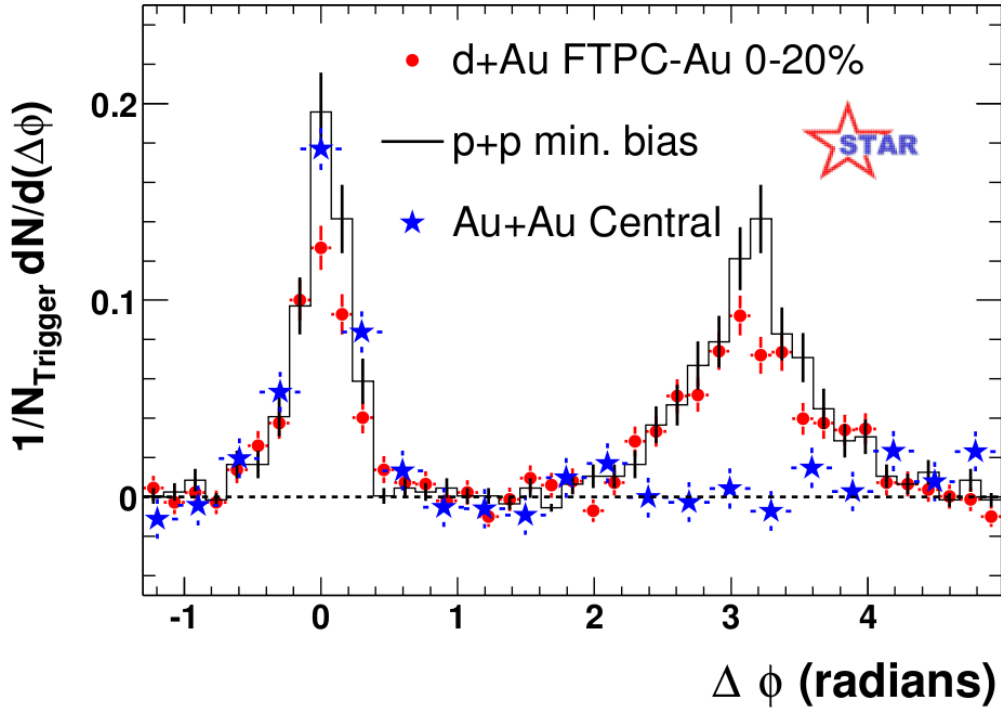
Figure 1.13: Jet Quenching measured at STAR [20, 21]. It is found in Au-Au col-
lisions, that the jet travelling the shortest path through the medium
($\Delta\phi \sim 0$) is enhanced compared to the jet travelling through the longest
path in the medium ($\Delta\phi \sim \pi$). This in not seen in d-Au and p-p colli-
sions, and is interpreted as the existence of a strongly interacting QGP
in Au-Au collisions.

elliptic flow only can be explained if the system is thermalized in less than $1\,\text{fm/c}$; a time
where the density of the fireball is an order of magnitude higher than the critical value for
quark deconfinement,why it is concluded that a QGP is indeed created.

1.6.4   Particle Ratios

Major work have been done at all four RHIC experiments at determining the ratios between
various particles, to help in understanding the particle production mechanism/conditions in
heavy ion collisions. In fig. 1.15, published by STAR [29], ratios of p_T-integrated mid-rapidity
yields for different hadron species in central Au+Au collisions at $\sqrt{s_{NN}} = 200\,\text{GeV}$ is shown.
The ratios are compared to a statistical model fit (horizontal lines), where chemical and
thermal equilibrium is required. As seen the model describes the measured ratios very well.
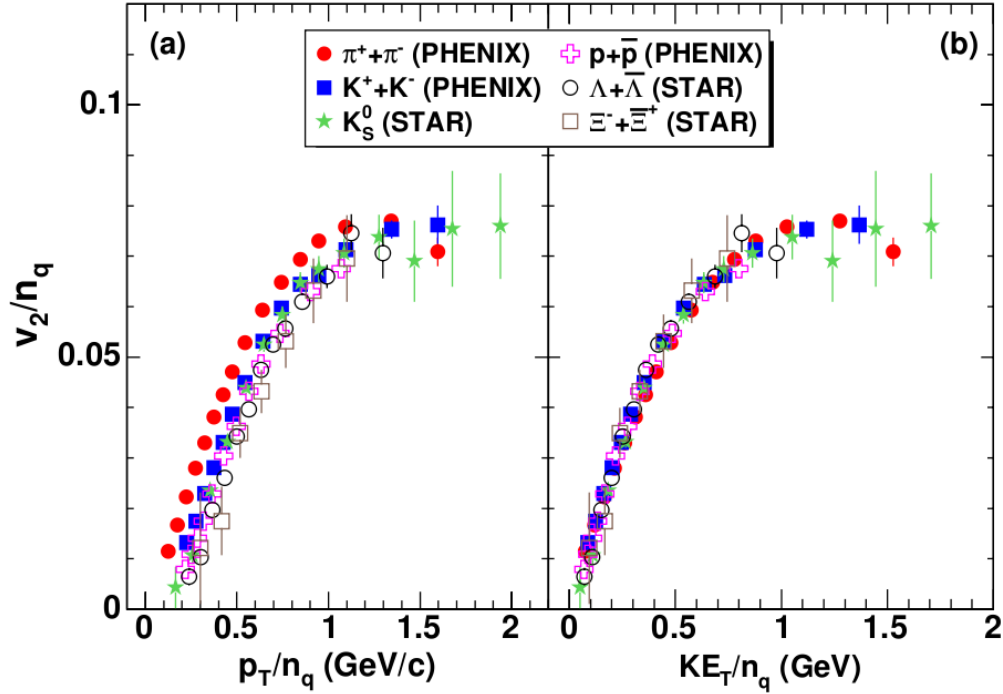
Figure 1.14: Measurements of the elliptic flow scaled with the number of quark de-
grees of freedom. It is found that the very large elliptic flow indicate
a thermalized fireball region, in which a QGP is formed. Figure taken
from [26].

1.6.5   Nuclear Stopping

Nuclear Stopping investigate how much kinetic energy is lost during a collision; e.g. how much
the participating nuclei are stopped. An experimental measure for the stopping was given by
Videbaek and Hansen [30]. They defined the stopping as the average rapidity loss:

$$\langle \delta y \rangle = |y_b - \langle y \rangle| \tag{1.15}$$

where y_b is the beam rapidity of the colliding nuclei. $\langle y \rangle$ denotes the average baryon rapidity
after the collision, given in symmetric collisions as:

$$\langle y \rangle = \frac{2}{N_{part}} \int_0^{y_b} y \frac{dN_{B-\bar{B}}}{dy} dy \tag{1.16}$$

N_{part} is the number of nucleons directly participating in the collision and $\frac{dN_{B-\bar{B}}}{dy}$ is the yield
of net-baryons ($N_{B-\bar{B}} = N_B - N_{\bar{B}}$) per rapidity.   In fig. 1.16 the measured net-baryon
distribution from several experiments is shown [31]. In fig. 1.17 the average rapidity loss as
a function of energy is shown. An important stopping result from RHIC is that the linear
scaling seen at pre-RHIC energies is broken at RHIC.
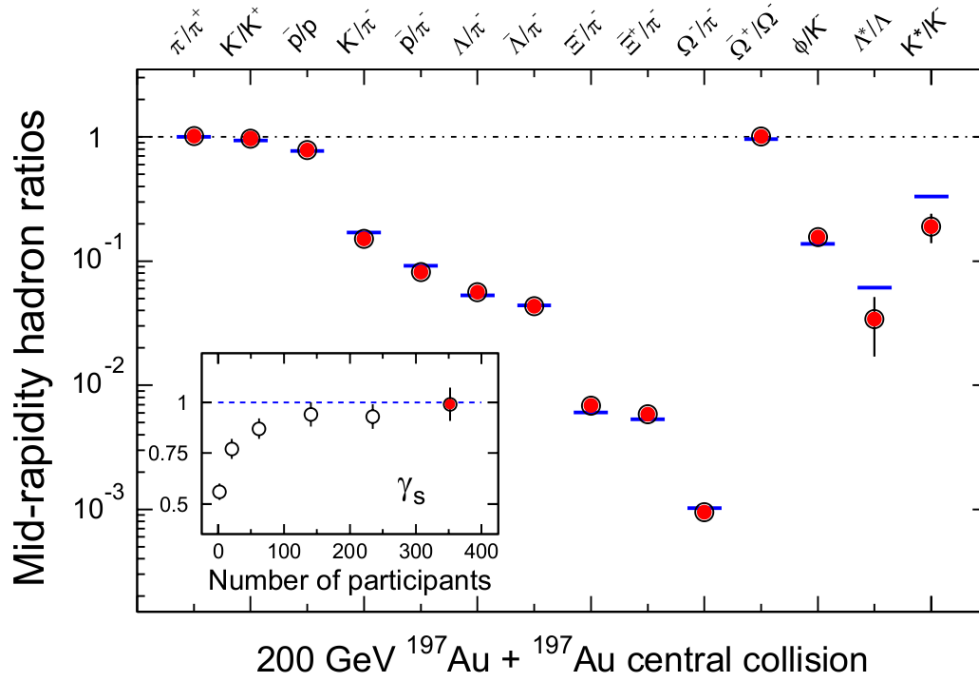
Figure 1.15: Ratios of various hadron species yields fitted to a statistical model, requiring chemical and thermal equilibrium. Good agreement is found, suggesting that the fireball is indeed equilibrated early on [29]. This is also illustrated in the insert, showing the so-called non-equilibrium parameter, γ_s, as a function of participants. It approaches unity (=equilibrium) for central collisions.

On a final note it is also seen that as $\sqrt{s_{NN}}$ rises the central rapidity region becomes very net-baryon poor, showing that increasing transparency is achieved. As mentioned in sec. 1.5.2 this is reminiscent of the conditions in the early Universe, which also motivates why heavy ion collisions are often referred to as "mini-Big Bangs".
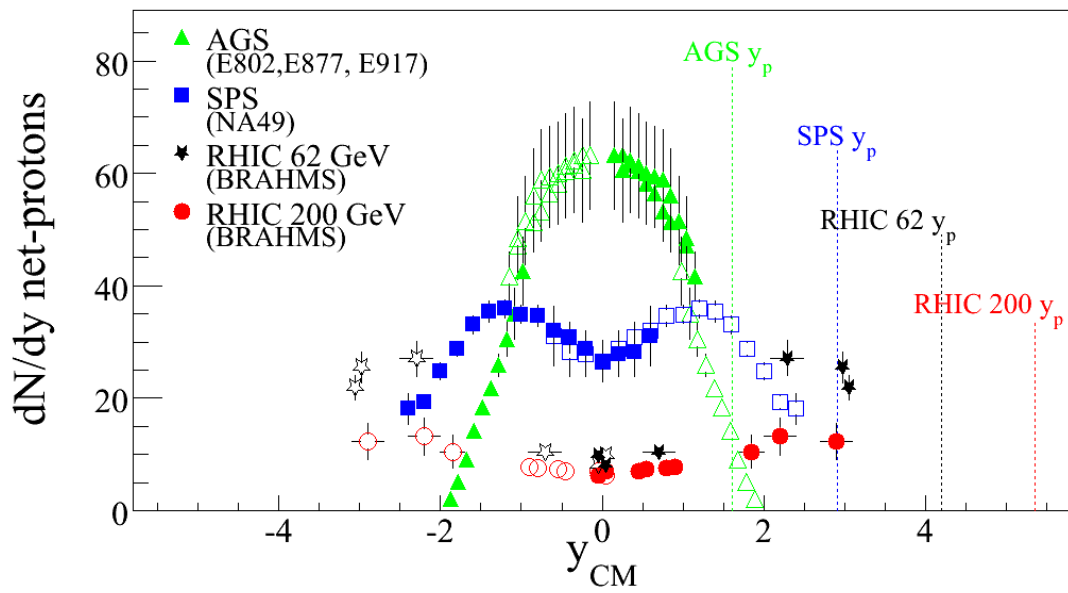
Figure 1.16: The net-proton distribution from several experiments at different energies. It is found that as the collision energy rises, the collision becomes increasingly transparent. The figure is from [31], with the addition of the BRAHMS 62.4 GeV distribution pending for publication [32].
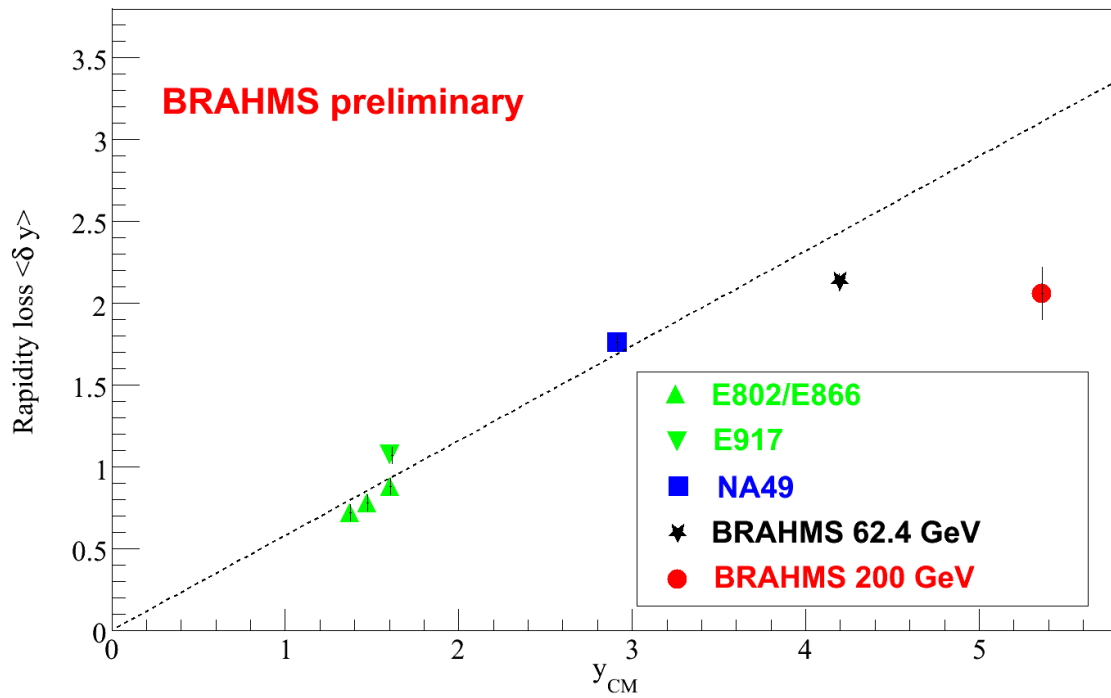
Figure 1.17: The average rapidity loss as a function of collision energy. The figure is from [31], with the addition of the BRAHMS 62.4 GeV distribution pending for publication [32]. The linear scaling seen pre-RHIC (dashed line) is broken at RHIC.

Chapter 2

Coalescence

The formation of deuterons in heavy ion collisions occurs through a process called coalescence. The idea is that when the constituent nucleons are sufficiently close in momentum space they coalesce into a new particle. Deuterons are created in this way by the process $p + n + \pi \rightarrow d + (\pi \text{ or } \gamma)$, where a proton and a neutron coalesce into a deuteron and a pion or photon carry off the excess energy and momentum. Since the deuteron is a very loosely bound system with a binding energy of merely 2.2 MeV, the coalescence must take place late in the heavy ion collision, when the energy density has declined sufficiently for deuterons to survive. Thus deuteron coalescence take place in the colder outer spatial region at the time scale of kinetic freeze-out.

Historically the idea of coalescence was founded by Butler and Pearson in their 1963 paper on deuteron production in proton-nucleus collisions [33]. In that paper they found that the amount of measured deuterons could not be accounted for by traditional formation mechanisms (nucleon-nucleon collisions), hence proposing that the extra deuterons were formed by neutrons and protons in the cascade inside the collisions. Schwarzschild and Zupančič followed up at the same time by arguing that the deuteron momentum distribution should be proportional to the product of the proton and neutron momentum distributions [34]. Hence for Lorentz invariant distributions:

$$\gamma \frac{d^3 N_d}{dp^3} \propto \left(\gamma \frac{d^3 N_p}{dp_p^3} \right) \left(\gamma \frac{d^3 N_n}{dp_n^3} \right) \tag{2.1}$$

The subscripts denote deuterons, protons and neutrons respectively, and the proportionality constant is the coalescence parameter. γ is given by $\gamma = E/m$, with E and m being the particle energy and mass respectively. For deuterons the coalescence parameter, B_2, used throughout this thesis is defined as:

$$\left(E_d \frac{d^3 N_d}{dp_d^3} \right) = B_2 \cdot \left(E_p \frac{d^3 N_p}{dp_p^3} \right)^2 \tag{2.2}$$

Here $p_d = 2p_p$ and it is assumed that

$$\left(E_n \frac{d^3 N_n}{dp_n^3} \right) = R_{np} \cdot \left(E_p \frac{d^3 N_p}{dp_p^3} \right) \tag{2.3}$$

with the ratio between neutrons and protons in the source being R_{np}. Equation 2.2 can be generalised to clusters of mass A as:

$$\left(E_A \frac{d^3 N_A}{dp_A^3} \right) = B_A \cdot \left(E_p \frac{d^3 N_p}{dp_p^3} \right)^A \tag{2.4}$$

with $p_A = A \cdot p$ denoting the total momentum of the cluster.

In equations 2.2 and 2.4 the neutron contribution is eliminated by setting R_{np} to unity. This is necessary since the BRAHMS experiment is unable to measure neutral particles. For a more elaborate treatment this should be taken into account.

The coalescence parameter is an experimentally measurable quantity, which can be related to the properties of the emitting source via models. Some of these models will be presented in the following sections.

2.1   Simple Coalescence Model

In this section the outline of a simple, yet very descriptive model, will be presented. For more details see [35]. The model states that the deuteron phase space density is proportional to the proton density times the probability of finding a neutron within a small sphere of radius, p_0, around the proton momentum:

$$\left(\gamma \frac{d^3 N_d}{dp_d^3} \right) = \frac{4\pi}{3} p_0^3 \cdot \left(\gamma \frac{d^3 N_n}{dp_n^3} \right) \left(\gamma \frac{d^3 N_p}{dp_p^3} \right) \tag{2.5}$$

Consider a small sphere with radius p_0. The probability, P, of finding a single nucleon in this sphere is given by

$$P = \frac{1}{M} \frac{4\pi}{3} p_0^3 \left(\gamma \frac{d^3 N_N}{dp_N^3} \right), \tag{2.6}$$

where M denotes the mean nucleon multiplicity. Thus the probability of finding A nucleons of M in the sphere is given binomially as

$$P_M(A) = \binom{M}{A} P^A (1 - P)^{M-A} \tag{2.7}$$

Now assume that the mean nucleon multiplicity is high ($M \gg 1$), the mean number of nucleons within the sphere is low ($MP \ll 1$) and finally that the forming cluster is small ($A \ll M$) then eq. 2.7 becomes:

$$P_M(A) = \frac{1}{A!} (MP)^A \tag{2.8}$$

Using eq. 2.6 and 2.7 while assuming that the probability of finding one cluster of A nucleons is equal to the probability of finding A individual nucleons in the small sphere (i.e. that once enough nucleons are close enough they immediately coalesce into a cluster) one obtains that the phase space density for a cluster of A nucleons is:

$$\left(\gamma \frac{d^3 N_A}{dp_A^3} \right) = \frac{1}{A!} \left(\frac{4\pi}{3} p_0^3 \right)^{A-1} \cdot \left(\gamma \frac{d^3 N_N}{dp_N^3} \right)^A \tag{2.9}$$

Taking spin and iso-spin into account the general coalescence parameter becomes [23]:

$$B_A = A \left(\frac{2S_A + 1}{2^A} \right) \cdot \frac{R_{np}^N}{N! Z!} \left(\frac{4\pi p_0^3}{3m_p} \right)^{A-1} \tag{2.10}$$

N, Z denotes the number of neutrons and protons respectively in the cluster, m_p is the proton mass, and S_A is the total cluster spin.

This model has no dependency on the collision system, except for the R_{np}. The yields of composite clusters are solely determined by the momentum differences of the constituents. Thus such models makes the coalescence parameter a unique parameter for each cluster type.

2.2 Thermodynamical Model

The simple model presented has proven to be successful for N+N systems at low energies (pre-AGS) and for p+N and p+p at all energies [23].

At higher energies however it fails for N+N collisions. This became evident with the first coalescence measurements from AGS [36], which yielded significantly lower values than at previous experiments. It led to the important understanding that light clusters are created during the last part of the collision in the outermost parts of the collision, when the fireball undergoes freeze-out [37].

In general light clusters are fairly large objects, with small binding energies, E_b, compared to the mean energy in the source. As an example consider a deuteron ($E_b = 2.2$MeV) created in the middle of a heavy collision with a temperature above 100MeV. It is obvious that the deuteron will break before escaping to be detected. Thus the measured deuterons must be created in the edge areas at a relatively late stage of the collision, where the temperature has decreased enough to allow the deuterons to survive.

Considering a simple thermodynamical model of the collision where:

- The dimension of the collision is much larger than the typical scale of the strong interaction ($\gg$ 1fm).

- The system consists of many particles ($\gg$ 1).

- The lifetime of the collision fireball is much larger than the relaxation time ($\gg$ 1fm/c).

- The particles of the system interacts frequently.

In such a collision thermal and chemical equilibrium can be upheld, allowing for the use of statistical mechanics to derive the momentum distribution [38]:

$$\frac{d^3 N_A}{dp_A^3} = \frac{g_A V}{(2\pi)^3} \exp(\frac{\mu_A - E_A}{T})$$ (2.11)

V is the collision volume at freeze-out, μ_A is the chemical potential, $E = \sqrt{m^2 + p^2}$ is the nucleon/cluster energy, g_A is the spin degeneracy factor and T is the temperature at freeze-out. Utilising the assumed chemical equilibrium, $\mu_A = N\mu_n + Z\mu_p$, and using eq. 2.11 for both nucleons and cluster, the coalescence parameter gets the form

$$B_A = A \left(\frac{2S_A + 1}{2^A} \right) \frac{R_{np}^N}{N!Z!} \left(\frac{(2\pi)^3}{m_p V} \right)^{A-1}$$ (2.12)

where the factor $\exp(E_b/T)$ have been omitted since the binding energy is small compared to the temperature.

A very important feature in eq. 2.12 is that the coalescence parameter is connected to the source volume as

$$B_A \propto V^{-(A-1)}$$ (2.13)

which for deuteron coalescence specifically yields:

$$B_2 \propto \frac{1}{V}$$ (2.14)

Thus, according to the thermodynamical model, the deuteron coalescence parameter is inversely connected to the collision volume at the time where the deuterons freeze-out. This is a powerful prediction, which will be used later on to estimate the radius of the fireball region upon the time of deuteron creation.

2.3 Density Matrix model

Models such as those presented in the last section are all very intuitive and simplistic. More complicated models, which takes into account for instance some of the quantum mechanical aspects of coalescence, exists. Such one is the density matrix model, which originally was proposed by Sato and Yazaki [39]. A throughout presentation of this model is beyond the scope of this thesis, however the main lines will be presented here.

This model treats the overlapping of the nucleon wave functions semi-classically in a coalescence perspective. Consider the internal coalescence volume introduced in eq. 2.5, $\frac{4\pi p_0^3}{3}$. For deuterons the density matrix model argues that:

$$\frac{4\pi p_0^3}{3} = \frac{3}{4}(8\pi)^{3/2} \left(\frac{\nu_d \nu}{\nu_d + \nu} \right)^{3/2}$$ (2.15)

ν_d and ν denotes size parameters of the deuteron and the fireball respectively. The deuteron wave function, $\psi_d(r)$, and the neutron/proton density matrices, $D_p(r) = D_n(r)$, is related to the size parameters in the following way.

$$\psi_d(r) = \left(\frac{\nu_d}{2\pi}\right)^{3/4} \exp\left(\frac{-r^2\nu_d}{4}\right) \tag{2.16}$$

$$D_p(r) = \left(\frac{\nu}{\pi}\right)^{3/2} \exp\left(-r^2\nu\right) \tag{2.17}$$

Using these functions gives (also in this model) power law expressions for the abundances of nuclei expressed in terms of the abundances of nucleons with the constant of proportionality being the coalescence parameter[40]. For this model it is given as:

$$B_A = \left(\frac{2s_A+1}{2^A}\right) R_{np}^N A^{3/2} \left(4\pi\frac{\nu_A\nu}{\nu_A+\nu}\right)^{3/2(A-1)} \tag{2.18}$$

The size parameter, ν, is related to the mean square radius, R_{rms} of the emitting source by:

$$R_{\text{rms}} = \sqrt{\frac{3}{2\nu}} \tag{2.19}$$

Overlapping nucleon wave functions projected onto the cluster wave function has been very successfully applied at AGS energies to describe deuteron production [23].

2.4   Flow and Density Profiles

In sec. 1.6.3 several types of flow was introduced. Of them only the radial flow persist in central collisions. It is an effect created by the pressure in the very dense center of collisions, causing a collective expansion radially, with a collective flow velocity of v_f.

The effect of the radial flow is that it adds a translatory energy contribution to the apparent temperature of each particle species [40]. Thus,

$$\langle E \rangle = \langle E \rangle^{thermal} + \langle E \rangle^{flow} \sim T_0 + mv_f^2 \tag{2.20}$$

where $\langle E \rangle$ and m is the mean energy and the mass of the particle respectively. T_0 is the fireball temperature. It is now clear that deuterons thus should have a higher apparent temperature than protons, since $m_d \sim 2m_p$. Flow have been verified by several experiments in the past. An example of this is shown in fig. 2.1, where the results obtained by the NA44 experiment in [41] is presented.

The concept of flow have a profound effect on what to expect in B_2 observations. If the general particle momentum distributions roughly follows

$$\frac{d^3N_A}{dp_A^3} \sim \exp\left[\frac{-E_A}{T_A}\right] \tag{2.21}$$

characterised by the inverse slope parameter, T_A, the coalescence parameter is given by:
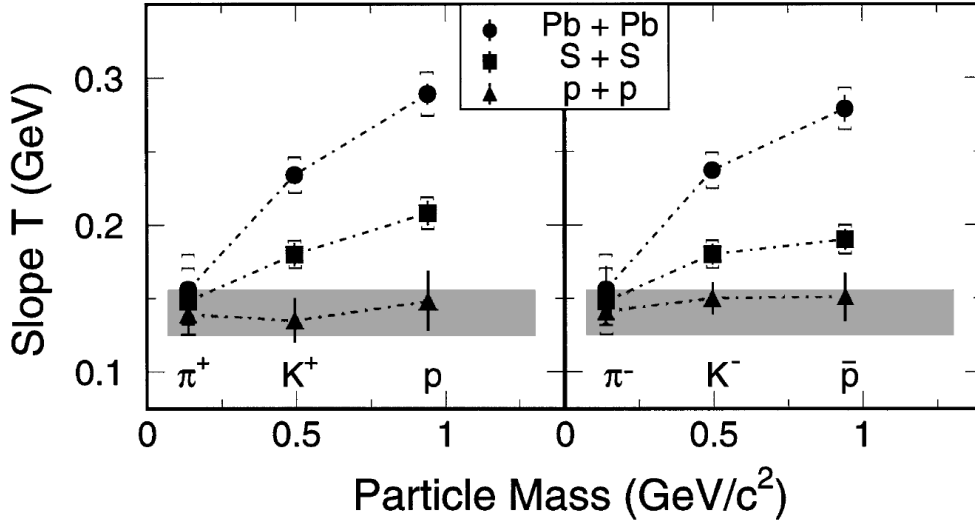
Figure 2.1: An example of experimental verification of flow in heavy ion collision from
the NA44 experiment. It is seen that the more participants are involved
in the collision, the more pronounced the flow is. This can be attributed
to a larger density, and thus a larger pressure gradient in such collisions.
Furthermore it is seen, that in heavy ion collisions the measured value of
T increases for heavier particles.

$$B_2 \sim \frac{\exp\left[\frac{-E_d}{T_d}\right]}{\exp\left[\frac{-E_p}{T_p}\right]^2} = \exp\left[E_d\left(\frac{1}{T_p} - \frac{1}{T_d}\right)\right] \tag{2.22}$$

In eq. 2.22 it has been used that $E_d \sim 2E_p$. It is seen that if the proton and deuteron spectra
have the same slope ($T_p = T_d$), B_2 will be independent of momentum. If $T_d > T_p$ then B_2 will
increase with momentum. In later sections measurements of B_2 versus p_T is presented.

2.4.1 Polleri Model

In this section a phenomenological model proposed by Polleri *et al.* [40] regarding the interplay
between collective flow and density profiles is presented. It is clear that the flow profile and
the density profile are connected, since a change in the flow also changes the density profile
(and vice versa). The model by Polleri relates position and momenta by the presence of flow.
The main feature of the model is, that it shows how the difference in the observed slope in
different particle spectra constrains the possible density and flow profiles.

The flow profiles considered is given by the transverse velocity field:

$$\vec{v_T} = v_f \left(\frac{r_T}{R_0} \right)^\alpha \vec{e_T} \tag{2.23}$$

Here $\vec{v_T}$ is the transverse velocity at r_T. $\vec{e_T}$ is the transverse unit vector. v_f and R_0 are the strength and scale parameter of the flow profile. The exponent α is used for different profiles, i.e $\alpha = 1$ is a linear flow profile[7] and $\alpha = 1/2$ is labelled a square root flow profile.

In the work of Polleri three density profiles are generally considered. The first one is a profile where the density as a function of radius is a Gaussian. The next profile considered is labelled a box profile. It has a constant density until a maximum radius, where it changes to zero. Homogeneous spheres for instance follow a box profile. The last profile Polleri labels a surface profile. It is reminiscent to the density profile observed in a supernova explosion, e.g. a depleted central region enveloped by a spherical shell of constant density. Fig. 2.2 shows an example of this interplay between a Gaussian density profile and a linear flow profile. Measurements of the slopes of spectra thus might assist in narrowing down the possible profiles.

In fig. 2.3 the Polleri calculations of the inverse slope parameter as a function of mass number is shown. It is seen that the included E-802 data[43] suggests a Gaussian density profile with a linear flow profile. It is clear that deuteron measurements becomes vital in distinguishing between the profiles, since the various profiles are very similar for small A. Thus low uncertainty measurements of deuterons are very useful.

Another useful calculation is seen in fig. 2.4, where the predicted B_2 versus p_T is shown for several density and flow profiles. Again the E-802 data is plotted on top of it, suggesting that the the density profile is either a box profile or a surface profile.

Determining the exact flow profile based on the E-802 data is not possible; for that more data are required. However the Polleri model yields a intuitive way to look at flow and density profiles. In later sections the obtained results of this work will be compared with the Polleri model qualitatively.

---

[7]And is very similar to the Hubble law governing the expansion of the Universe
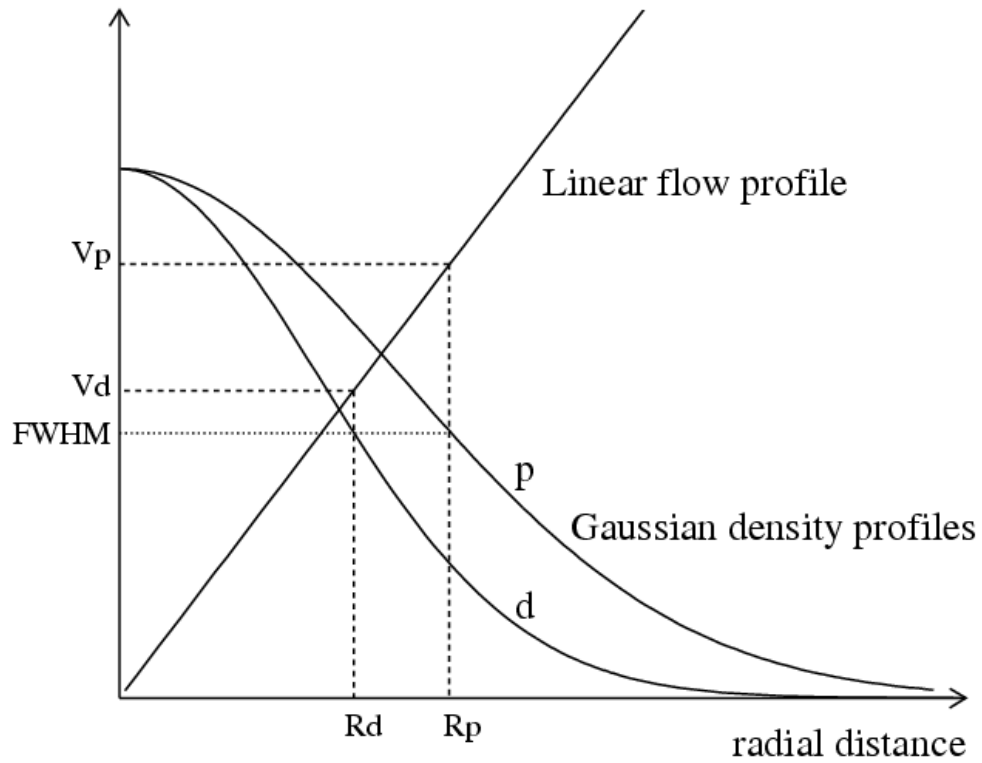
Figure 2.2: Illustration of the connection between density and flow profiles. Gaussian density profiles for both deuterons and protons are shown. At FWHM the mean radii, R_d and R_p respectively, is marked. Each of these radii then corresponds to a flow velocity, v_d and v_p, marked as the intersection with the chosen linear flow profile. Figure taken from [42].
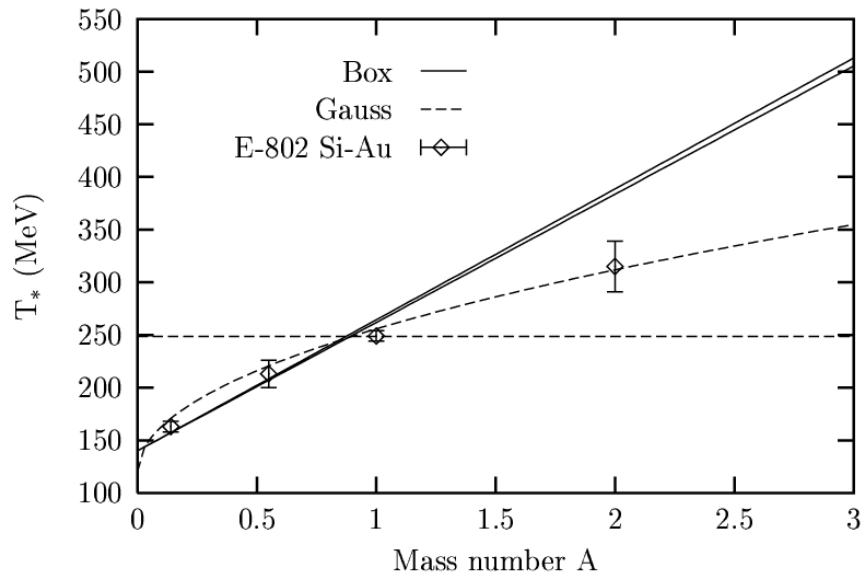
Figure 2.3: The inverse slope parameter, T_A (labelled T_* on the figure), as a function of mass number, A. Included is two types of density profiles; Box profile (solid lines) and Gaussian Profile (dashed lines). For each profile the bottom curve is a linear flow profile , and the top curve is a square root flow profile. On top of the curves data from the E-802 Experiment[43] is plotted. Figure taken from [40].
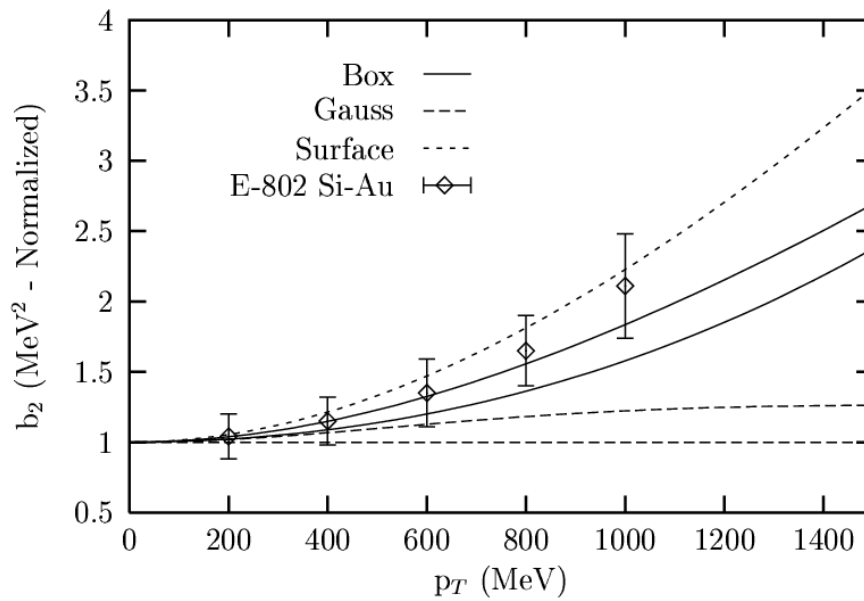
Figure 2.4: The B_2 versus p_T distribution for various density profiles. For the box profile and the Gaussian profile the top curve are for square root flow profiles and the bottom curve for a linear flow profile. Like in fig. 2.3 the data points are from [43]. Figure taken from [40].

Chapter 3

Experimental Setup

In the following the experimental setup at the BRAHMS experiment will be covered.

3.1 The Relativistic Heavy Ion Collider
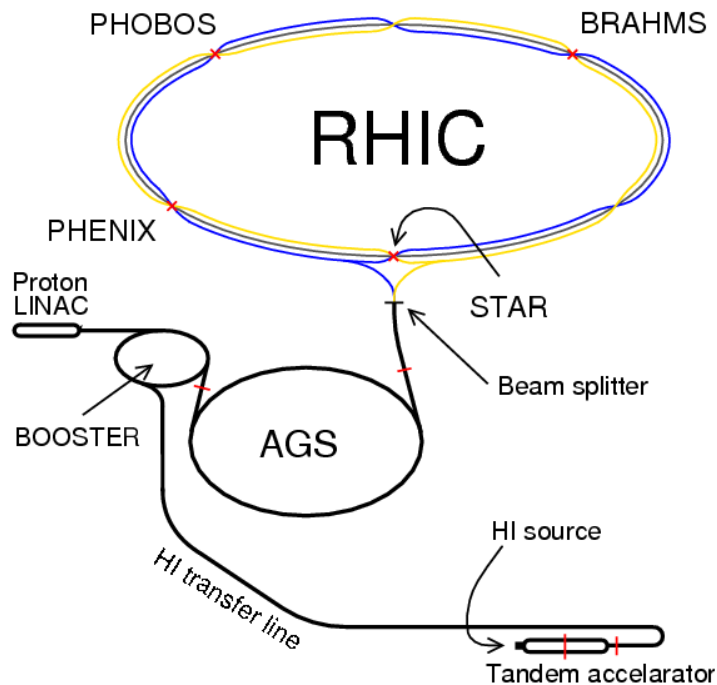
Figure 3.1: Schematic view of the RHIC facility

The Relativistic Heavy Ion Collider (RHIC) [44] is a part of the accelerator complex at Brookhaven National Laboratory (BNL). The main purpose for the RHIC is to produce Au-Au and p-p collisions at the top RHIC energy of $\sqrt{s_{NN}} = 200\,\text{GeV}$. Figure 3.1 shows a

schematic view of the RHIC facility. The old AGS accelerator complex (Tandem, Booster, AGS etc.) is now used as a pre-accelerator. When leaving the AGS the beam is split in two separate beams, travelling in RHIC clockwise and counterclockwise respectively. In the RHIC the particle beams are accelerated to their final energy. There are six experimental halls at RHIC where the beams can intersect to produce collisions. However only four of these are occupied by the RHIC experiments STAR [45], PHENIX [46], PHOBOS [47] and BRAHMS [48].

3.2   The BRAHMS Experiment
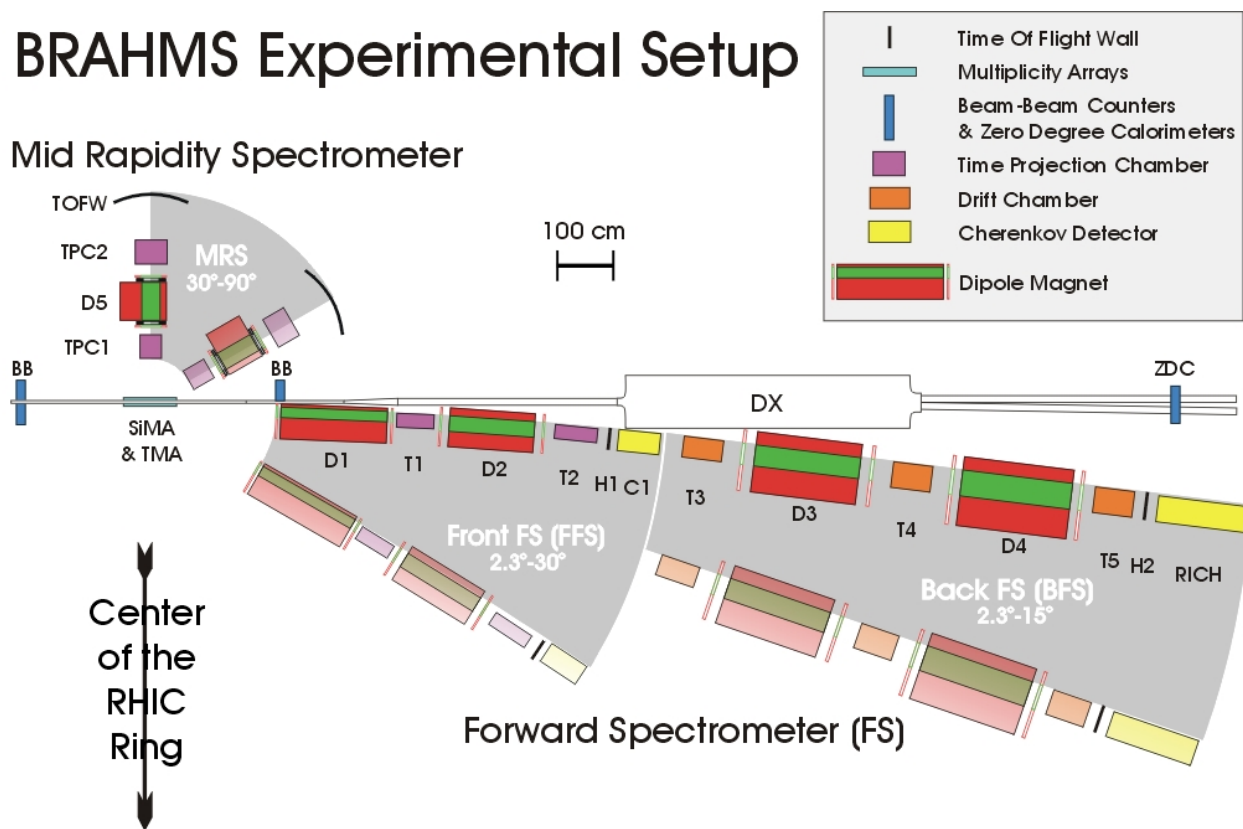
Figure 3.2: Top-down view on the BRAHMS Experiment. Figure taken from [50].

The Broad Range Hadronic Magnetic Spectrometer (BRAHMS) is located at the 2 o'clock experimental hall at the RHIC. Compared to the two large experiments at the RHIC, STAR and PHENIX, BRAHMS is a small experiment the purpose of which is to facilitate detection and identification of high momentum charged particles. In order to allow for detection of midrange momentum particles ($p \approx 1 - 5\,\text{GeV}$) as well as high momentum particles ($p \approx 20 - 25\,\text{GeV}$) the BRAHMS detector consists of two separate detector systems, the Mid Rapidity Spectrometer (MRS) and the Forward Spectrometer (FS). What makes BRAHMS unique

compared to the other experiments is the ability to rotate the two spectrometer arms, thereby covering a large window of rapidity.

Furthermore the BRAHMS detector makes use of the global detectors common to all RHIC experiments. In the following sections the various detectors will be introduced. This description is based on [48] and [49], where nothing else is mentioned. A sketch of the BRAHMS experimental setup is shown in figure 3.2.

3.3 The Global Detectors

BRAHMS utilises three global detectors. These are the Multiplicity Arrays, the Beam Beam Counters and the Zero Degree Calorimeters. The purpose of these detectors is to detect general properties of the collisions, that are not reliably detected in either MRS or FS.

3.3.1 Multiplicity Arrays
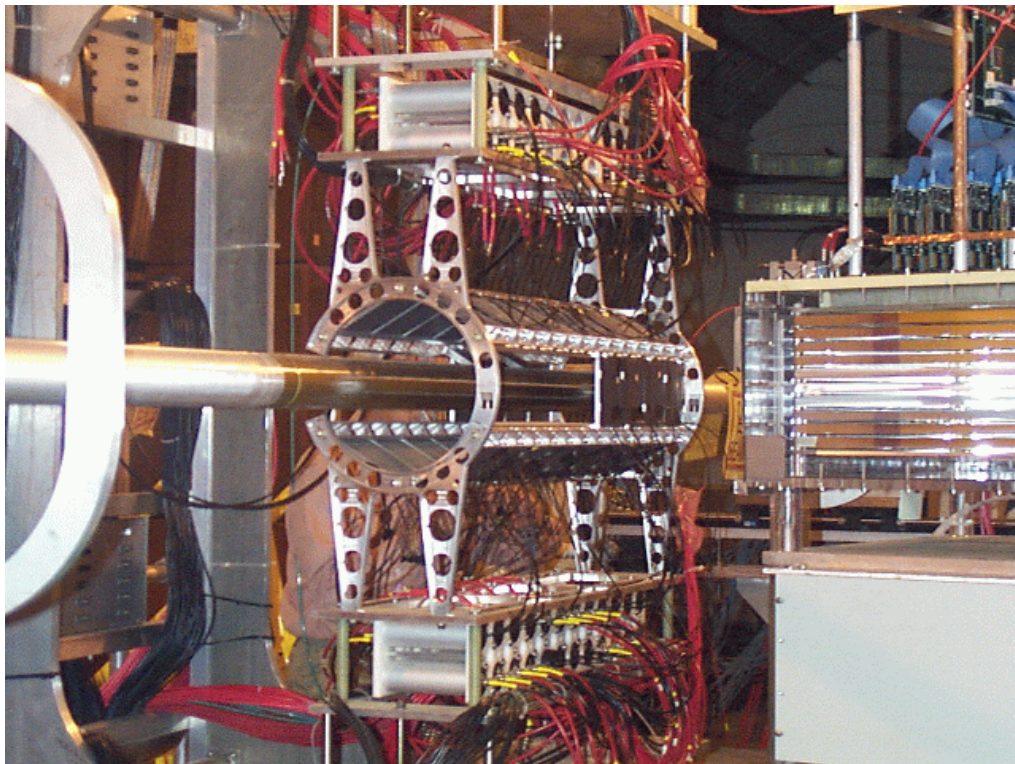
Figure 3.3: The multiplicity array. Figure taken from [7].

Multiplicity is an important observable in heavy ion physics as the number of particles emerging from a heavy ion collision is directly related to the definition of the centrality of the collision. The Multiplicity Arrays (MA) consist of two parts: The inner array consisting

of Si-strips (SiMA in fig. 3.2) arranged hexagonally relative to the beam pipe around the interaction vertex and the outer array made of plastic scintillator (TMA in fig. 3.2). The outer array is also arranged as a hexagonally barrel coaxial to the inner array. The MA measure the energy loss of particles passing through the inner and outer arrays and convert it to $dN/d\eta$, the particle multiplicity per unit of pseudorapidity. For more details on the MA see [51].

3.3.2 Beam Beam Counters
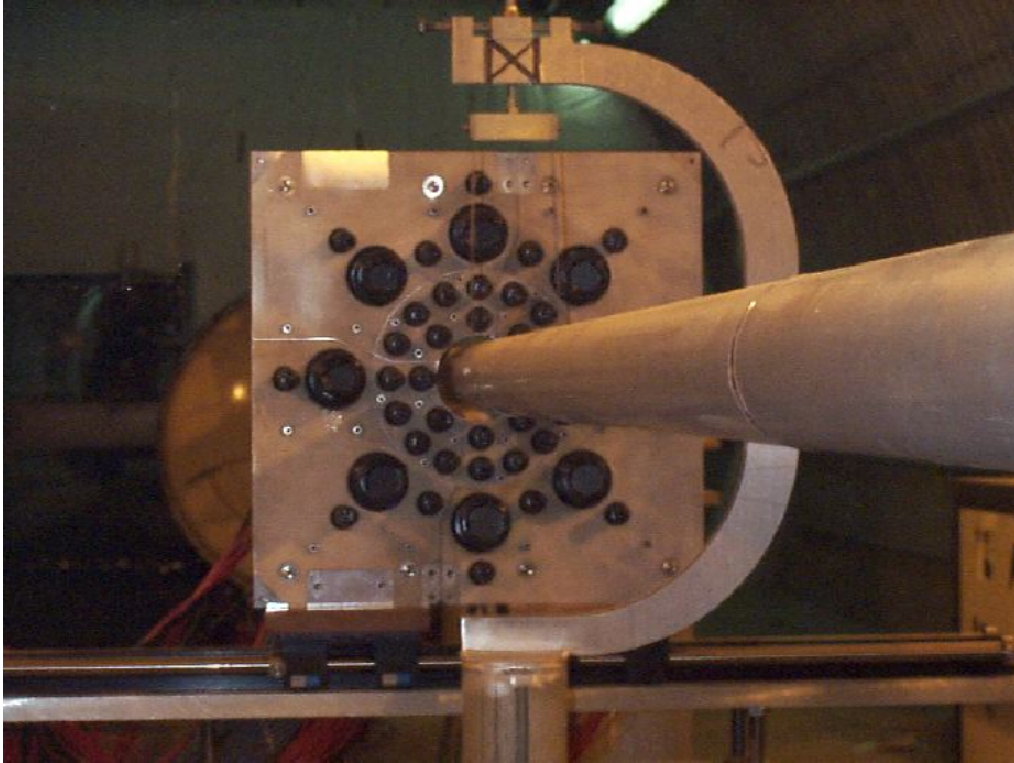
Figure 3.4: The left Beam Beam Counter. Figure taken from [7].

The beam-beam counters (BBCs) are positioned on either side of the interaction point (IP), 220 cm from the nominal IP. Constructed from two Čerenkov detectors supported by photo-multiplier tubes, the beam-beam counters are capable of determining the actual collision vertex, i.e. the measured IP. This is done with the zero time signal taken as

$$T_0 = (t_\text{left} - t_\text{right})/2 + T_\text{const}$$

Here t_left and t_right are the time signals from the left and right BBC respectively and T_const is a time-constant depending on the electronics. The counters have a 50 ps time resolution, which gives an uncertainty in the determination of the vertex of approximately 1.5 cm. BRAHMS

utilises three beam-beam counters on each side of the vertex. They are positioned at pseudo-rapidities of 3.1 , 3.4 and 3.6. For more details on the BBCs see [52].

3.3.3 Zero Degree Calorimeters

Figure 3.5: Close up of one of the Zero Degree Calorimeters. Figure taken from [7].

The Zero Degree Calorimeters (ZDCs) of the BRAHMS experiment are located on either side of the nominal IP, 18 meters from the IP. Their main purpose is to measure the luminosity of the RHIC to monitor its performance during runs. This enables the RHIC team to make RHIC runs as stable and efficient as possible during data taking periods. The ZDCs detect the neutrons that stem directly from the colliding nuclei. These neutrons are not bend in the magnetic fields so they do not follow the RHIC ring and are thus picked up in the ZDCs. From the energy deposit of these neutrons the luminosity can be calculated. The ZDCs provide an alternative way of determining the actual IP but the resolution is about 3.6 cm. This is a little higher than for the BBCs, which is why the determination of the IP is primarily done by the BBCs. The energy deposit of the neutrons can also be used to determine the multiplicity of particles emerging from the collisions. Furthermore the ZDCs are used as the minimum bias trigger for which a signal in both ZDCs within the same window of time is required. A more

in depth description of the ZDCs can be found in [53].

3.4   The Mid Rapidity Spectrometer
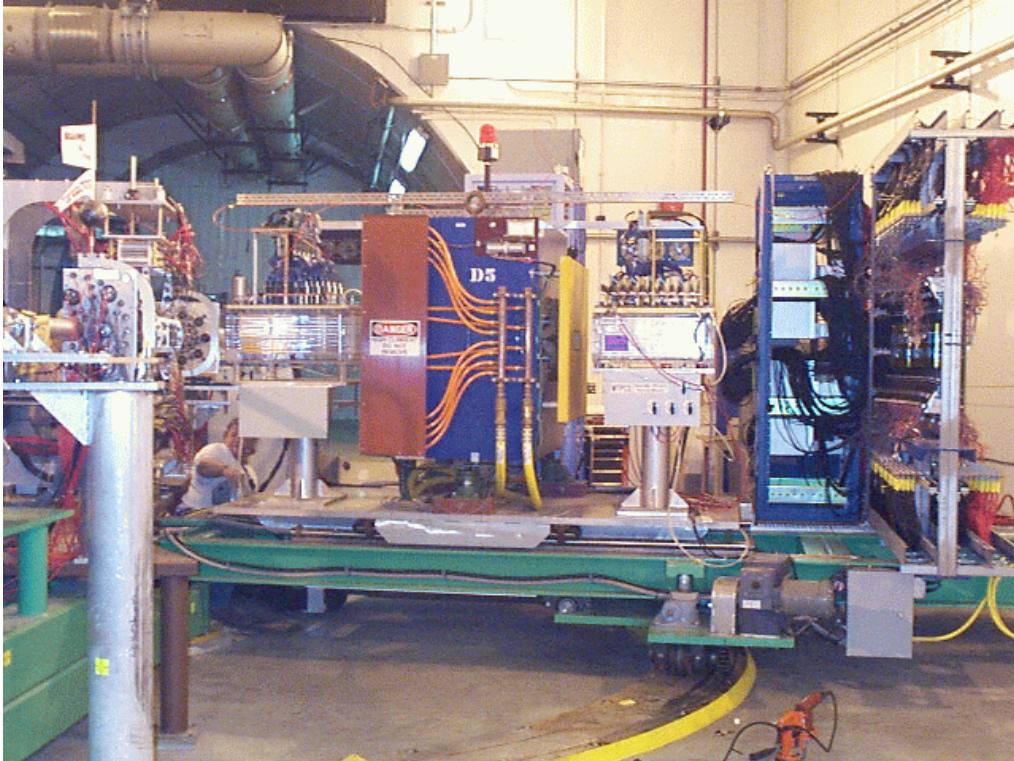
Figure 3.6: The Mid-rapidity Spectrometer. Figure taken from [7].

The overall purpose of the MRS is to provide particle identification and tracking of particles emitted around mid-rapidity. The MRS can be rotated to cover angles with the beam-pipe of $30° < \theta < 95°$ so the pseudorapidity covered is $-0.087 < \eta < 1.32$. Geometrically the MRS has an acceptance of 6.5 msr. As shown in figure 3.2 the MRS contains two Time Projection Chambers (TPCs), a dipole magnet and a Time of Flight (TOF) wall.

3.4.1   Time Projection Chambers

The purpose of the TPCs is to measure three dimensional particle trajectories. When a particle enters the gas inside a TPC it causes ionizations through collisions with particles in the gas. This leads to the emission of electrons that drift along the electric field lines in the TPC. When these electrons cross the wires that are suspended inside the TPC cavity, they induce current in these wires, thereby generating a signal. This signal is read out to yield positions and times of the particle travelling through the TPC. As the TPCs are positioned

outside the magnet the tracks obtained in this way will be straight lines. BRAHMS utilises four TPCs with an intrinsic position resolution around $400\mu m$ and a track-track resolution around 15 mm.

3.4.2 Dipole Magnet

The dipole magnet (D5) of the MRS is a conventional dipole electromagnet. It is located between the two TPCs in order to deflect charged particles. This deflection is used to determine the momentum of the traversing particle.

3.4.3 Time of Flight Wall

The MRS has a time of flight wall installed at the end of the spectrometer. Its purpose is to measure the flight time of the particles as the difference between the collision start time (from the BBCs) and the signal in the TOF wall. This measurement is used in conjunction with the momentum measurement in the magnet to identify different particle species.

The TOF wall in the MRS, the TOFW consists of 125 scintillating slats that are read out by photo-multiplier tubes.

3.5 The Forward Spectrometer

By construction, the FS is divided in two parts: The front forward spectrometer (FFS) and the back forward spectrometer (BFS). The FFS covers angles from 2.3°to 30°while the BFS covers a range of 2.3°to 15°. This corresponds to intervals in pseudorapidity of $1.32 < \eta < 3.91$ and $2.03 < \eta < 3.91$, respectively. The FS covers 0.8 msr of solid angle.

The FS consists of two TPCs and three Drift Chambers (DC) for tracking particles; four dipole magnets for momentum determination, two TOF walls and a Ring Imaging Čerenhov (RICH) for identifying particles.

For the analysis at hand only the particles traversing through the entire FS are analysed.

3.5.1 Drift Chambers

Like the TPCs the drift chambers provide coordinates for tracking of the particles passing through. While the TPCs require lots of electronics the DCs are easier to operate. The DCs have a slightly better resolution than the TPCs; their position resolution is around $300\mu m$ and their track-track resolution is ≈ 10mm.

3.5.2 H1 and H2

The FS employs two TOF walls, H1 and H2. As indicated in figure 3.2, H1 is located in the FFS and H2 is located in the BFS in front of the RICH. These TOF walls are similar to the one in MRS. H1 is larger than H2, but due to its location it is only able to identify lower momentum particles, since the time resolution compared to the time-of-flight is rather large.
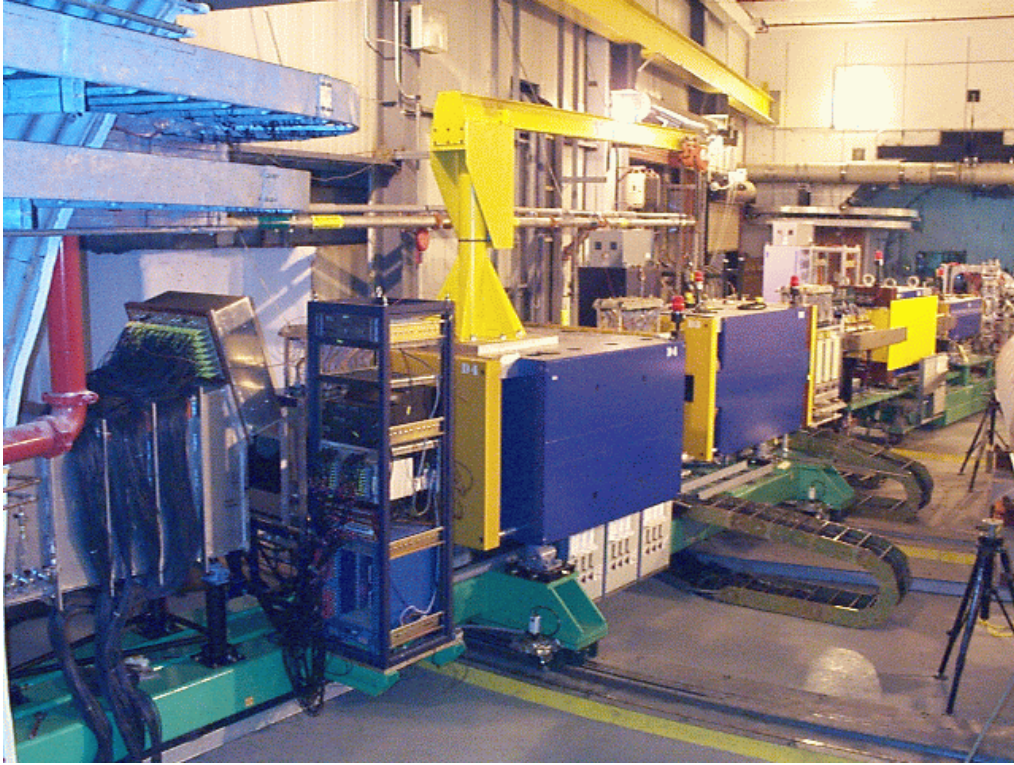
Figure 3.7: The Forward Spectrometer. Figure taken from [7].

3.5.3   The RICH

The Ring Imaging Čerenkov (RICH) detector is located at the end of the FS. It is used for determining velocity of high momentum particles. It is based on detecting Čerenkov radiation which is emitted when a particle travels through a medium at a velocity surpassing the speed of light in that medium. The radiation is emitted in a cone with the Čerenkov emission angle, $\theta_{\check{c}}$, given by:

$$\cos(\theta_{\check{c}}) = \frac{1}{n\beta} \tag{3.1}$$

Here n = 1.00185 is the index of refraction of the gas in the the RICH and β is the velocity of the traversing particle.

The Čerenkov radiation hits a spherical mirror at the back of the RICH, getting focused up onto the image plane, where it is detected as rings. The ring radii are used to identify particles. In fig. 3.9 the basic principle of the RICH is illustrated.
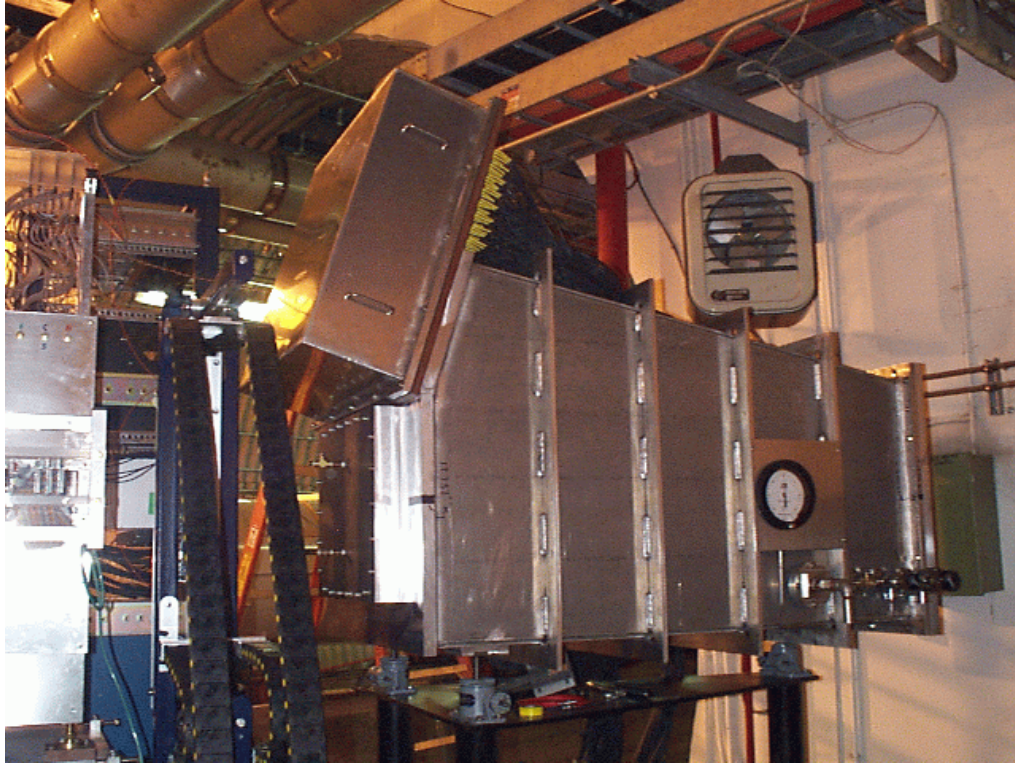
Figure 3.8: Photo of the RICH. Figure taken from [7].

3.6 Data Acquisition System

Whenever an collision happens, the Data AcQuisition (DAQ) system collects the signals from the various sub-detectors. In the following the procedure regarding whether to read out an event or not is described.

3.6.1 Triggers

Triggers are set up as being signals from sub-detectors or combinations of these, which defines whether a given event should be read out by the DAQ. For the data run presented in this report, the different triggers and their constraints on the data are given in table 3.1. Trigger 1 requires that the there is a signal in both BBCs within a narrow time interval. Trigger 2 is a FS trigger requiring that there is a hit in H1, a signal in the FS in addition to fulfilment of trigger 1. The signal in FS is recorded by a specific trigger detector, made up of scintillators, located just past the D1 magnet. Trigger 3 is the MRS trigger requiring a signal in MRS (done in a similar fashion as in the FS), and the fulfilment of trigger 1. Trigger 4 is similar to trigger 1 except it is for the ZDCs. Trigger 5 was not used in this run. Finally trigger six is another FS trigger based on the ZDCs instead of the BBCs.
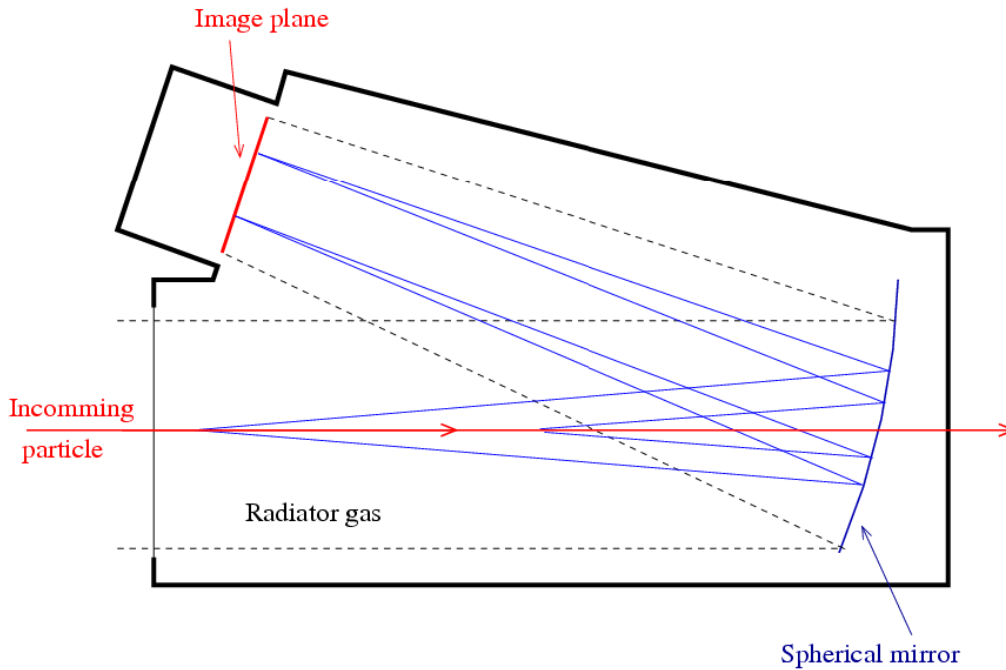
Figure 3.9: Sketch of the principle of the RICH. Figure taken from [25].

Trigger Scaledown

The DAQ at BRAHMS is not capable of recording every event provided by RHIC. To circumvent this, the BRAHMS experiment assigns each trigger with a scaledown factor. When an event occur the trigger box sends a signal directly to the DAQ system, which selects whether or not to keep the event. So if a specific trigger have a scaledown of n, only every n'th event fulfilling that specific trigger criteria is kept.

The data from the event are not sent as quickly to the DAQ as the trigger box signal. Instead they are sent through lots of cable, delaying their arrival at the DAQ. The reason for this, is that once they arrive, it has already been decided if the event should be recorded or

Trigger Nr.	Requirements
1	Coincidence signal in the BBCs
2	Hit in H1, signal in FS and trigger 1
3	Signal in MRS and trigger 1
4	Coincidence signal in both ZDCs
5	Not used in this run
6	Hit in H1, signal in FS and trigger 4

Table 3.1: Trigger definitions for the BRAHMS 2004 run

not, hence allowing the latter to be discarded immediately. The scaledown factor is recorded for normalisation purposes later on.

3.7 Initial Data Selection

At the BRAHMS experiment the raw data are treated at various levels even before the main analysis starts. In this section these different steps are briefly discussed. For further description on these steps consult [7], [25] or [52].

- **Initial Calibrations.** The first step after storing the raw data on computers, is doing calibrations of the TPCs.

- **Local Tracking.** Next step is to reconstruct the local tracks; i.e tracks inside a single TPC.

- **Global Tracking.** When the local tracks are done for all TPCs, these are paired with each other (if possible) to give the full trajectory of particles.

- **Final Calibrations.** Calibrations of the TOF walls are now done.

- **DST Generation.** The final step is to create DSTs (Data Summary Tree), containing information on all aspects of the run in a tree structure.

Chapter 4

Analysis

This chapter is devoted to describing the analysis process. A brief overview of this process is:

- **Event selection:** Limit the study to events containing relevant information.

- **Track selection:** Only primary tracks, i.e. tracks from the initial collision, should be studied.

- **PID selection:** For each track the particle species is determined using the signals from the PID detectors.

- **Corrections:** Track by track corrections should be applied after the PID selection, the most important being efficiency and acceptance corrections.

- **Spectra building:** From the identified, corrected tracks the invariant spectra containing the number of particles per rapidity and transverse momentum bin can be built.

Each item will be explained in further details in the coming sections.

4.1   Data Naming Convention

When recording data at the BRAHMS experiment, the spectrometers are fixed on a single polar angle, θ, magnetic field strength and polarity for a period of time. This will be referred to as a setting in the following. The name adopted for each setting follows the convention: (polar angle)(polarity)(magnet current).

In this work the following setting have been analysed:

- **MRS:** 90A2255, 90B2255, 90A1050, 90B1050, 40A2255, 40B2255, 40A1050, 40B1050.

- **FS:** 10B1219, 10B861, 8B861, 8B608, 4B3450, 3B3450, 3B1723, 2B3450, 2B2442, 2B1723.

The magnet currents are given in Ampere and denote the current sent through the first magnet in the respective spectrometer; i.e D1 in FS and D5 in MRS. In the MRS 2255 corresponds to the full field (maximum field). For the FS 3450 is the maximum magnetic field strength.

4.2   Software

The analysis is done using ROOT (ROOT's Object Oriented Technologies)[54] as a framework for the analysis software. ROOT is a C^{++} based object oriented data analysis program developed through the work performed at CERN. ROOT is geared to handle large data samples, containing utilities for many purposes e.g. data collection, analysis, and even simulations. The software used in this analysis is contained in the package 'BANAPP'(BRAHMS ANalysis APPlictions). This package is being developed by the HEHI group for the BRAHMS collaboration. To facilitate this analysis, the core packages have been modified accordingly.

4.3   Event Selection

Three global cuts are applied to select relevant events:

- **Centrality:** Only the 20% most central events are analysed.

- **IP selection:** Only events where the measured IP is within a maximum distance from the nominal IP is analysed. For the MRS this maximum is ± 15 cm and for the FS this limit is ± 20 cm.

- **ZDC and BB coincidence:** Only events where the ZDC and BB IP measurements coincides are analysed.

The centrality is determined, as mentioned in sec. 1.5, by the multiplicity. In fig. 4.1, an example of centrality classes derived from the multiplicity, is shown.

The decision to select the 20% most central collisions is done based on two considerations. First of all it is desirable to choose as central collisions as possible to hopefully investigate collisions in which a QGP is formed. However when working with deuterons lots of statistics is needed, why a larger centrality class is preferred. In the end 0-20% was chosen. Measurements of B_2 at $\sqrt{s_{NN}} = 200\,\text{GeV}$ by PHENIX also uses this centrality class making direct comparisons possible, which are presented in the results chapter.

The IP cut is chosen on basis of an analysis done in [7], which shows that several of the triggers becomes inefficient outside $\pm 15(20)$ cm from the vertex in the MRS(FS).

Requiring that the IP determination from the ZDC and the BB coincides rejects events, where for instance background particles have caused bad timing signals in one of the counters. The distribution of the ZDC/BB differences are Gaussian, and in this work a 3σ cut is applied. The effect of this cut is illustrated in fig. 4.2.

4.4   Track Selection

Track selection is done by applying two cuts:

- **Track quality cut** Tracks must be of good quality, i.e. coming from the IP and being matched well in the tracking detectors.
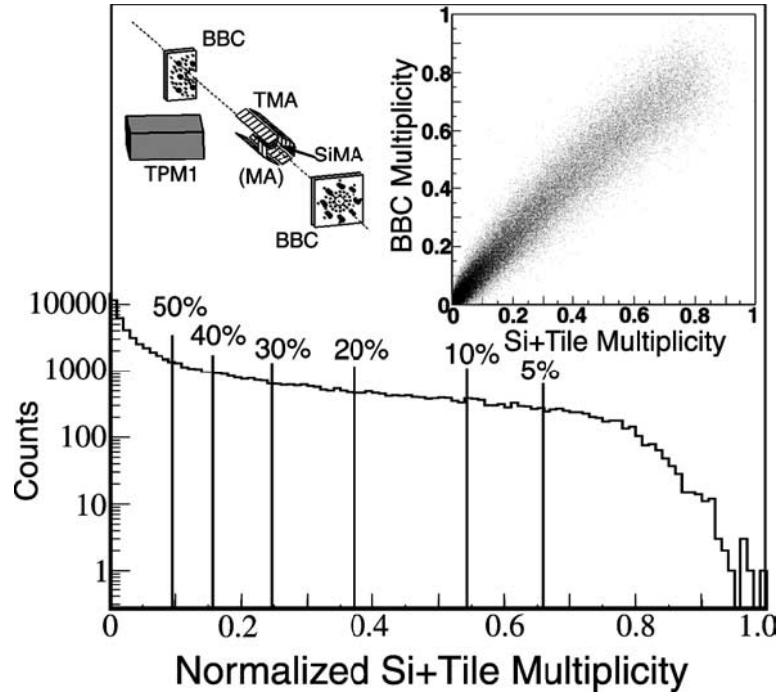
Figure 4.1: The multiplicity distribution normalised to the highest multiplicity. In-
dicated are the various centrality classes. In the upper part of the figure
a sketch of the interaction region of BRAHMS is shown as well as the
correlation between the multiplicities determined by the BBCs and the
MA (Si+Tile). In this work the centrality class 0-20 % is chosen. Figure
taken from [55].

- **Magnet fiducial cut.** Tracks which come too near to one of the magnets are rejected.

Track Quality Cut

When cutting in the track quality different methods are used in the FS and the MRS. In the
FS a method computing a track quality parameter, χ^2, of each tracks and then cutting away
high χ^2 tracks is used, whereas in the MRS a simpler method is used, where it is required that
the track must point back to the IP. Let us consider the simple case first.

In the IP pointing cut all tracks are extrapolated back to the IP and is then required to
originate within a given maximum distance from the IP. The pointed track vertex is given
by the intersection between the YZ-plane and the extrapolated track. The pointed tracks
distributions in the Z and Y directions are fitted to Gaussian, to find the means and standard
deviations, μ_Z, μ_Y, σ_Z and σ_Y. The pointing cut is then defined such that only tracks where

$$\sqrt{\left(\frac{Z_{pointed} - \mu_Z}{\sigma_Z}\right)^2 + \left(\frac{Y_{pointed} - \mu_Y}{\sigma_Y}\right)^2} \leq 4 \tag{4.1}$$
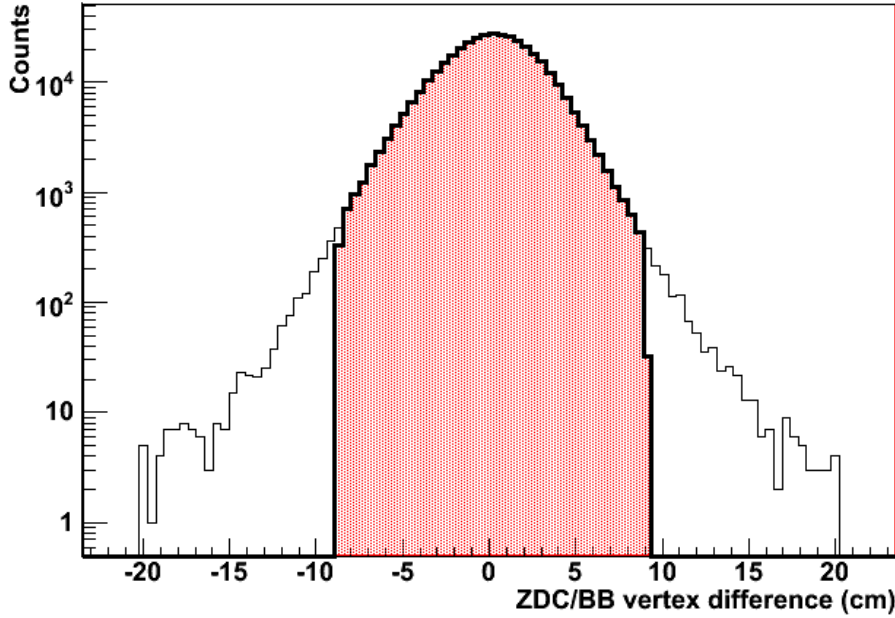
Figure 4.2: Coincidence between the ZDC and BB IP determination for the setting 40A1050. Highlighted in red is the selected 3σ Gaussian cut.

is fulfilled, are selected. $Z_{pointed} = Z_{trk} - Z_{BB}$ gives the deviation from the measured BB vertex for each track. This is only necessary for the Z-axis, since for the Y axis the pointed track vertex is defined at the specific measured BB vertex. $Y_{pointed}$ therefore is just the track vertex. Thus the pointing cut denote an elliptical cut of 4σ in the ZY plane. In fig. 4.3 the pointing cut is shown for the setting 40B1050.

In fig. 4.4 and 4.5 the effect of the pointing cut for protons and anti-protons in the MRS is shown. The difference in the amount of particles at large deviations, $N\sigma$, between protons and anti-protons can not be accounted for by merely particle decays. Had that been the case both protons and anti-protons would have a similar high deviation tail. Instead the difference mainly stems from low momentum protons being knocked out of the beam-pipe material by particles from collision.

In the FS it becomes a little trickier, since in all tracking detectors the local tracks must be matched well to be selected. For further details consult [56]. The quality track cut is done by defining the track quality parameter, χ^2. It is not exactly a proper statistical χ^2 though, why the name might seem a bit ill chosen. It is in some regards similar to the statistical χ^2 by being the squared residuals, but it can not be normalised by the numbers of degrees of freedom. However it is the custom name inside the BRAHMS collaboration. It is given as:
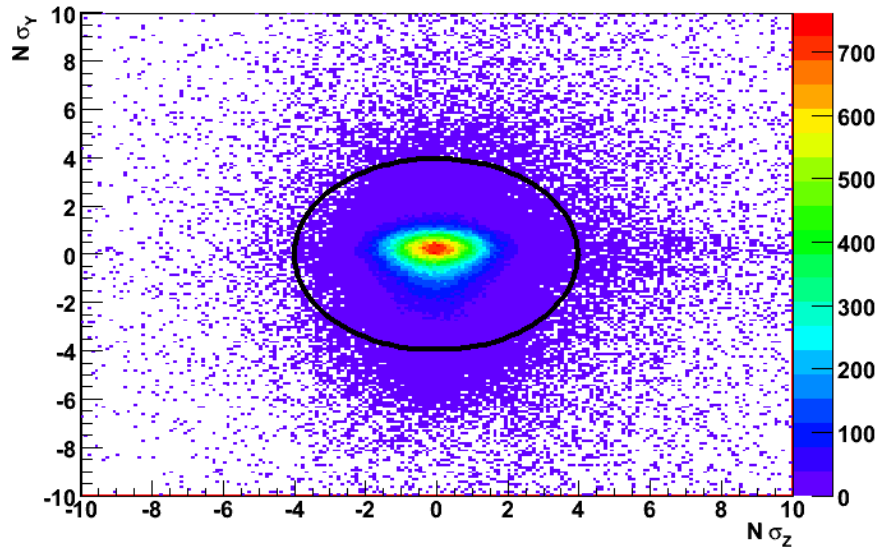
Figure 4.3: The pointing cut in the MRS. The vertex distributions of pointed tracks in the Y and Z directions measured in standard deviations are plotted for the setting 40B1050. The selected data is inside the ellipse.
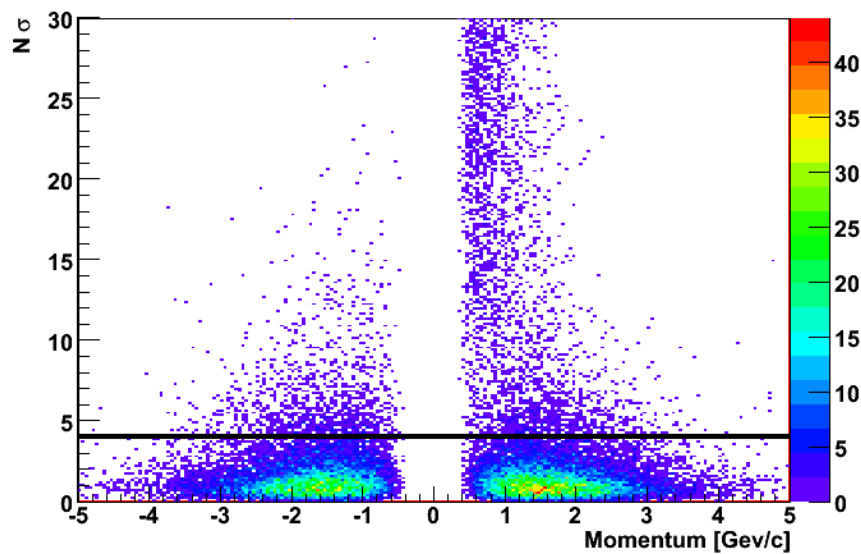
Figure 4.4: The pointing cut in the MRS. Plotted is the distance in standard deviations from the IP for protons and anti-protons. The background from protons knocked out of the beam-pipe is clearly visible. The horizontal line shows the 3σ cut line, i.e. everything below that line is selected, and the rest discarded. The setting in the plot is 40B1050.
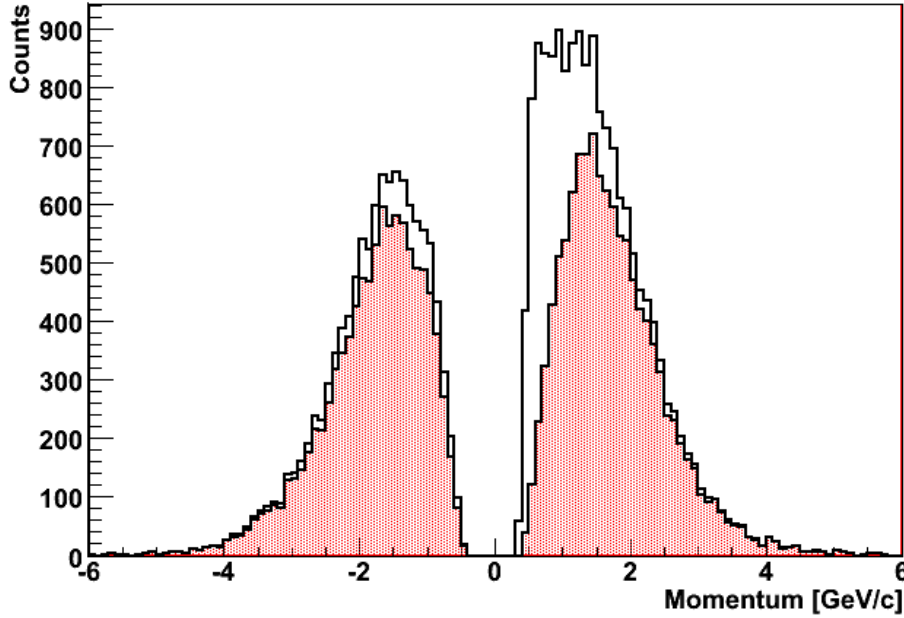
Figure 4.5: The effect of the pointing cut in the MRS. Shown is the momentum distribution of (anti-)protons before and after the pointing cut. The shaded area is the selected tracks. The setting in the plot is 40B1050.

$$\chi^2 = \left(\frac{Z_{\mathrm{vtx}}^{\mathrm{global}} - Z_{\mathrm{vtx}}^{\mathrm{proj}}}{\sigma_{\mathrm{Z-vtx}}}\right)^2 +$$

$$\sum_N \left(\left(\frac{X_{\mathrm{trk}} - X_{\mathrm{proj}}}{\sigma_{\mathrm{X}}}\right)^2 + \left(\frac{Y_{\mathrm{trk}} - Y_{\mathrm{proj}}}{\sigma_{\mathrm{Y}}}\right)^2 + \left(\frac{\alpha_{\mathrm{Y-trk}} - \alpha_{\mathrm{Y-proj}}}{\sigma_{\alpha_{\mathrm{Y}}}}\right)^2 + \left(\frac{\theta_{\mathrm{trk}} - \theta_{\mathrm{proj}}}{\sigma_\theta}\right)^2\right)$$

$$(4.2)$$

Here $Z_{\mathrm{vtx}}^{\mathrm{BBC}}$ is the vertex measured in the BBCs and $Z_{\mathrm{vtx}}^{\mathrm{proj}}$ is the projection of the track back to the beam axis ZY-plane. The sum is over the N tracking chambers of the FS, where (X, Y) is the coordinates of the track in tracking chamber N. α_Y and θ denotes the slope of the track in the Y-direction and the angle between the track and Z-axis in the XZ-plane respectively. In the sum, the subscript 'trk' denote the actual measured local track, whereas the subscript 'proj' denotes the same quantity for the projected global tracks . So to summarise the χ^2 yields information about the deviations between the local tracks and the reconstructed global track.

The calculated χ^2 values are compared to a simulated distribution, which can be seen in fig. 4.6. The width of each simulation momentum slice is fit to the function: $f = A + B/p$, where the constants are found to be: A=28.5 and B=180. The fit function is then used on the measured χ^2 distribution, requiring that the selected tracks are within 4σ, i.e.:
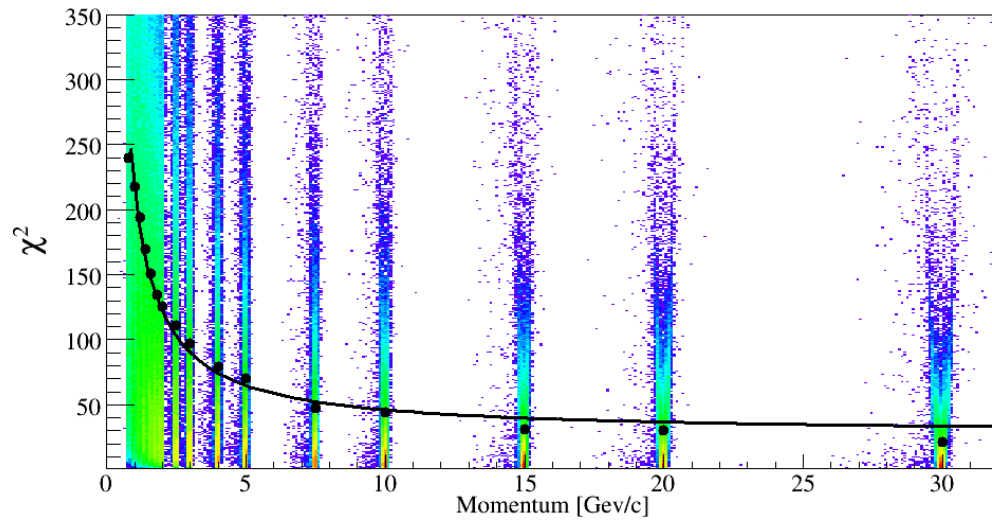
Figure 4.6: Example of the simulated χ^2 distribution as a function of momentum for the FS. The curve is a fit to the widths of each simulated momentum slice. The fit function is $f = 28.5 + 180/p$. Figure taken from [56].
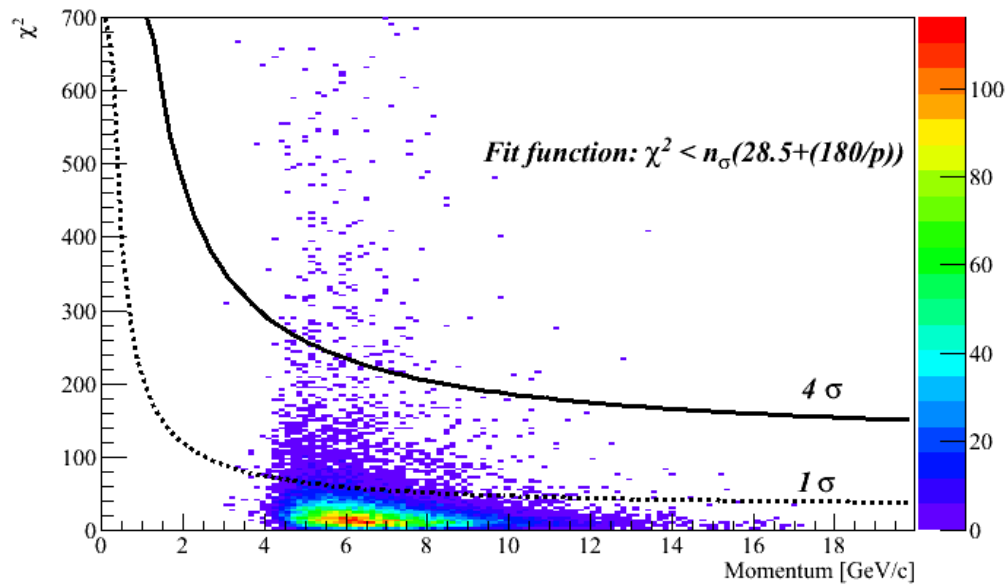
Figure 4.7: The quality track cut illustrated for the setting 8B861. The χ^2 of the tracks are shown together with the 4σ cut from eq. 4.3. The tracks above the solid line are rejecting as poorly matched tracks. The dashed line shows the 1σ fit function

$$\chi^2 < 4 \cdot (28.5 + 180/p) \tag{4.3}$$

Tracks above this are rejected as poorly matched tracks. The selected tracks can be seen for the setting 8B861 in fig. 4.7.

Magnet Fiducial Cut

The second cut, the magnet fiducial cut, makes sure that particles do not come too close to the physical sides of the magnets, while passing through the magnet gaps. Local tracks are matched in the magnets, where it is required that they do not get closer than $1\,\mathrm{cm}$ cm to any of the magnet sides. In the D5 magnet this means a data reduction of more than 20%, since the vertical aperture is only approximately $10\,\mathrm{cm}$. The magnitude of the cut is necessary (particularly in the Y-direction) due to uncertainties in (vertical) track matching [52]. This uncertainty can in unfortunate cases mistake a particle hitting the magnet, knocking out detector material, which continue further on into the spectrometer, for a particle just coming close to the magnet edge, but getting correctly bent. The fiducial cut helps to avoid this. Fig. 4.8 illustrates the fiducial cut for the D5 magnet.

4.5   Particle Identification

Discriminating between the relevant particle species is obviously a vastly important step in any analysis regarding identified particles. Particle IDentification (PID) is done by combining the momentum measurement in the dipole magnets, with a velocity (or solely velocity dependent quantity) measurement.

Velocity determination at BRAHMS is done by utilising either the TOF walls or the RICH detector. For the MRS solely the TOF wall is used, whereas either the TOFs or RICH is used in the FS depending on polar angle and magnetic field strength.

It should be noted that, throughout this analysis, when presenting plots from the MRS involving a momentum axis it does not truly show the momentum, but instead it shows the electrical charge times the momentum of the particle. This makes it possible to separate particles and anti-particles in the plots. Thus anti-particles will be shown as having negative momentum.

For the FS only particles OR anti-particles survives through the spectrometer for a given setting. In that case particle momentum will always be presented as positive. In this work only particles are investigated in the FS.

4.5.1   MRS PID Selection

In the MRS the TOF wall is used for the velocity determination, since the time-of-flight is measured and the travel distance to the TOF wall is well known. The mass-square, m^2, can then be calculated through the relation:
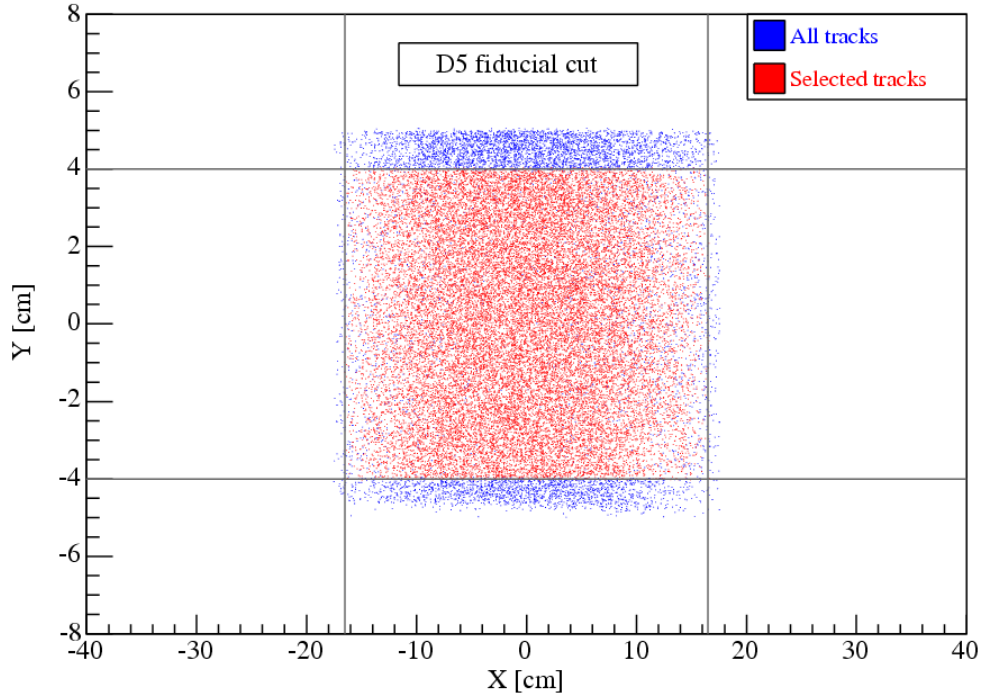
Figure 4.8: Illustration of the effect of the magnet fiducial cut. The dots are the track intersections the backplane of the D5 magnet. The lines denotes the applied cut, with the red points inside being the selected tracks. Figure taken from [52].

$$\begin{aligned} p &\equiv m\beta\gamma & \Leftrightarrow \\ m^2 &= \frac{p^2}{\beta^2\gamma^2} & \Leftrightarrow \\ m^2 &= p^2\left(\frac{1}{\beta^2} - 1\right) & \end{aligned} \qquad (4.4)$$

An example of the mass square versus the measured momentum distribution is shown in fig. 4.9. The top (and sparse) branch are identified as (anti-)deuterons with a m^2 around 3.5. At a m^2 of around 0.9 the (anti-)protons are located. Further down the kaons (K^- and K^+ respectively) are seen, and in the bottom branches pions (π^- and π^+ respectively).

It can be estimated through error propagation, that the momentum dependent width of the distributions can be parameterised as:

$$\sigma^2_{m^2} = 4\left(m^4 p^2 \sigma^2_{ang} + m^4\left(1 + \frac{m^2}{p^2}\right)\sigma^2_{mult} + (m^2 + p^2)^2 \sigma^2_t\right) \qquad (4.5)$$

σ^2_{ang}, σ^2_{mult} and σ^2_t denotes the track angular resolution, the angular smearing in regards to
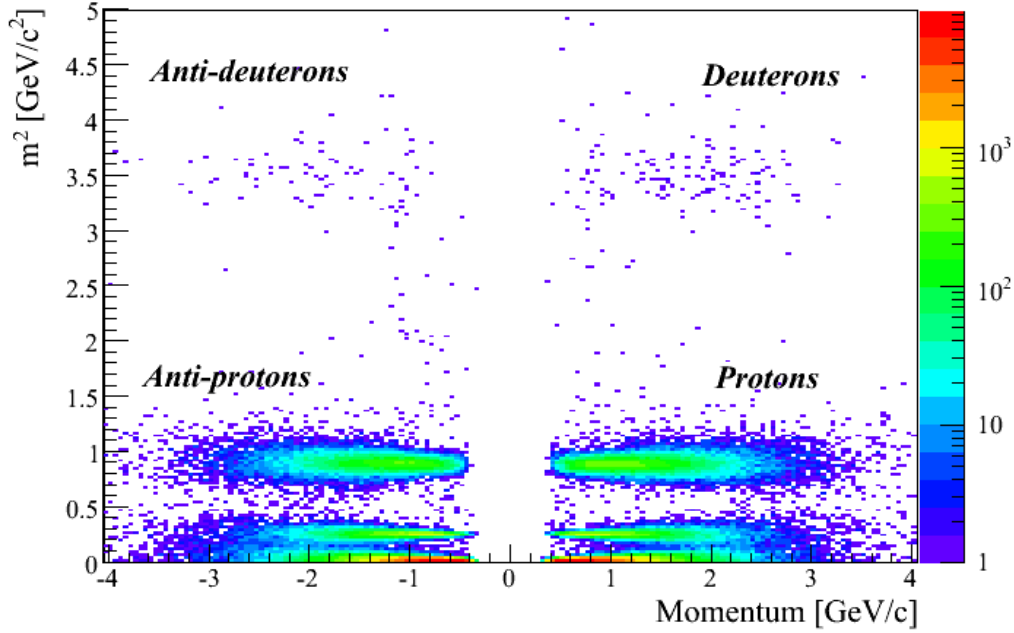
Figure 4.9: m^2 versus p in the MRS TOF wall. The (anti-)proton and (anti-)deuteron branches are roughly located under their names. The actual detailed identification will be presented later on. The data plotted are from 90B1050.

multiple scattering and the TOF wall resolution. For further discussion regarding the form of eq. 4.5 see [7, 25, 52].

Proton and Anti-proton PID

Selecting protons and anti-protons are done by slicing the m^2 versus p into five momentum slices. Each slice is then projected onto the m^2-axis and fitted to a Gaussian to obtain the width of the m^2 distribution at the mean momentum of that slice. Finally the obtained widths are fit to eq. 4.5. For the PID in the MRS a 2σ cut is used around the average mass found from the m^2 distribution. In appendix D an example of the fits to the momentum slices and the fit to the widths can be found.

When going to high p_T the proton and kaon branches becomes inseparable ($p_T \sim 3 - 3.5$ GeV/c), yielding a maximum range where the TOF wall PID method is applicable. For this work the exact location of this maximum p_T is not crucial, since only protons with $p_T < 2$ GeV/c are used further on to construct B_2. An example of the selected protons can be seen in fig. 4.10.
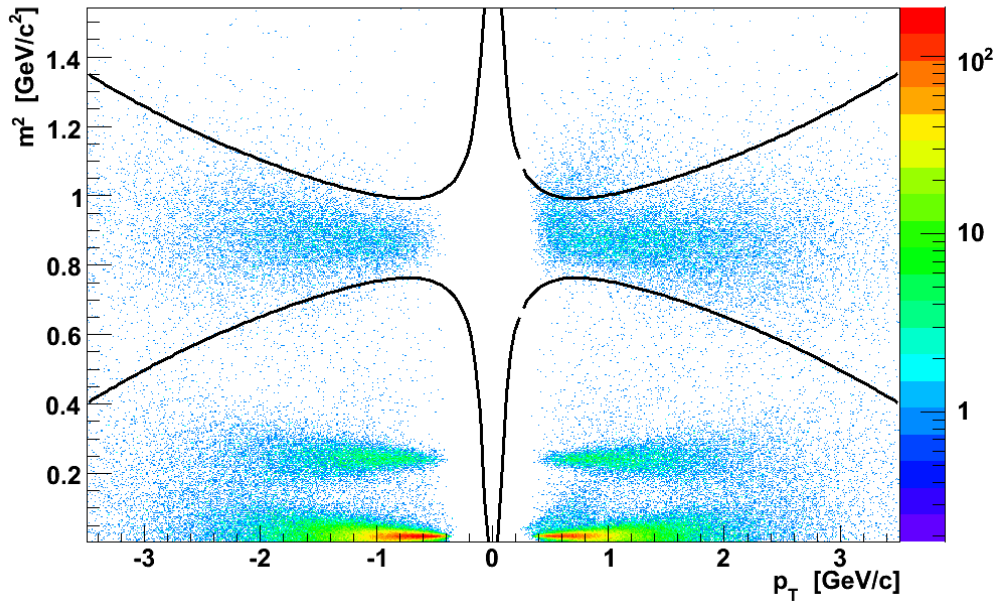
Figure 4.10: Selection of protons and anti-protons in the MRS. The selected particles are inside the curves. The curves marks a 2σ cut. The setting in the plot is 90B1050.

Deuteron and Anti-deuteron PID

The (anti-)deuterons are selected in a similar, but simpler fashion. Due to the scarcity in the m^2 versus p distribution, it is not possible to make slices as for the protons. Instead the entire momentum range is projected onto the m^2-axis, as seen in fig. 4.11, and fitted to a gaussian in the relevant m^2 range. The deuterons are then selected as being a linear cut in momentum $\pm 3\sigma$ from the mean value. This is a reasonable method since at that high m^2 the background is low, and there are no mixing between the deuteron and proton branches at the p_T ranges investigated.

In fig. 4.11 the selected (anti-)deuterons are shown as the shaded red gaussian area in the m^2 distribution. In fig. 4.12 the same selected (anti-)deuterons is shown in a m^2 versus p plot.

4.5.2 FS PID Selection

In the FS the two TOF walls (H1 and H2) and the RICH detector are used for velocity determination. For momenta in the range $4\,\mathrm{GeV/c} < p < 10\,\mathrm{GeV/c}$, H1 and H2 should be usable. They allow for PID in the same manner as for the MRS described in the previous section. In fig. 4.13 an example of PID in H1 and H2 is given. As can be seen, the uncertainty in the m^2 for the H1, makes it very hard to distinguish between protons and kaons at all. Thus it was chosen to only use H2 for FS TOF PID.

For particles with momenta $p > 10\,\mathrm{GeV/c}$ H2 PID also breaks down because separation
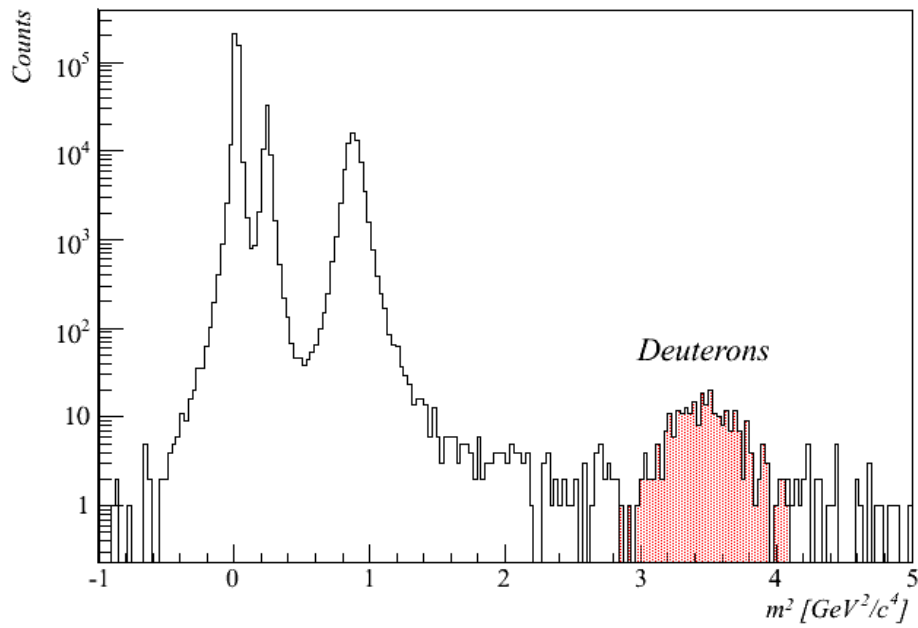
Figure 4.11: m^2 distribution for the MRS TOF wall. The shaded area illustrates the selected deuterons, within 3σ of the deuteron mean. The setting depicted is 90B1050.
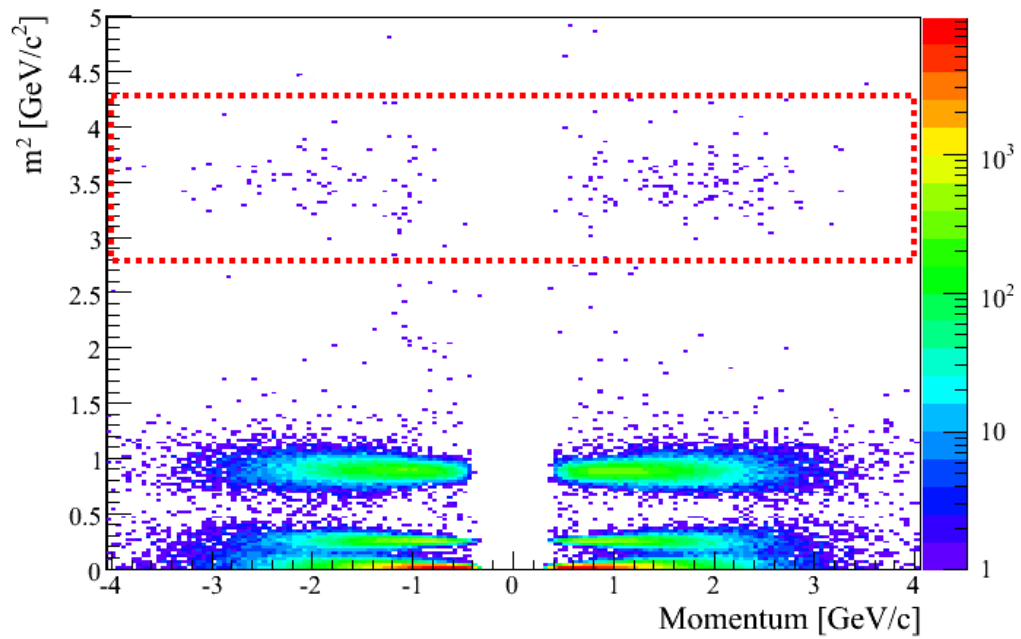
Figure 4.12: The m^2 versus p distribution for the setting 90B1050. The dashed red lines borders the area of the selected (anti-)deuterons, within 3σ of the deuteron mean m^2 found in fig. 4.11.
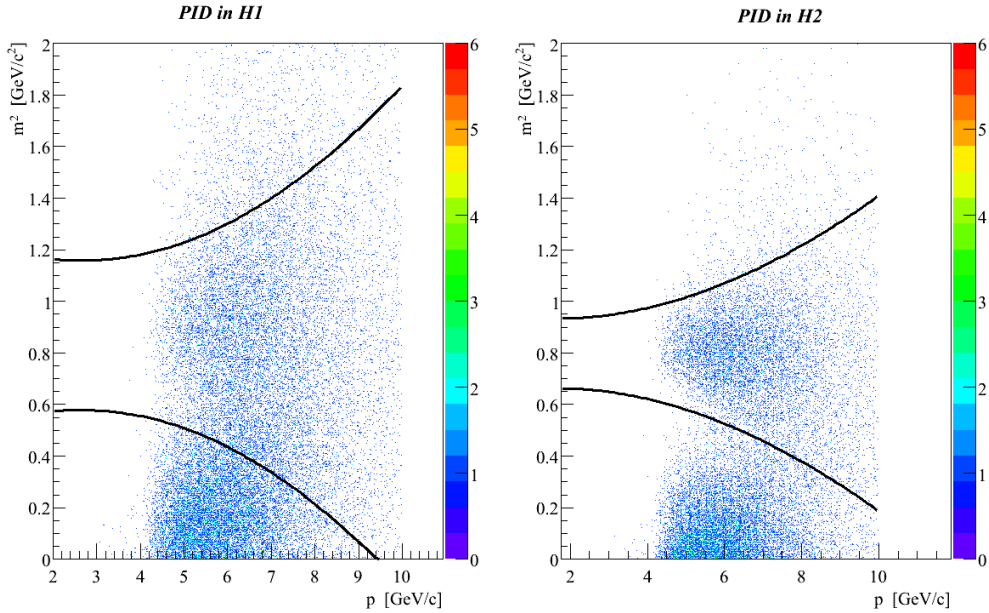
Figure 4.13: Plot of mass-square versus momentum for the FS TOF walls.   The
protons are identified as the top horizontal branch. Everything between
the curves are identified as a proton by H1 and H2 respectively. This
figure is for the setting 8B861.

between kaons and protons is no longer possible. For high momentum particles the RICH
detector is used for PID instead.

4.5.3   RICH PID Selection

For the highest momentum particles it is necessary to use the RICH to identify particles. As
touched upon in the previous sections, the time resolution of the TOF walls yields massive
uncertainties in particle velocities at high momentum.

The RICH allows PID by measuring the Čerenkov angle of the emitted Čerenkov radiation,
which gets focused to a ring in the RICH imaging plane. The expected ring radius of a particle
detected in the RICH is given by [52]:

$$r = L \cdot \tan \left(\cos^{-1} \frac{1}{n} \sqrt{1 + \frac{m^2}{p^2}} \right) \tag{4.6}$$

Here L is the focal length of the spherical mirror, n is the index of refraction of the gas, and
m,p is the particle's mass and momentum respectively.

Doing PID with the RICH consists of two methods, labelled the direct method and the
indirect method.

Direct RICH PID

The direct method of PID uses the RICH ring radius directly. In addition to the expected ring radius of eq. 4.5.3 two additional functions are used to select particles directly.

$$r_+ = L \cdot \tan\left(\cos^{-1}\left(\frac{1}{n}\sqrt{1 + \frac{m^2}{(p + \delta p)^2}}\right)\right) + \delta r \tag{4.7}$$

$$r_- = L \cdot \tan\left(\cos^{-1}\frac{1}{n}\sqrt{1 + \frac{m^2}{(p - \delta p)^2}}\right) - \delta r \tag{4.8}$$

These two functions are used as limits for each particle species, incorporating the ring radius uncertainty, δr, and the momentum resolution, δp. In fig. 4.14 the direct selection is illustrated.
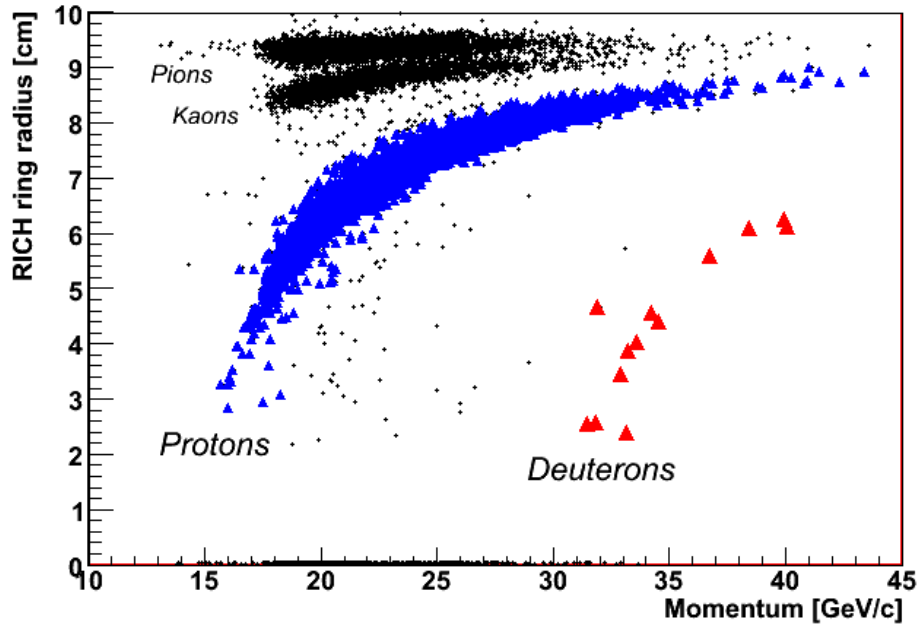
Figure 4.14: RICH direct PID selection. Protons and deuteron are identified by the ring radius assigned to them in the RICH.

The direct PID method can be used above the Čerenkov threshold, i.e. the minimum momentum which causes the particle to emit Čerenkov radiation. For protons this limit is approximately 15 GeV/c and for deuterons approximately 30 GeV/c.

Indirect RICH PID

The indirect method expands the PID offered by the direct method, by looking at particles which hit the RICH back plane, but does not get a ring radius assigned to them. This can

happen if a particle comes through the RICH with less momentum than the RICH threshold for that particle specie. For pions and kaons for instance, this threshold is about 3-4 and 8-10 GeV respectively meaning that above these thresholds all pions and kaons should emit a ring, if the RICH was 100% efficient. In reality the RICH has an efficiency of approximately 98% [7], which will be corrected for later. Thus in the momentum range from approximately 12-17 GeV/c only protons can be detected in the RICH back plane without emitting a ring[8]. The RICH can be said to veto out the lighter particles (kaons/pions). The reason for choosing 12 GeV/c as a lower boundary is to make sure that kaons near the threshold momentum, not getting a ring radius assigned, (maybe due to problems reconstructing a small ring, i.e. problems with the pixel resolution of the RICH CCD), are not misidentified as protons.

In theory it is possible to measure deuterons indirectly in the same manner, by looking in a p_T range where protons are sure to emit a ring. However in reality it becomes very tricky. As mentioned above the RICH is only 98 % efficient, which means that 2% of the protons does not get a ring assigned to them. Considering that there are approximately 100 times more protons than deuterons it is clear that identifying deuterons in this way is not possible, since there is a very considerable background of these RICH-inefficient protons[9].

4.6   Corrections

The data need to be corrected for various effects. These corrections will be presented in the coming sections. An overview of these corrections is:

- **GEANT corrections :** Simulations using GEANT to correct for physical effects like absorption, multiple scattering etc.

- **Acceptance corrections :** Correcting for the fact that that BRAHMS does only cover a limited solid angle.

- **Detector efficiency :** Correcting for the efficiency of the tracking detection.

- **Hyperon weak decay :** Correcting for overestimating the (anti-)proton measurements due to weak decay of hyperons into (anti-)protons.

4.6.1   GEANT Corrections

GEANT v3.21 [57] (GEometry ANd Tracking) is a series of simulation programs, who through Monte Carlo methods, are designed to be able to track elementary particles through an experimental setup to simulate detector responses. Monte Carlo methods are a widely used class of algoritms for simulations. They are distinguished from ohter simulations in that they are stochastic, i.e. being non-deterministic through the use of random numbers.

---

[8]Also deuterons and other light clusters will be found in this range in this way, but compared to the number of protons their contribution is very small ($\ll 1\%$).

[9]A quick comparison of numbers shows that the 'background' is even exceeding the deuteron signal.

In this work GEANT simulations with the exact BRAHMS geometry/setup is used to make corrections for physical effects such a multiple scattering, weak decay, hadronic interactions etc. in the detectors. This extension to GEANT is called BRAG (BRAhms Geometry). A distribution of particles are thrown through the BRAHMS geometry, where the mentioned physical effects are being simulated. At the end the particles which survive through the simulation is compared to the initial distribution, yielding an correction function. This function is then applied to the selected experimental data.
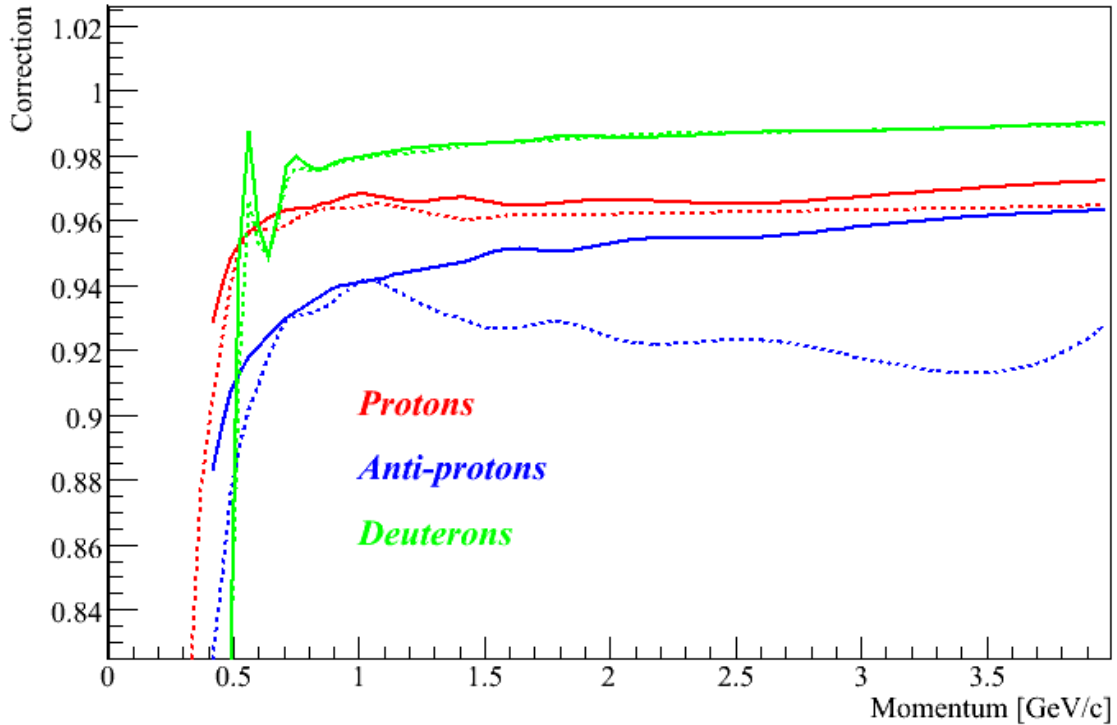
Figure 4.15: Example of GEANT correction functions for the MRS. Solid and dashed lines denote the correction function for 90°and 40°settings respectively. Protons, Anti-protons and deuterons are coloured red, blue and green respectively. It should be noted that the deuteron functions does not have absorption implemented.

Specifically the simulations used for this work takes into account multiple scattering, absorption, weak decays and energy loss in the detectors. GEANT, however, is not currently able to handle absorption for deuterons currently and anti-deuterons are not implemented at all. Thus it is necessary to estimate the GEANT corrections in those cases. These approximations are similar to what was done in the NA44 experiment [58].

First it is assumed that the absorption correction for deuterons can be factorized as the absorption correction for protons at half the deuteron momentum squared, i.e.
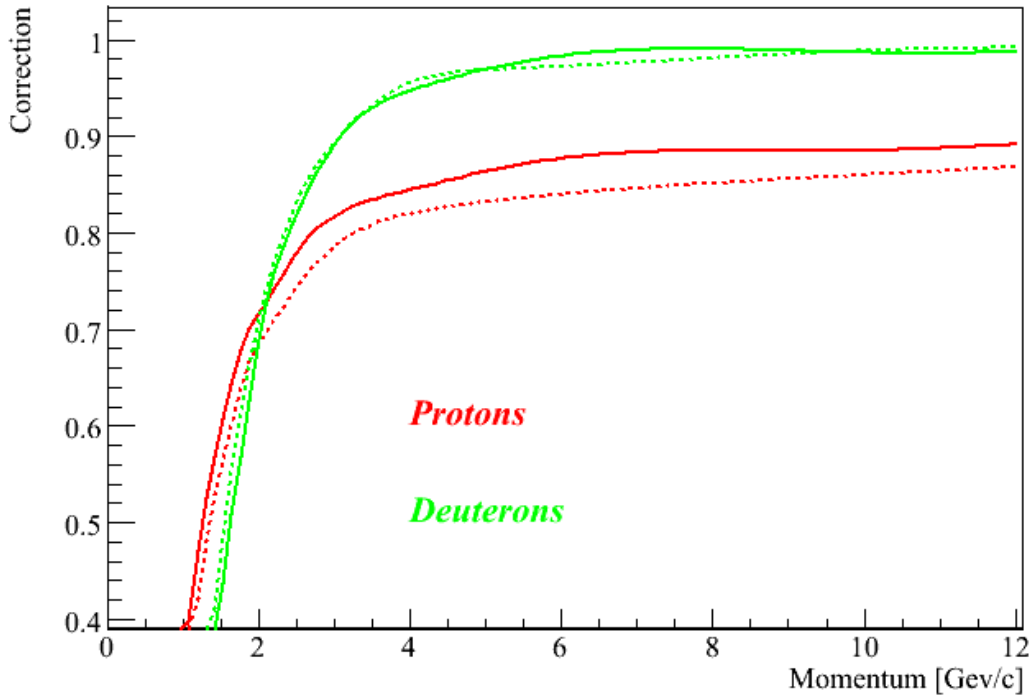
Figure 4.16: Example of GEANT correction functions for the FS. Solid and dashed lines denote the correction function for 8°and 4°settings respectively. Protons, Anti-protons and deuterons are coloured red, blue and green respectively. It should be noted that the deuterons functions does not have absorption implemented.

$$C_{abs-d}^{GEANT}(p_d) = (C_{abs-p}^{GEANT}(p_d/2))^2 \tag{4.9}$$

In the same manner it is assumed that the anti-deuteron absorption is factorised by the anti-proton absorption correction at half deuteron momentum.

The next assumption is that for the rest of the corrections there are no difference between deuterons and anti-deuterons, i.e. $C_d^{GEANT}(p_d) = C_{\bar{d}}^{GEANT}(p_{\bar{d}})$.

The resulting corrections becomes:

- Deuterons: $C_d^{\text{TOTAL}}(p_d) = (C_{abs-p}^{GEANT}(p_d/2))^2 \cdot C_d^{GEANT}(p_d)$

- Anti-deuterons: $C_{\bar{d}}^{TOTAL}(p_{\bar{d}}) = (C_{\text{abs-}\bar{p}}^{GEANT}(p_{\bar{d}}/2))^2 \cdot C_{\bar{d}}^{GEANT}(p_{\bar{d}})$

Fig. 4.15 and 4.16 shows the examples of the GEANT correction functions for the MRS and FS respectively. The shown deuteron function is only the GEANT correction for deuterons, i.e. not having the absorption in it. At low momenta it is seen that the deuteron function start

fluctuating in the MRS. For momenta lower than 0.5 GeV/c all the functions decrease rapidly. It is not possible to calculate the total deuteron correction lower than approximately 1 GeV/c, since it incorporates the absorption correction from protons at half momentum. Going lower than this momentum value would yield corrections larger than the measurements itself.

4.6.2 Acceptance

The data must also be corrected for geometrical acceptance. The acceptance is the probability that we detect a particle with a given p_T and y in our spectrometer. The acceptance is a purely geometrical quantity, and is calculated by simulations using the BRAG package. The concept of acceptance is illustrated in fig. 4.17. The acceptance vary with the collision vertex, so several mappings of acceptance is needed to cover the entire vertex range. In this work vertex bins of 5 cm is used, yielding 6 MRS acceptance maps in the vertex range [-15 cm;[15]cm] around the nominal IP.
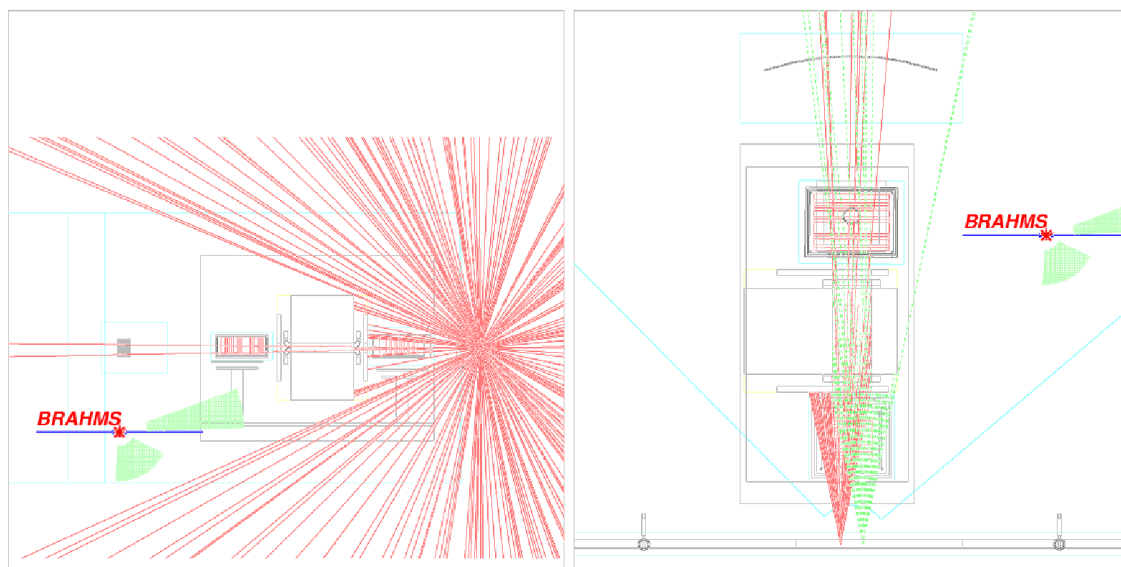
Figure 4.17: Illustration of the concept of geometrical acceptance in the BRAHMS experiment. On the right side is a top down view of the MRS spectrometer. The green and red cascades are the simulated particle distributions from two different vertices. It is seen that only a fraction of the simulated tracks survives through the spectrometer. This fraction is the acceptance.

The acceptance maps are 2D-histograms in p_T and y depicting the fraction of particles that are accepted by a given detector. For a range of given vertices the simulation throws a flat distribution (in p, θ and ϕ) of single particles into the solid angle of the first magnet gap. The acceptance is hence given as the number of particles surviving through the entire

spectrometer relative to the thrown distribution:

$$\mathcal{A}(y, p_T) = \frac{\text{Accepted}(y, p_T)}{\text{Thrown}(y, p_T)} \cdot \frac{\Delta\phi}{2\pi} \tag{4.10}$$

In eq. 4.10 the last factor originates from the fact that the thrown distribution (and the detector) does not cover the entire azimuthal angle.

Due to the fact that rapidity is mass-dependent, distinct acceptance maps have been created for each particle species. Fig. 4.18 shows an example of a proton acceptance map.
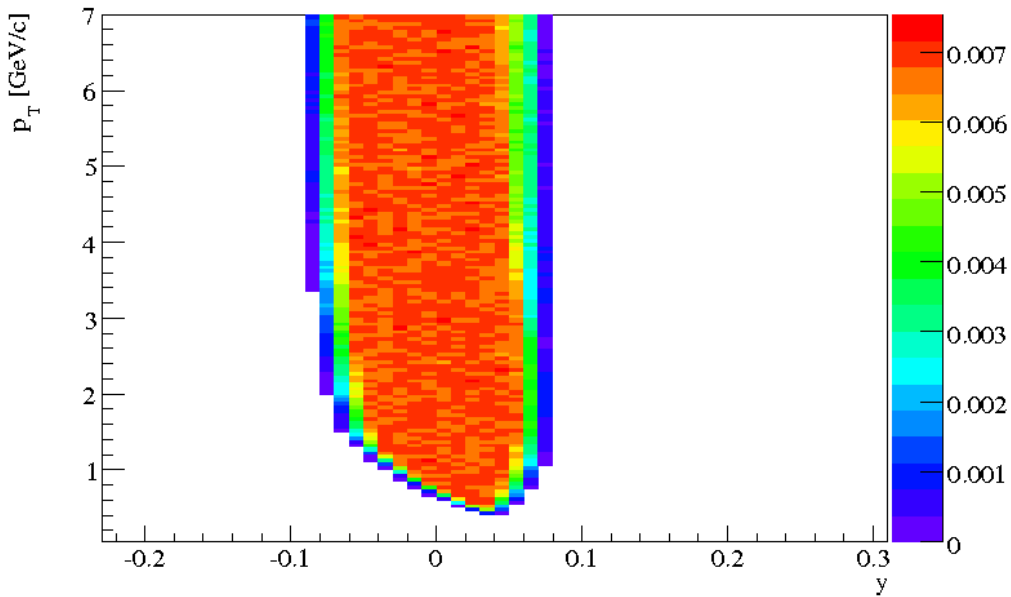
Figure 4.18: Proton acceptance map in the setting 90B1050 for the TOFW. The map is for the vertex bin [0cm;5cm]. The colour contour of each bin is the acceptance value.

4.6.3   Detector Efficiency

No detector is perfect. This is true for all experiments in physics including BRAHMS. In this section it is described how detector inefficiency is corrected for.

1. Simulate a large number of events making hits in all layers of the detector.

2. Reconstruct the hits, creating first local tracks, then global tracks.

3. Compare the number of reconstructed tracks to the number of simulated tracks.

In the FS a method known as the reference track method is used to compute the efficiency [7]. The idea is to build a track based on track segments from all tracking detectors in the FS except the one for which the efficiency should be calculated. This track is then compared to a track that includes the detector under study in the tracking. Now the efficiency for a single detector in FS (T1-T5,H1,H2) can be defined as [7]:

$$E_{\mathrm{rec}} = \frac{N_{\mathrm{local}}}{N_{\mathrm{r}ef}} \tag{4.11}$$

Here N_{local} is the number of tracks in the detector that matched the tracks constructed as described above. $N_{\mathrm{r}ef}$ is the number of these 'reference tracks'. The overall efficiency of the FS is then the product of the efficiencies of all the tracking detectors (T1-T5,H1,H2).

To implement the above and find the efficiencies using the reference track method a software package developed by Pawel Staszel for the BRAHMS Collaboration, was used to compute the efficiencies of all the tracks in the data set.

For the MRS the efficiency can be estimated to be the product of the efficiencies of the two TPCs. These are fairly constant at approximately 95%. Thus we have $E_{\mathrm{MRS}} = 0.95 \cdot 0.95 \approx 0.9$.

4.6.4 Weak Hyperon Decay

The measured protons can be divided into two categories:

- **Primary protons:** Protons which are created in the initial collision.

- **Secondary protons:** Protons being created when either Λ or Σ hyperons decay.

The possible decay channels for the Λ and Σ hyperons are [3]:

$$\Lambda \to p + \pi^- \ (64.1\%)$$
$$\Lambda \to n + \pi^0 \ (35.7\%)$$
$$\Sigma^0 \to \Lambda + \gamma \ (100\%)$$
$$\Sigma^+ \to p + \pi^0 \ (51.6\%)$$
$$\Sigma^+ \to n + \pi^+ \ (48.3\%)$$
$$\Sigma^- \to n + \pi^- \ (99.8\%)$$

The formation of the deuterons happens around the time scale of the QGP freeze-out after approximately 10^{-23} seconds ($\sim$ fm/c). The half-life for the Λ hyperons is of the order of 10^{-10} seconds. The half-life of the Σ's are shorter ($\sim 10^{-20}$), however most of them decay into a Lambda who then also decays. However still the half-life of the direct transition from Σ^+ to proton is much longer than freeze out time [3]. Thus the hyperons decay into secondary protons after the deuterons are formed but before the particles are detected in the spectrometers; thus increasing the measured proton distribution. This effect need to be corrected for. The correction, C, is of the form:

$$C = \frac{N_p}{N_p + N_\Lambda + N_{\Sigma^+}} = \frac{1}{1 + c_1 \cdot \frac{\Lambda}{p} + c_2 \cdot \frac{\Sigma^+}{p}} \tag{4.12}$$

Here N_p is primary protons, N_Λ is the protons coming from Λ decays, N_{Σ^+} is protons coming from Σ^+ decays. Thus $N_\Lambda = c_1 \cdot \Lambda$ and $N_{\Sigma^+} = c_2 \cdot \Sigma^+$ with the Λ and Σ^+ denoting the hyperon yields. c_1 and c_2 are the hyperon to proton decay channel probability for the Λ and Σ^+ respectively, i.e. $c_1 = 0.641$ and $c_2 = 0.516$.

Unfortunately the BRAHMS experiment can not measure the Λ and Σ^+ distributions[10].

Currently there is no published Λ/p-ratio for $\sqrt{s_{NN}} = 200\,\text{GeV}$, however the PHENIX collaboration have used an approach in [60], which is adopted in this work.

The main idea is to use the event generator HIJING [59] (Heavy Ion Jet INteraction Generator). HIJING simulates particle creation in heavy ion collisions through the use of Monte Carlo methods. A more elaborate discussion on HIJING can be found in [61].

What PHENIX did was to tune HIJING to produce their measured Λ/p-ratio for $\sqrt{s_{NN}} = 130\,\text{GeV}$ [62]. With this tuned HIJING they then calculated the Λ/p-ratio for $\sqrt{s_{NN}} = 200\,\text{GeV}$. PHENIX finds that $c_1\Lambda/p$ (where all hyperons decaying into Λ's are counted as Λ's, i.e. Σ^0, Ξ^0 and Ξ^-) is approximately 0.35 with a systematic error of 6%. The systematic error stems from varying the Λ/p-ratio for $\sqrt{s_{NN}} = 130\,\text{GeV}$ in the tuning of HIJING.

The Σ^+ distribution have not been measured at the RHIC. In thermal models [65] the ratio between Σ^+ and protons is predicted as $\frac{\Sigma^+}{p} \sim 0.1$ at $\sqrt{s_{NN}} = 130\,\text{GeV}$. These values are adapted for this work.

This yields $C \sim 0.75$, meaning that 25% of the measured protons stems from hyperon decays. It has been found that the correction is the same for $y \sim 0$ and $y \sim 3$ [7]. It is thus assumed that it is the same for all rapidities. It is also found that there are no significant differences in the correction for anti-protons and protons.

The hyperon decay correction is not included when presenting the spectra plots in the following chapter. This is chosen to present the actual measured invariant spectra (together with simulated corrections). Since the hyperon weak decay correction is very model dependent, and also fairly large, it is clear that small uncertainties in it would induce profound changes in the results. This is especially true when creating B_2, where the correction is squared. When proceeding onwards to the coalescence parameter plots, results will be presented both without and with the weak hyperon decay correction.

4.7 Creating Invariant Spectra

As discussed in sec. 1.4, the invariant spectra are defined as $\frac{d^2N}{2\pi N_{ev} P_T dy dp_T}$. Each spectra is ideally created in a narrow rapidity window (where statistics allow for this). For this work the following rapidity bins have been analysed:

- $-0.1 < y < 0.1$, corresponding to settings at $\theta = 90°$.

---

[10] An attempt was made in [66], but the small solid angle coverage of the detector makes it very rare that the two decay products can be detected in the spectrometer.

- $0.5 < y < 1$, corresponding to settings at $\theta = 40°$.

- $1.5 < y < 2.5$, corresponding to settings at $\theta = 8 - 10°$.

- $3 < y < 3.2$, corresponding to settings at $\theta = 2.3 - 4°$.

The rapidity intervals are not exactly narrow; especially for $y \sim 1$ and $y \sim 2$. The broad intervals are a necessary evil chosen to maximise the deuteron statistics.

The construction of spectra from the selected data is performed bin per bin. The spectrum is created by first correcting the data for efficiency, acceptance etc. as described above. The edges of the acceptance maps is cut away, to avoid areas where the acceptance changes rapidly over single bins. This is done to hinder that the uncertainty in the rapidity/momentum erroneously places a particle in a neighbouring bin with a vastly different acceptance. Finally the spectra are normalised to the bin-widths in p_T and the number of events measured.

Adding Overlapping Settings

Especially for the MRS different settings cover the same (y, p_T) region in phase space. The procedure of adding overlapping settings applied in this report, which is described in detail elsewhere ([7] and [52]), takes into account mixing of statistical errors, different weights of the data etc.[11]

Fig. 4.19 shows an example of overlapping settings, depicting the spectra ratios of the individual settings to the average of all the selected settings for the $40°$ selected protons. The average of all the settings is used from this point on to denote the particle spectrum at a given rapidity. As seen in fig. 4.19 there is an excellent agreement between the individual settings and the average for a large range in p_T.

4.8 Yields

From the invariant spectra $\frac{dN}{dy}$ can be obtained. As BRAHMS does not cover the entire p_T range of interest, extrapolation of the data is required to enable the integration of the invariant spectra. For this purpose several fit functions can be used. The primary fit function chosen in this work is an exponential in m_T:

$$f(m_T) = \frac{Y}{2\pi T(T + m)} \cdot e^{-\frac{m_T - m}{T}} \tag{4.13}$$

Here m is the (anti-)particle mass.

Other function are known to describe the data well; amongst them a Boltzmann in m_T:

$$f(m_T) = \frac{Y}{2\pi T(2T^2 + 2Tm + m^2)} \cdot m_T \cdot e^{-\frac{m_T - m}{T}} \tag{4.14}$$

---

[11]The procedure is implemented in the original version of the software used for the analysis in this work so there was found no need to change it nor claim credit for it
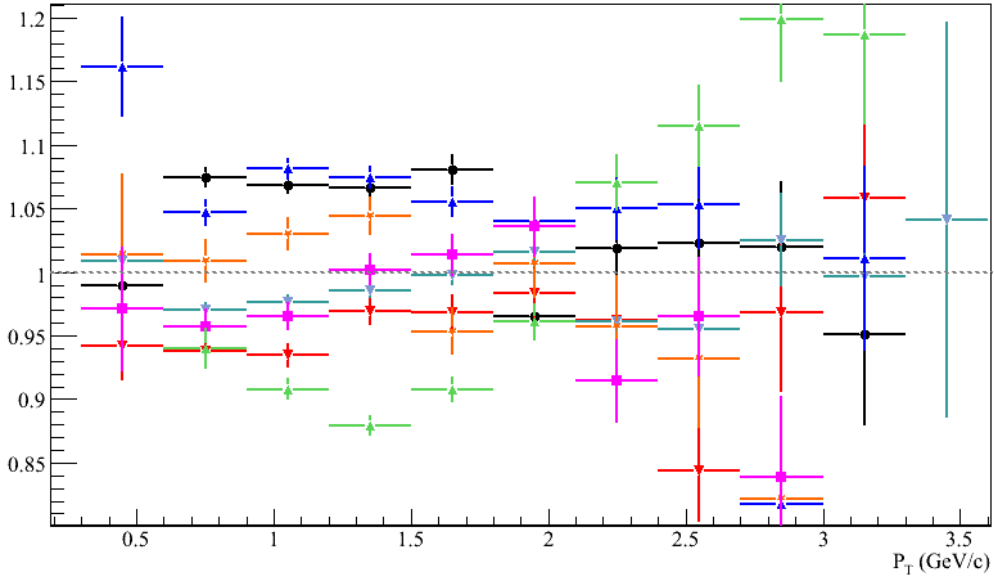
Figure 4.19: The ratio between the spectra of the individual settings and the average of the settings. This plot shows the proton spectra in the $\theta = 40°$ settings. It is found that all the individual settings are in excellent agreement.

and a Gaussian in p_T:

$$f(p_T) = \frac{Y}{2\pi T^2} \cdot e^{-\frac{p_T^2}{2T^2}} \tag{4.15}$$

All three functions are parameterised in such a way that the fit parameters are the extrapolated yield (Y) and the inverse slope parameter (T). For further details on this consult [7].

The fit functions all describe invariant spectra well [7]. χ^2-wise the Boltzmann and Exponential are very similar over the whole p_T range, whereas the Gaussian describes the low p_T regions well, but fail considerably at large p_T for the protons. For the deuterons the Gaussian is actually marginally better than the other functions over the entire p_T range. This would be an interesting thing to study further in another work.

The decision to choose eq. 4.13 as the primary fit function instead of the Boltzmann, considering their similar χ^2, was influenced by previous work implementing it as main fit function [7].

The extrapolated yield results from the exponential can be seen in the results chapter in tab. 5.1. Similar tables for the other two fit functions can be found in appendix C.

4.9 Errors

This section is devoted to describing how errors are handled. Basically errors can be divided into two categories; statistical and systematic errors. Statistical errors are random fluctuations in measurements due to the normality of the error. Statistical errors are almost always defined by Gaussian distributions[67]. The statistical error scales as the square-root of measurements as usually in Poisson statistics. Thus increasing the amount of measurements yields smaller errors, thereby increasing the precision. This is not the case for systematic errors. They denote uncertainties where the size and/or bias of the effect is not known. A rule of thumb is that if the extent of a systematic effect is known, it should be corrected for. Refining experiments or correcting for systematic effects decreases the systematic uncertainties, thereby increasing the accuracy of the measurement.

Propagation of uncorrelated errors are governed by the general formula[67]:

$$\partial q = \sqrt{\left(\frac{\partial q}{\partial x}\partial x\right)^2 + ... + \left(\frac{\partial q}{\partial z}\partial z\right)^2} \tag{4.16}$$

Here q, x and v denote quantities, with errors ∂q, ∂x and ∂v. If the measurements are correlated extra terms are added containing the covariances. These vanish for uncorrelated quantities.

Thus for error propagation of simple additive quantities ($q = x + ... + v$) it simplifies to adding in quadrature:

$$\partial q = \sqrt{\partial x^2 + ... + \partial z^2} \tag{4.17}$$

This is used very often (though most of the time automatically by ROOT) when adding histogram bins, re binning etc. For multiplicative error propagation ($q = x \cdot ... \cdot v$), i.e. error contributions from for instance multiplicative corrections, eq. 4.16 becomes:

$$\frac{\partial q}{q} = \sqrt{\left(\frac{\partial x}{x}\right)^2 + ... + \left(\frac{\partial z}{z}\right)^2} \tag{4.18}$$

Systematic Effects

In the following an estimate of the systematic effects will be presented. This will be used to estimate the systematic error on the B_2 results presented in the next section.

We start out by revisiting fig. 4.19 showing the ratio between individual overlapping settings and their average. This will give a good estimate of the systematics, since by definition it should be exactly unity if we had a perfect spectrometer, i.e with no systematic effects (and lots of statistics). It is found that for the MRS 40°settings, the systematic differences from the average is approximately 10% over a large p_T range. Similarly it is found, that the systematic error from this method for the most forward FS settings is approximately 20%.

This approach covers most of the systematic effects, like for instance uncertainties in the sub-detectors (angular resolution, vertex resolution etc.) and in track by track corrections

(acceptance, efficiency etc.). An advantage to this simple approach is, that it is not needed to consider whether the individual contributions are correlated or not. It basically estimates the magnitude of the error, but not the origin (this is of course not optimal if one is looking for a particular effect instead of solely the total systematic error).

Another concern one might have using the ratios for the estimate is if systematic effects, which are biased towards raising/lowering the spectra, exists. These would not show up since all settings would be shifted in the same direction. It should however be noted, that adding an estimate of each individual contribution in quadrature yields a systematic error in agreement with the ones obtained by the ratio approach, why it seems unlikely that any such bias (of significant magnitude) is being missed.

This systematic error contribution applies to all particle species. However when doing B_2 the error cancels out in the ratio between deuterons and protons. Left is then just the 'extra' remaining proton part. This means that the systematic error contribution on B_2 ends up being 10% and 20% respectively.

Besides the already mentioned systematic effects one have to consider corrections which are applied to the entire spectra as a function. The function parameter uncertainties must be considered as systematic effects. Most notably in this category are the hyperon weak decay correction and the GEANT correction for absorption, multiple scattering etc. For the hyperon decay it is found, that the systematic error on the $\frac{\Lambda}{p}$ is 6% [60], as mentioned in the sec. 4.6.4.

The systematic error on $\frac{\Sigma^+}{p}$ cannot easily be estimated since it not measured. However in the hyperon correction factor the Σ^+ term is much smaller than the Λ term. Therefore it is reasonable to neglect the systematic error on the Σ^+ term.

Thus the total systematic error contribution from hyperon decays is approximately 6%. This systematic effect does only apply for (anti-)protons, why each (anti-)proton contribution in B_2 is added using eq. 4.18. Thus the resulting systematic error on B_2 from this contribution is approximately 8%.

For the GEANT corrections the relative error on the fit parameters are of the order of 1%, which negligible compared to the hyperon decay contribution. This gives a total systematic error of 13% and 22% in the MRS and FS respectively.

These systematic errors will be applied to the B_2 plots presented in the next section. However combining the statistical and systematic error is not trivial. Often in the literature two ways of doing it are found, either by adding them linearly or in quadrature. Doing the latter requires that the systematic errors are in fact Gaussian in nature; this is not always the case (and/or not always known).

The approach chosen here will be to add them in quadrature, since it is estimated that the majority of the systematic error are indeed Gaussian.

Thus the total error becomes:

$$\epsilon_{\mathrm{Total}} = \sqrt{\epsilon_{\mathrm{Stat}}^2 + \epsilon_{\mathrm{Syst}}^2} \qquad (4.19)$$

The total error will only be used when plotting, for listing results both errors will be listed separately. In tab. 4.1 an overview of the systematic errors used in this work is given.

y-interval	$\epsilon_{\text{sys}}\ [\%]$ (no WDC)	$\epsilon_{\text{sys}}\ [\%]$ (with WDC)
-0.1< y <0.1	10	13
0.5 < y <1.0	10	13
1.5 < y <2.5	20	22
3.0 < y <3.2	20	22

Table 4.1: Overview over the systematic error estimates used on B_2 in this work for all rapidities. In the table 'WDC' indicate if the error is including hyperon Weak Decay Correction contributions or not.

Chapter 5

Results and Discussion

The following sections are devoted to presenting and discussing all the results of this analysis. The first results presented will be the invariant particle spectra, which are used to create distributions of B_2 versus p_T. They are fitted to obtain the overall B_2 value for a given rapidity bin. Finally the obtained results will be compared to previous measurements and the source size will be estimated from the models presented earlier.

5.1   Invariant Spectra

Particle spectra are presented for the four rapididity bins presented in sec. 4.7. As stated previously this work analyses the 0-20% most central collisions in Au-Au collisions at $\sqrt{s_{NN}} = 200$ GeV. In fig. 5.1 the particle spectra are shown. All anti-particle spectra have been scaled with a factor of $\frac{1}{2}$ to help distinguish them from the particle spectra. The spectra presented have not been corrected for weak hyperon decays. Tab. 5.1 shows the characteristics of each spectra; i.e. fit parameters, extrapolated yield, inverse slope parameter and the fit χ^2. The results in tab. 5.1 are from fitting the data with a exponential in m_T. In appendix C the same quantities are presented for a Boltzmann and Gaussian fit.

As can be seen in fig. 5.1 excellent p_T coverage exist for both protons/deuterons and their anti-particle counterparts in the two MRS rapidity bins. However at p_T above 3.0 GeV/c especially the (anti-)deuteron spectra starts to fluctuate. It is mainly seen as a statistical issue. For instance one might notice that in the deuteron spectrum at $y \sim 0$ no deuterons at all are found in the bin starting at $p_T = 3.5$ GeV/c. Similarly for anti-deuterons the bin around 3.2 GeV/c differs significantly compared to the trend seen in the spectrum. This will be an issue later on, where very high p_T deuterons are compared to lower p_T deuterons in creating the B_2 versus p_T distributions.

The spectra shown in fig. 5.1 for the FS are very different from the MRS ones. First of all it has not been possible to identify enough anti-deuterons to use further on. This means that for forward rapidities no anti-particle spectra are presented.

At $y \sim 2$ the protons can only be seperated from the kaons by the TOF wall up until approximately $p_T \sim 1.4$ Gev/c. A RICH detection is in principal possible for the very high momenta protons (above $p_T \sim 2.3$), but it has been omitted in this work. This is done since
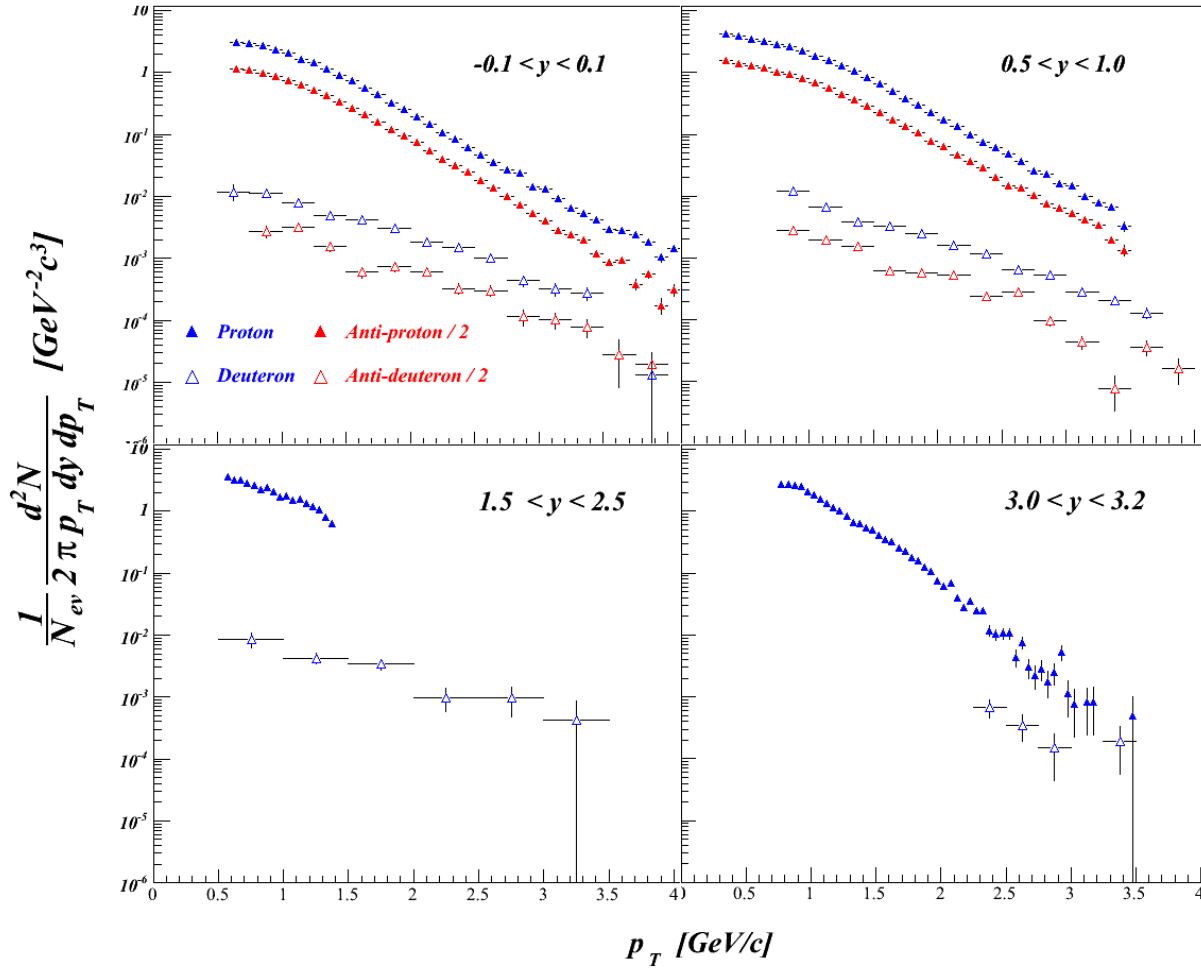
Figure 5.1: The invariant spectra for all four rapidity bins. It should be noticed that the anti-particle spectra have been scaled by a factor of $\frac{1}{2}$, to help distinguishing particle/anti-particle spectra.

the statistics were poor and the p_T-range could not be used for creating B_2 anyway. While the TOF proton range is limited due to the p/K separation, the deuterons does not suffer from this, since the gap m^2-wise between the proton and deuterons branches are sufficiently large.

At the most forward rapidity bin the proton range is quite large, whereas the deuteron range is limited to only very high p_T. Unfortunately, as mentioned in sec. 4.5.3, the indirect RICH PID method can not be applied to the deuterons, extending the meassurable range downwards. Thus only directly identified deuterons (which must have very high momentum) are shown.

Rapidity interval	Part.	Fit range [Gev/c]	Extrapolated yield	Inverse slope parameter (T)	χ^2/ndf
$-0.1 < y < 0.1$	p	$1.0 < p_T < 4.0$	23.8 ± 0.1	346.6 ± 0.9	$375/118$
	$\bar{p}$	$1.0 < p_T < 4.0$	17.9 ± 0.1	342.0 ± 1.0	$483/118$
	d	$1.0 < p_T < 4.0$	0.099 ± 0.005	291.4 ± 9.8	$26/10$
	$\bar{d}$	$1.0 < p_T < 4.0$	0.047 ± 0.003	343.7 ± 22.0	$29/10$
$0.5 < y < 1.0$	p	$1.0 < p_T < 3.5$	21.2 ± 0.05	352.2 ± 0.4	$771/98$
	$\bar{p}$	$1.0 < p_T < 3.5$	15.1 ± 0.04	350.0 ± 0.6	$575/98$
	d	$1.0 < p_T < 4.0$	0.077 ± 0.002	345.3 ± 9.6	$16/9$
	$\bar{d}$	$1.0 < p_T < 4.0$	0.043 ± 0.002	276.9 ± 8.9	$82/10$
$1.5 < y < 2.5$	p	$0.6 < p_T < 1.2$	18.0 ± 0.3	417.0 ± 15.9	$26/10$
	d	$1.0 < p_T < 3.5$	0.074 ± 0.010	383.6 ± 90.6	$2.8/3$
$3.0 < y < 3.2$	p	$1.0 < p_T < 3.0$	21.1 ± 0.3	251.0 ± 1.7	$134/38$
	d	$2.2 < p_T < 3.6$	0.046 ± 0.028	451.0 ± 328.6	$0.45/1$

Table 5.1: Overview over fit results for all spectra. The fit functions used are expontials in p_T. In appendix C similar tables for other fit functions can be found.

5.2 B_2 **versus** p_T

Taking the meassured p_T ranges of each spectrum into account limits the range where it is possible to compute B_2. As mentioned previously it is important that relevant p_T intervals is used when calculating B_2. Thus deuterons in the p_T interval $[x_1; x_2]$ must be coupled to protons in the p_T interval $[\frac{x_1}{2}; \frac{x_2}{2}]$. In Fig. 5.2 the selected (anti-)deuteron/(anti-)proton p_T intervals used for constructing the B_2 versus p_T is shown. The colored part of each spectrum highlights the selected interval, whereas the shaded parts lies outside the useable range. The resulting B_2 versus p_T distribution can be seen for all four rapidities in fig. 5.3. It is seen, that for the two mid-rapidity intervals B_2 is slightly rising with p_T for both particles and particles. Also an excellent agreement between particles and anti-particles is found.

For the forward rapidities it is not possible to conclude anything on the p_T dependence of the B_2, since the possible matching of the various p_T-ranges of the particle spectra is far from optimal.

5.3 B_2 **versus** y

The next step is to convert the B_2 versus p_T distributions into a single 'mean' B_2-value for each rapidity bin. There are several considerations to be made on how to perform this conversion. If one have well defined B_2 versus p_T distributions over a large p_T range for all the rapidities, it might be possible to fit the distributions to an analytical function and then evaluate that function at a specific p_T. This would be the optimal solution, but also require really high
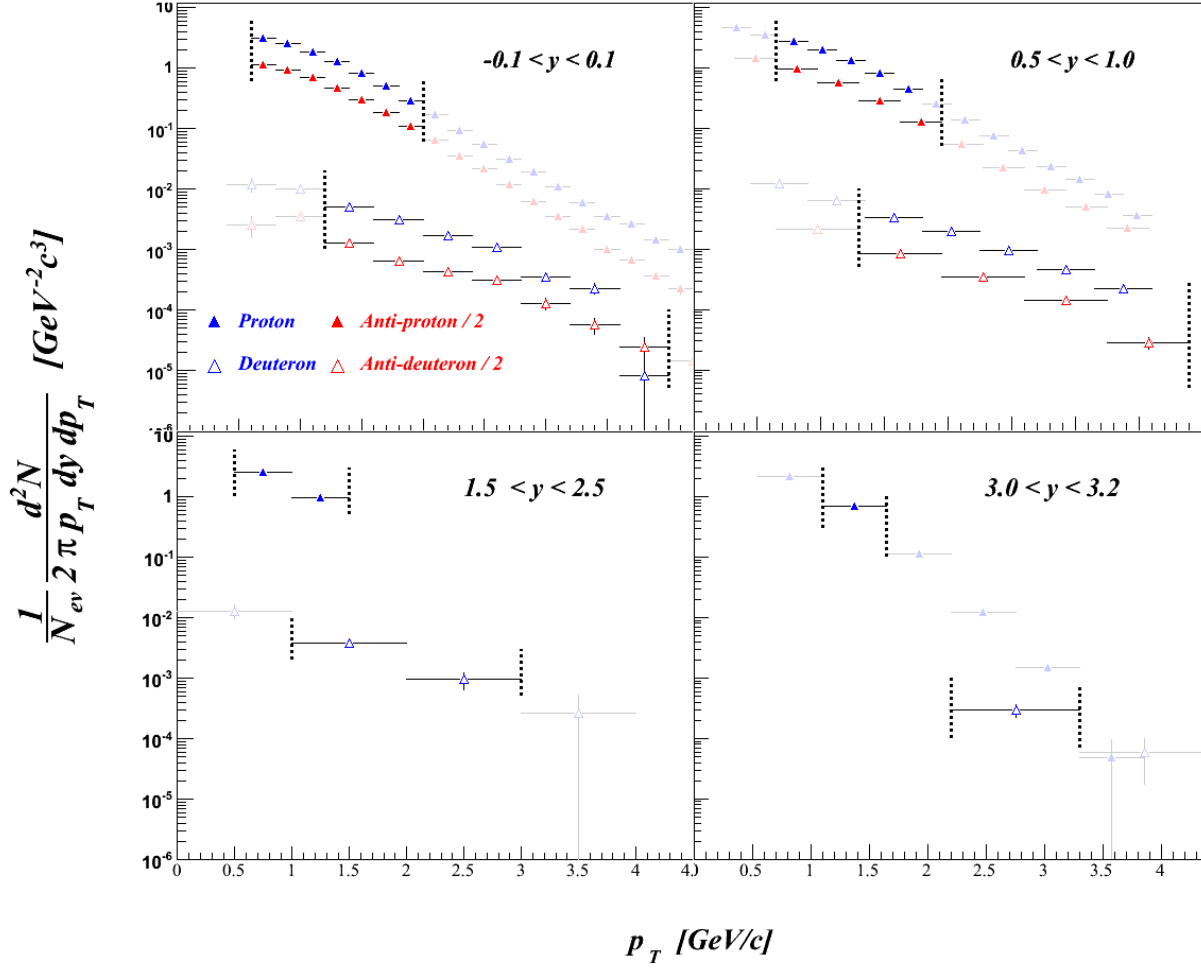
Figure 5.2: The invariant spectra for all rapidities. Here the spectra is shown in the binning used to calculate B_2 versus p_T. For each spectrum the colored range shows the exact p_T range used further on to create B_2. The shaded ranges can not be used.
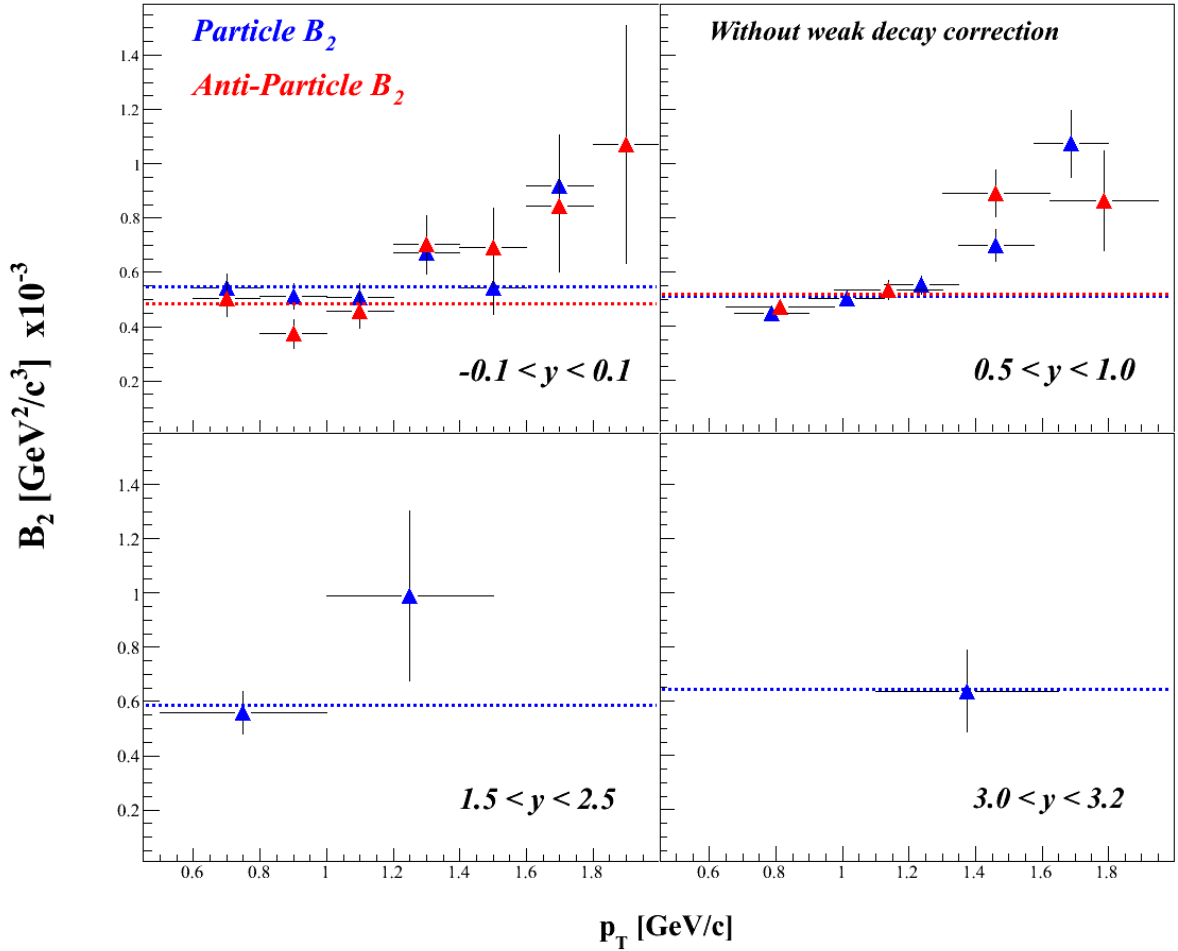
Figure 5.3: The B_2 versus p_T distributions for all rapidities. A rising trend is seen in the MRS for both particles and anti-particles. In the FS it is not possible to conclude anything about the p_T dependence. The dashed lines denotes the weighted mean of each distribution. The distribution has not been corrected for weak hyperon decays.

statistics over a broad range of p_T and y. In the case of this work it is not a viable option, since the FS distributions consists of two and one point respectively. This renders it impossible to fit the FS distributions to any reasonable extent.

Another approach could be to find a p_T value common to all rapidiy bins (if possible) and then compare directly at the selected value. This would indeed be a direct comparison, but to be able to include the the most forward point, one would have to choose a p_T above 1.1 GeV/c which in the other rapidity bins are outside the statistical bulk. Thus following this approach might be a direct comparison between rapidities, but it would also have large statistical errors assigned to the results. A third possible approach would be to get the weigthed mean of each

Figure 5.4: B_2 as a function of rapidity. It is found that there is no rapidity dependence of B_2. The error bars are statistical, whereas the shaded areas denotes the total error.

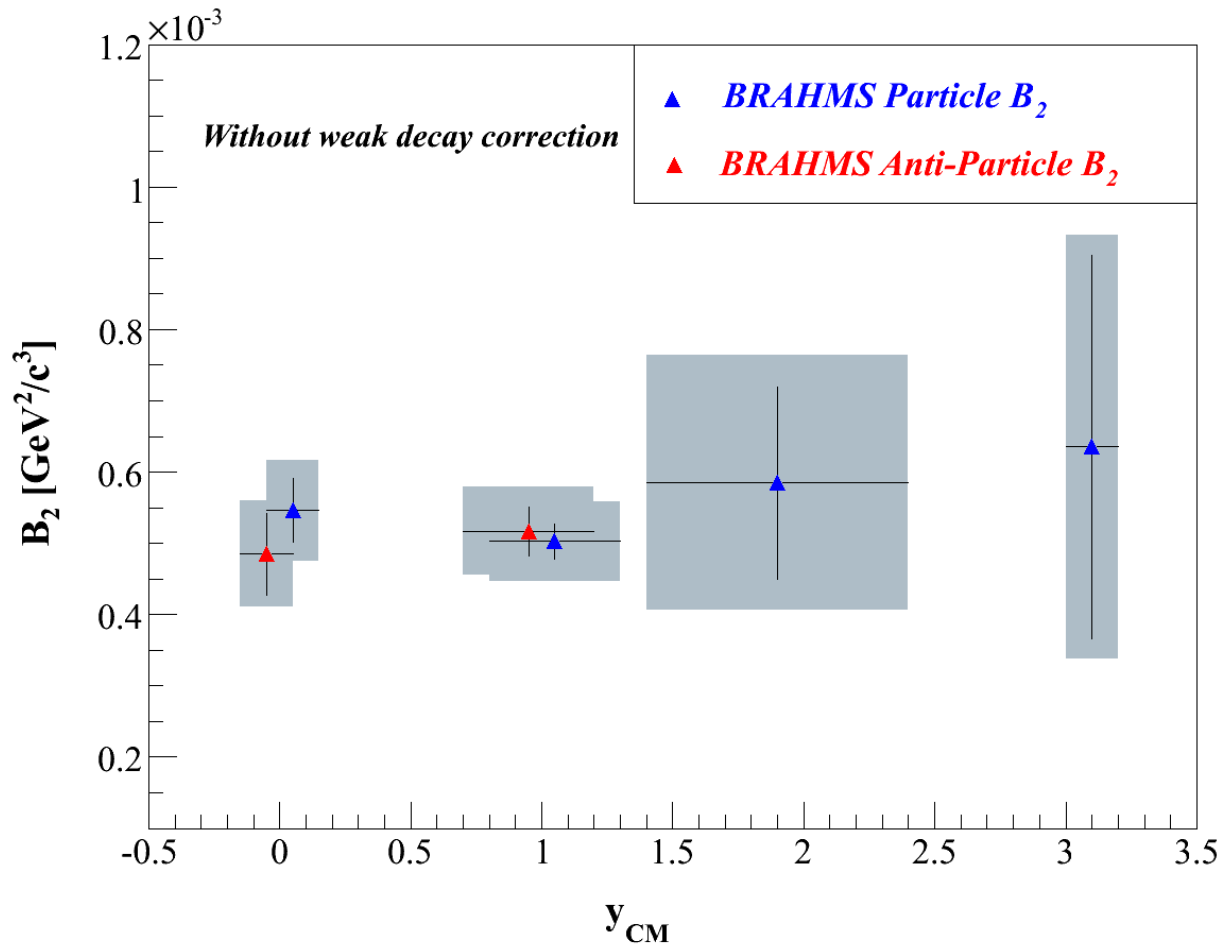| y-interval	Particle B_2 $[GeV^2/c^3]$	Anti-particle B_2 $[GeV^2/c^3]$
Corrected for hyperon weak decay		
-0.1< y <0.1	$(9.7 \pm 0.45 \pm 1.3) \cdot 10^{-4}$	$(8.62 \pm 0.57 \pm 1.1) \cdot 10^{-4}$
0.5 < y <1.0	$(8.94 \pm 0.25 \pm 1.2) \cdot 10^{-4}$	$(9.19 \pm 0.35 \pm 1.2) \cdot 10^{-4}$
1.5 < y <2.5	$(1.04 \pm 0.14 \pm 0.23) \cdot 10^{-3}$	-
3.0 < y <3.2	$(1.13 \pm 0.27 \pm 0.25) \cdot 10^{-3}$	-
Without weak decay correction		
-0.1< y <0.1	$(5.46 \pm 0.25 \pm 0.55) \cdot 10^{-4}$	$(4.85 \pm 0.32 \pm 0.49) \cdot 10^{-4}$
0.5 < y <1.0	$(5.03 \pm 0.14 \pm 0.50) \cdot 10^{-4}$	$(5.17 \pm 0.19 \pm 0.52) \cdot 10^{-4}$
1.5 < y <2.5	$(5.85 \pm 0.76 \pm 1.09) \cdot 10^{-4}$	-
3.0 < y <3.2	$(6.36 \pm 0.15 \pm 0.13) \cdot 10^{-4}$	-

Table 5.2: The mean values of the B_2 versus p_T distributions for all the rapidity bins. The top section are corrected for hyperon weak decay, whereas the lower part is not. The errors are statistical and systematic respectively reading from left to right.

distribution. This would be a viable solution if the various rapidity bins had approximately the same p_T range and if the amount of statistics as a function of p_T is somewhat similar, i.e. that the lower p_T bins have the most statistics etc. This is indeed a good measure for the three first rapidity bins ($y \sim 0 - 2$), since the error assigned to the total B_2 would be smaller than the above method due to the weights of the high statistics p_T-bins. However the most forward bin only have one point at $p_T = 1.4$ Gev/c. This means, that if the trend from the MRS is applicable to FS too, we are lacking a low p_T bin with more statistics and probably also a lower B_2 value. Thus using this method one must keep in mind that the most forward bin will probably be overestimated compared to the other rapidity bins.

It is clear that all three approaches described have both pros and cons in regards of the data sets at hand. The latter approach have been chosen in this work. The weighted means are included in fig. 5.3 as dashed lines in the color of the individual B_2 distribution.

In tab. 5.2 the mean value at each rapidity obtained from fig. 5.3 is presented. The B_2 versus y distribution is plotted in fig. 5.4. The error bars denote the statistical error, whereas the shaded areas denotes the total error.

It is found that the particle and anti-particle B_2 are in agreement with each other at both mid-rapidity bins.

Furthermore is it found that there is no rapidity dependence within the uncertainties of B_2. As mentioned one must keep in mind that the conversion method from B_2 versus p_T is probably biased towards overestimating the most forward rapidity point. The effect of this bias is not known but it is estimated that it is not more than maximum 10%. Even without correcting for it the there is no measurable rapidity dependency of B_2, due to the large errors at forward rapidities.

5.4   Comparisons with Other Experiments

The previous section presented the core measurements done in this work. In this section the results will be compared to other coalescence measurements. First the results are corrected for the weak hyperon decay as discussed in sec. 4.6.4, to allow for a direct comparison with PHENIX results. The correction is applied in fig. 5.5 and 5.6 showing the B_2 versus p_T and y distributions respectively. In fig. 5.6 is also included the coalescence parameters deduced from the PHENIX measurements of B_2 versus p_T at mid-rapidity[68]. The PHENIX points have been treated in the same way as the BRAHMS data by taking the mean value of the p_T distribution. The errors on the PHENIX points are the total error.
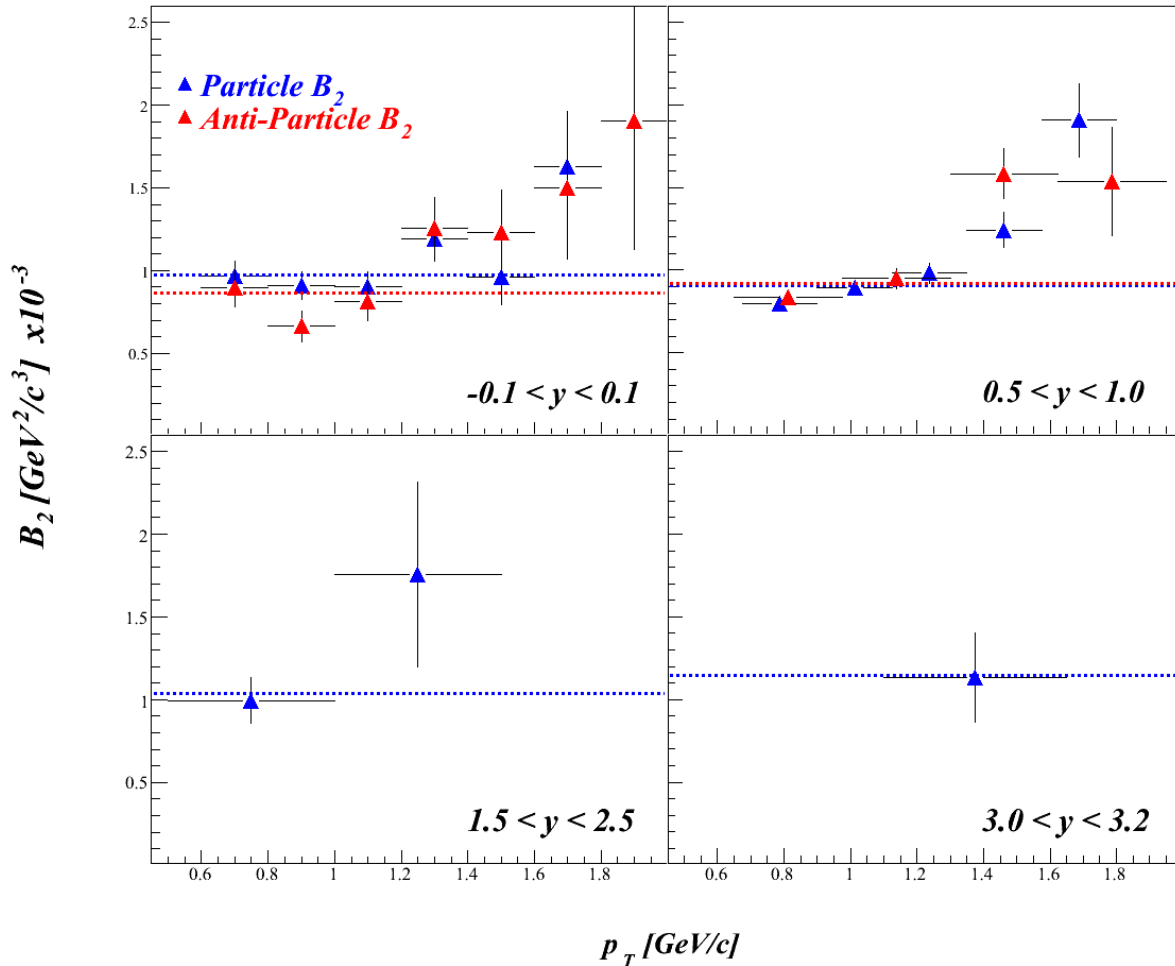
Figure 5.5: The B_2 versus p_T distributions for all rapidities corrected for weak hyperon decays. The dashed lines denotes the weighted mean of each distribution.
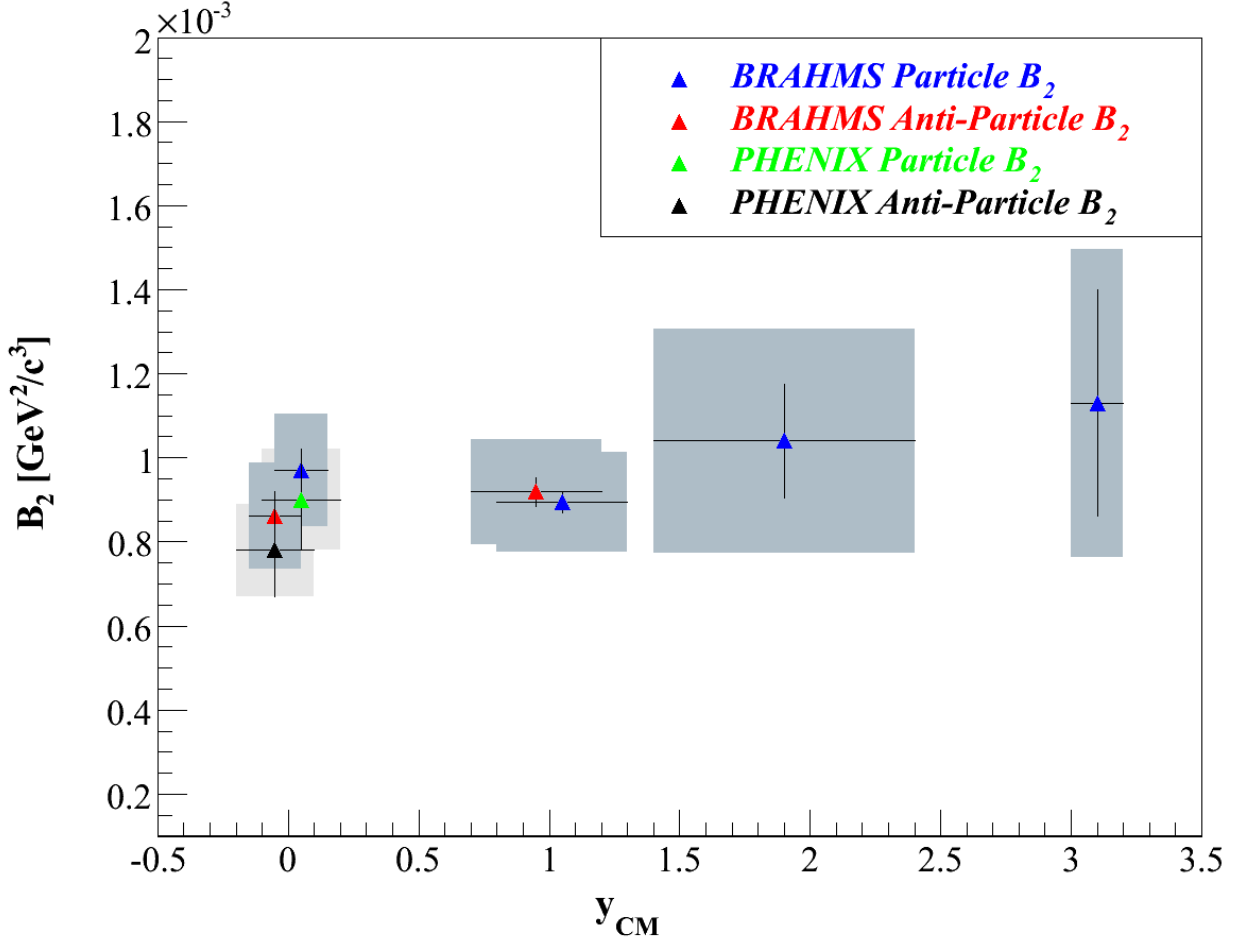
Figure 5.6: B_2 as a function of rapidity corrected for weak hyperon decays. Included in the figure is also the coalescence results by PHENIX [68] at mid rapidity. The error bars are statistical, whereas the shaded areas denotes the total error.

It is seen that there is agreement between the two data sets at $y \sim 0$.

Let us look a little closer at the PHENIX results again before turning to comparing with more experiments. Fig. 5.7 shows the published PHENIX B_2 versus p_T directly compared to the BRAHMS distributions. It is seen that also the p_T dependency is in good agreement. One thing to be mentioned though is, that in the lower p_T range it seems that the meassured BRAHMS distributions are flatter than the PHENIX distributions. However it might turn out to be just fluctuations; more measurements are needed to conclude if there truly are significant differences. Another point worth mentioning is the highest p_T points for particles which differs quite much. However it must be noted that the BRAHMS point consist of only one single
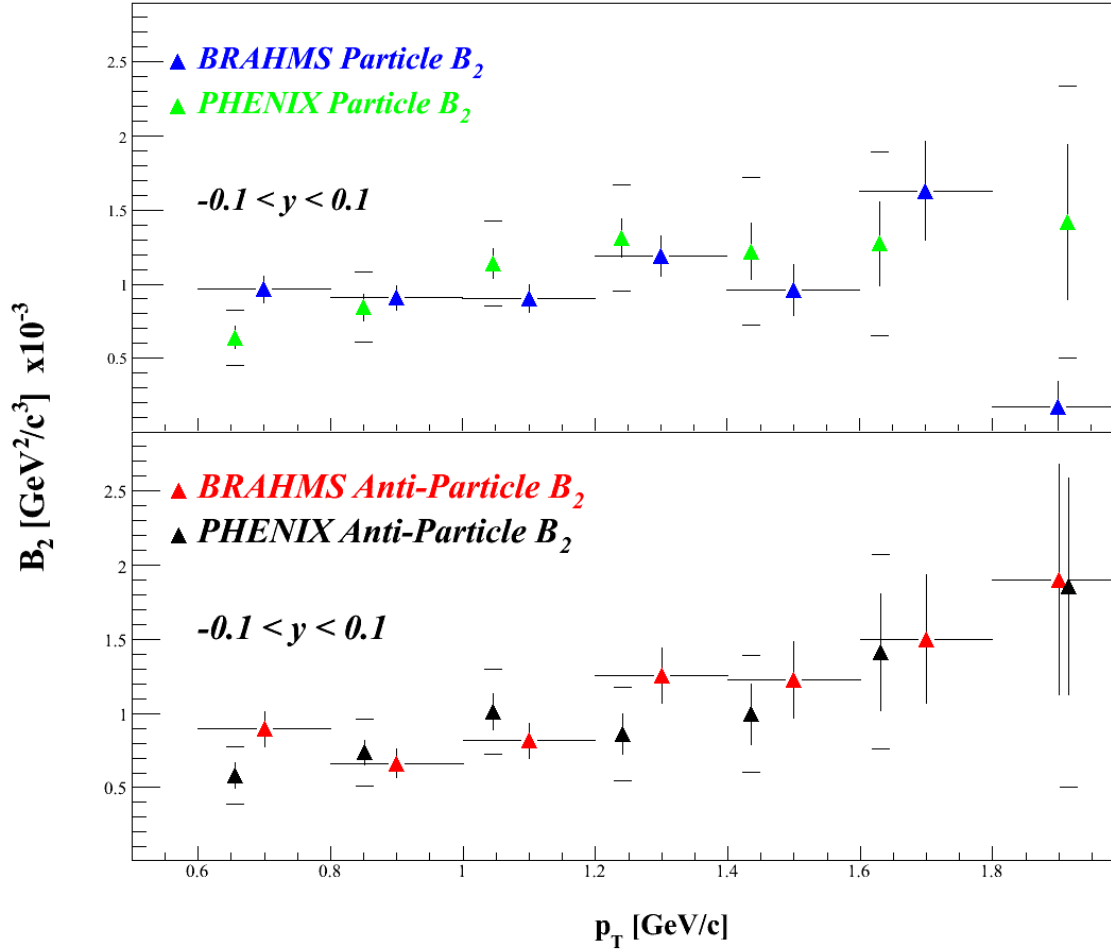
Figure 5.7: B_2 versus p_T comparisons between PHENIX and BRAHMS at $y \sim 0$. It is seen that there is good agreement between both particle and anti-particle measurements.

deuteron count, why no conclusions can be drawn based on it. For the anti-particles there is good agreement in this p_T-bin.

Next it is time to compare with others experiments at different energies. Fig. 5.8 shows the measured B_2 as a function of collision energy from several experiments. Added to the original plot is the results obtained in this work for $y \sim 0$. It is found that the coalescence parameter is decreasing as a function of collision energy pre-RHIC. Measurements from STAR ($\sqrt{s_{NN}} = 130\,\text{GeV}$) [69], PHENIX and now BRAHMS (both $\sqrt{s_{NN}} = 200\,\text{GeV}$) implies that this decrease is broken at RHIC energies. When interpreting B_2 as a measure of fireball volume, this implies that the dense collsion zone is of comparable size at RHIC and SPS.
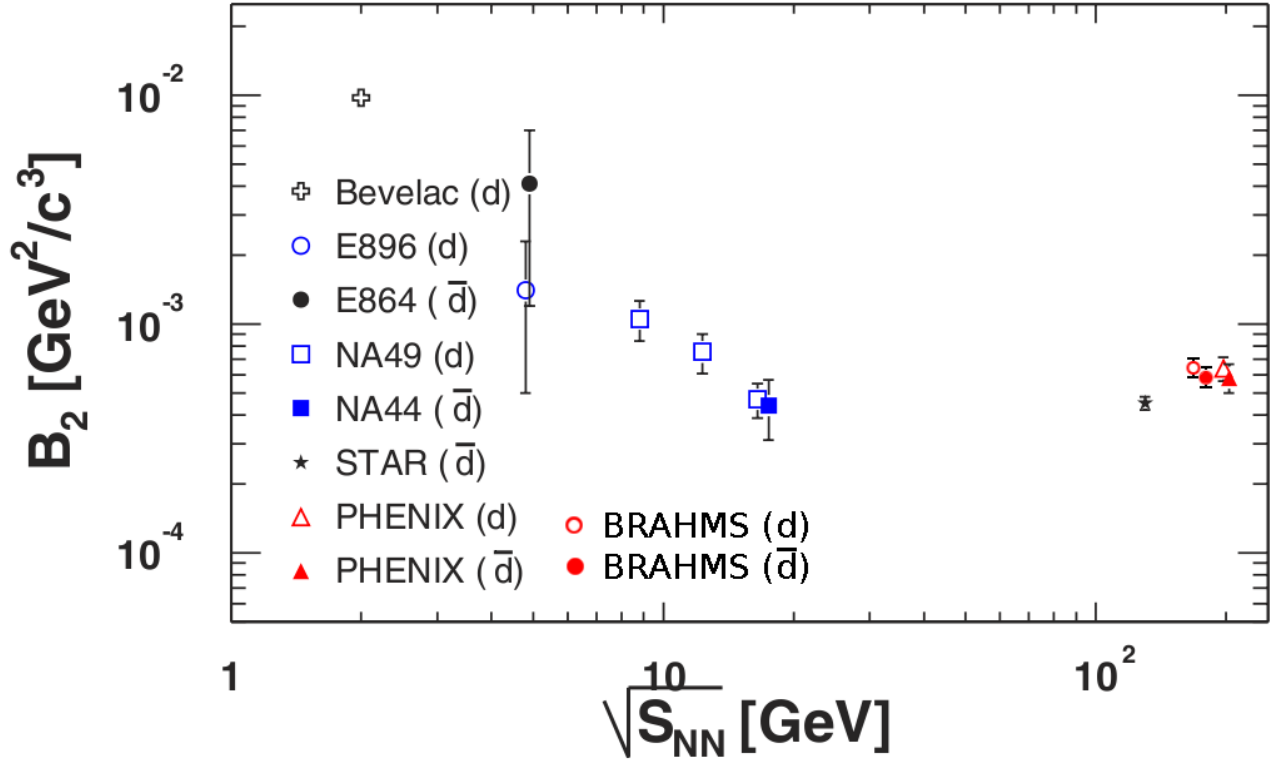
Figure 5.8: B_2 versus collision energy. The various data points are from [70, 36, 71, 72, 58, 69, 68] along with the addition of the results of this work. Figure taken from [68].

Polleri Model Revisited

As introduced in sec 2.4.1 the Polleri model can be compared to measured coalescence parameters. This can indicate the flow and density profiles of the collisions at hand. Unfortunately the calculations does not exist for $\sqrt{s_{NN}} = 200\,\text{GeV}$ why any detailed comparisons is not possible. However if one makes the (maybe naive) assumption that the form of the Polleri calculations presented in fig. 2.4 is preserved when going from SPS to RHIC energies, it might be possible to make some qualitative considerations.

Seeing that B_2 rises as a function of p_T suggests that the source density profile is not Gaussian. This is indeed true for a linear flow profile, where B_2 must be constant. For a square root profile B_2 rises a little. However it seems most probable that the best description is that of a box or surface profile. As with the E-802 data it would probably require a larger data set to estimate which flow profile is most suited (should it be possible to determine the density profile in the first place).

Rapidity interval	Radius (B_2)[fm]	Radius $(\bar{B}_2)$[fm]
-0.1$< y <$0.1	9.09 ± 0.42	9.46 ± 0.60
0.5$< y <$1.0	9.34 ± 0.24	9.26 ± 0.34
1.5$< y <$2.5	8.88 ± 1.17	-
3.0$< y <$3.2	8.64 ± 2.14	-

Table 5.3: Estimates of the fireball radius, derived from the measured coalescence parameters. It is assumed that the fireball is spherical.

5.5 Source Size Estimation

Using the thermal model described in sec. 2.2 one find that the fireball volume at the time of deuteron creation is given by eq. 2.12:

$$V = \frac{3}{2}\frac{(2\pi\hbar)^3}{m_p \cdot B_2} \tag{5.1}$$

where it is used that the deuteron total spin is +1, and the ratio between protons and neutrons are set to unity. Furthermore m_p and $\hbar = h/2\pi$ denotes the proton mass and the reduced Planck constant respectively.

Thus if a spherical fireball is assumed $(V = (4/3)\pi R^3)$ the radius, R, becomes:

$$R = \left(\frac{9}{8\pi}\frac{h^3}{m_p \cdot B_2}\right)^{(1/3)} \tag{5.2}$$

In this way the radius can be estimated. The radii derived for the B_2 values presented in sec. 5.3 is shown in tab. 5.5.

5.6 Outlook

The analysis presented in this thesis far from completes the necessary studies on deuteron coalescence. There is still lots of interesting and important work to be done in this field.

One interesting (and obvious) measurement to pursue in later works would be an analyis of B_2 as a function of centrality. This would hopefully shed more light on the theoretical connection between source size and fireball volume. It is expected that B_2 decreases for more central collisions (with more participants), as the overlapping region of the nuclei increases. This have been done by PHENIX in [68], who find that it is indeed the case. However more independent measurements are needed. To further delve into this topic doing B_2 versus collision system would most likely prove very interesting. BRAHMS have recorded Cu-Cu data recently, which have not been anyalysed as of yet in a coalescence perspective. Calculating B_2 for this system would give a fuller understanding of the connection between the number of participants and the measured coalescence parameter.

Furthermore more theoretical considerations are needed. As of yet Polleri simulations for $\sqrt{s_{NN}} = 200\,\text{GeV}$ does not exist. These would indeed be interesting to have. Hopefully they could yield insight into the flow and density profiles of heavy ion collisions.

Another thing which might prove useful is to further investigate the spectra fits; in particular the inverse slope parameter. As discussed in previously B_2 should be rising if the deuterons temperature is higher than the proton temperature. B_2 is indeed rising, however the extracted inverse slope parameter for the deuterons are not higher than for the protons everywhere. An explanation for this might be found in that fact that none of the fit functions describe the data perfectly. In addition the postulate that $T_d > T_p$ leads to B_2 rising assumes that the spectra are simple exponentials. Anyway it might prove useful to fully delve into this issue.

Chapter 6

Conclusion

In this work data from Au-Au collisions at $\sqrt{s_{NN}} = 200\,\text{GeV}$, recorded at BRAHMS, have been analysed. Invariant particle spectra of the 0-20% most central (anti-)protons and (anti-)deuterons have been presented for two mid-rapidity bins; $-0.1 < y < 0.1$ and $0.5 < y < 1.0$. Additionally invariant particle spectra of the 0-20% most central protons and deuterons have been presented for two forward rapidity bins; $1.5 < y < 2.5$ and $3.0 < y < 3.2$.

To obtain the spectra cuts have been applied to the events, requiring that they originate from close to the nominal interaction point and that there is coincidence between the vertex determination from the ZDC and BBCs. It has been required that the selected tracks are in fact stemming from the original collision and are matched well through the spectrometer, and that they do not get too close to the sides of the magnets. Furthermore particles have been identified using the TOF walls and the RICH for velocity determination, selecting protons and deuterons (and anti-protons and anti-deuterons). A number of corrections have been applied to the selected data, to account for geometrical acceptance, tracking efficiency, hadronic absorption, energy loss in the detectors, decays and multiple scattering.

The invariant spectra have been fit to several functions in order to estimate the extropolated invariant particle yield for each spectrum.

The invariant spectra have been used to construct the coalescence parameter as a function of p_T for all four rapidity bins. It was found that B_2 rises as a function of p_T for both particles and particles in the mid-rapidity bins, whereas the sparse statistics at forward rapidities does not allow for any conclusion in this regard.

Next the weighted average of each B_2 versus p_T distribution was presented. It was found that there is no rapidity dependency of B_2 within the uncertainties.

The obtained B_2 values were then corrected for hyperon weak decay, to allow for comparisons between data and other experiments. Here it was found that there is excellent agreement between PHENIX and BRAHMS in both the weighted average B_2 value and the measured B_2 versus p_T at mid-rapidity.

Comparisons was then done to previous deuteron coalescence results at different collision energies. It was shown that the decrease in B_2 for rising collision energies is seemingly broken at RHIC, where it seems to become constant for higher energies. Further investigations are needed to fully explain this phenomenon.

Using the obtained B_2 values it was attempted to make estimations of the source size, using the presented thermal coalescence model. It was found that, if a spherical fireball is assumed, the estimated radius of it is about $9\,\mathrm{fm}$ at the time of deuteron creation.

In regards to the density profile of the fireball it was found that, if the current model calculations are valid at $\sqrt{s_{NN}} = 200\,\mathrm{GeV}$, the density profile is unlikely to be Gaussian. Instead a box profile seems more in accordance with the obtained results.

Appendix A

The BRAHMS Collaboration

I C Arsene [11], I G Bearden[6], D Beavis[1], S Bekele[10], C Besliu[9], B Budick[5], H Bøggild[6],
C Chasman[1], C H Christensen[6], P Christensen[6], H H Dalsgaard[6], R Debbe[1],
J J Gaardhøje[6], K Hagel[7], H Ito[1], A Jipa[9], E B Johnson[10], C E Jørgensen[6], R Karabowicz[4],
N Katrynska[4], E J Kim[10], T M Larsen[6], J H Lee[1], S Lindahl[11], G Løvhøiden[11], Z Majka[4],
M J Murray[10], J Natowitz[7], B S Nielsen[6], C Nygaard[6], R Planeta[4], D Pal[10], F Rami[2],
C Ristea[6], O Ristea[9], D Röhrich[8], B H Samset[11], S J Sanders[10], R A Scheetz[1], P Staszel[4],
T S Tveter[11], F Videbæk[1] *(Spokesperson)*, R Wada[7], H Yang[8], Z Yin[8] and I S Zgura[3]

1 *Brookhaven National Laboratory, Upton, New York, USA*

2 *Institut Pluridisciplinaire Hubert Curien et Université Louis Pasteur, Strasbourg, France*

3 *Institute of Space Science,Bucharest-Magurele, Romania*

4 *M. Smoluchkowski Inst. of Physics, Jagiellonian University, Krakow, Poland*

5 *New York University, New York, USA*

6 *Niels Bohr Institute, University of Copenhagen, Copenhagen, Denmark*

7 *Texas A&M University, College Station, Texas, USA*

8 *University of Bergen, Department of Physics and Technology, Bergen, Norway*

9 *University of Bucharest, Romania*

10 *University of Kansas, Lawrence, Kansas, USA*

11 *University of Oslo, Department of Physics, Oslo, Norway*

Appendix B

Acronyms

The world of heavy ion physics is a world full of abbreviations. In the following a complete list of acronyms used in this work is presented.

AGS Alternating Gradient Synchroton

BBC Beam Beam Counter

BNL Brookhaven National Laboratory

BRAHMS Broad RAnge Hadron Magnetic Spectrometer

BRAG BRahms Analysis GEANT

CERN Conseil Européen pour la Recherche Nucléaire or European Organization for Nuclear Research

DST Data Summary Tree

D1-D5 Dipole magnet 1-5

DAQ Data AcQuisition

DC Drift Chamber

FS Forward Spectrometer

FFS Front Forward Spectrometer

FWHM Full Width Half Maximum

GEANT GEometry ANd Tracking

H1 / H2 TOF walls in the FS

HEHI High Energy Heavy Ion (group at NBI)

HIJING Heavy Ion Jet INteraction Generator

IP Interaction Point

lQCD lattice Quantum Chromo Dynamics

LEP Large Electron Positron (collider)

MA Multiplicity Array

MRS Mid Rapidity Spectrometer

NA49 North Area 49 (experiment at the SPS accelerator)

NBI Niels Bohr Institute

PHENIX Pioneering High Energy Nuclear Interaction eXperiment (one of the big RHIC experiments)

PHOBOS No acronym (small RHIC experiment)

PID Particle IDentification

pQCD pertubative QCD

QCD Quantum Chromo Dynamics

QED Quantum Electro Dynamics

QGP Quark Gluon Plasma

RHIC Relativistic Heavy Ion Collider

RICH Ring Imaging CHerenkov

ROOT ROOT's Object Oriented Technologies

SPS Super Proton Synchroton

STAR Solenoid Tracker At RHIC

TOF Time-Of-Flight

TPC Time Projection Chamber

ZDC Zero Degree Calorimeter

Appendix C

Alternative Fit Functions

This appendix presents the results of fitting spectra to a Boltzman in m_T (tab. C.1) and a Gaussian in p_T (tab. C.2) respectively.

Rapidity interval	Part.	Fit range [Gev/c]	Extrapolated yield	Inverse slope parameter (T)	χ^2/ndf
$-0.1 < y < 0.1$	p	$1.0 < p_T < 4.0$	22.0 ± 0.1	296.7 ± 0.7	$271/118$
	$\bar{p}$	$1.0 < p_T < 4.0$	16.5 ± 0.1	294.1 ± 0.8	$307/118$
	d	$1.0 < p_T < 4.0$	0.099 ± 0.005	273.0 ± 8.6	$25/10$
	$\bar{d}$	$1.0 < p_T < 4.0$	0.047 ± 0.003	318.3 ± 19.0	$29/10$
$0.5 < y < 1.0$	p	$1.0 < p_T < 3.5$	19.9 ± 0.05	298.2 ± 0.4	$651/98$
	$\bar{p}$	$1.0 < p_T < 3.5$	14.1 ± 0.05	296.6 ± 0.6	$590/98$
	d	$1.0 < p_T < 4.0$	0.077 ± 0.002	318.9 ± 8.3	$17/9$
	$\bar{d}$	$1.0 < p_T < 4.0$	0.043 ± 0.002	259.9 ± 7.2	$82/10$
$1.5 < y < 2.5$	p	$0.6 < p_T < 1.2$	17.2 ± 0.2	316.8 ± 8.7	$27/10$
	d	$1.0 < p_T < 3.5$	0.074 ± 0.010	350.0 ± 70.4	$2.8/3$
$3.0 < y < 3.2$	p	$1.0 < p_T < 3.0$	19.5 ± 0.2	221.6 ± 1.0	$109/38$
	d	$2.2 < p_T < 3.6$	0.045 ± 0.028	410.2 ± 274.5	$0.46/1$

Table C.1: Overview over fit results for all spectra. The fit function used is a boltzman in m_T.

97

Rapidity interval	Part.	Fit range [Gev/c]	Extrapolated yield	Inverse slope parameter (T)	χ^2/ndf
$-0.1 < y < 0.1$	p	$1.0 < p_T < 4.0$	17.9 ± 0.1	846.0 ± 1.6	$1325/118$
	$\bar{p}$	$1.0 < p_T < 4.0$	13.3 ± 0.1	845.8 ± 1.8	$863/118$
	d	$1.0 < p_T < 4.0$	0.096 ± 0.005	1124.4 ± 20.9	$18/10$
	$\bar{d}$	$1.0 < p_T < 4.0$	0.045 ± 0.003	1220.7 ± 42.7	$31/10$
$0.5 < y < 1.0$	p	$1.0 < p_T < 3.5$	16.7 ± 0.04	831.8 ± 1.0	$3153/98$
	$\bar{p}$	$1.0 < p_T < 3.5$	11.8 ± 0.04	829.3 ± 1.2	$2728/98$
	d	$1.0 < p_T < 4.0$	0.074 ± 0.002	1204.6 ± 18.2	$24/9$
	$\bar{d}$	$1.0 < p_T < 4.0$	0.041 ± 0.002	1083.0 ± 18.7	$81/10$
$1.5 < y < 2.5$	p	$0.6 < p_T < 1.2$	15.6 ± 0.2	744.8 ± 15.6	$30/10$
	d	$1.0 < p_T < 3.5$	0.072 ± 0.010	1239.0 ± 134.4	$2.9/3$
$3.0 < y < 3.2$	p	$1.0 < p_T < 3.0$	14.7 ± 0.2	689.2 ± 3.1	$117/38$
	d	$2.2 < p_T < 3.6$	0.041 ± 0.021	1440.1 ± 514.9	$0.5/1$

Table C.2: Overview over fit results for all spectra. The fit function used is a Gaussian in p_T.
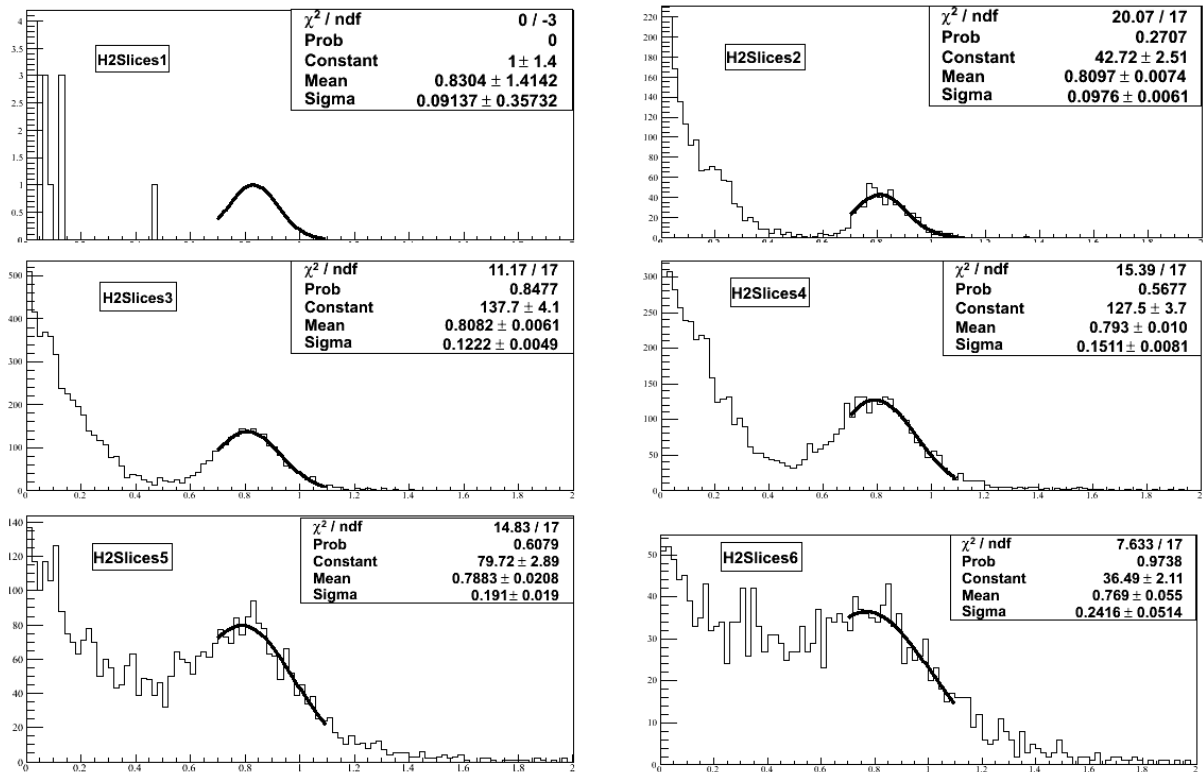
Appendix D

m^2 Widths for TOF PID

Figure D.1: The momentum slices for the H2 TOF wall in the setting 8B861, showing the m^2 distribution for each slice. The fit parameters can be seen for each slice. The momentum range of each slice can be deduced from its name by the following conversion; H2Slices[i]: $2 + i < p < 2 + (i + 1)$.

Getting the TOF PID m^2 width fit functions is done as described in the following. m^2

plots are made of five[12] equi-distant momentum slices as seen in fig. D.1. Each momentum slice is fitted to a Gaussian, whose widths are saved. Each width is then fit to eq. 4.5, which can be seen in fig. D.2. The obtained fit function is then used to select (anti-)protons.
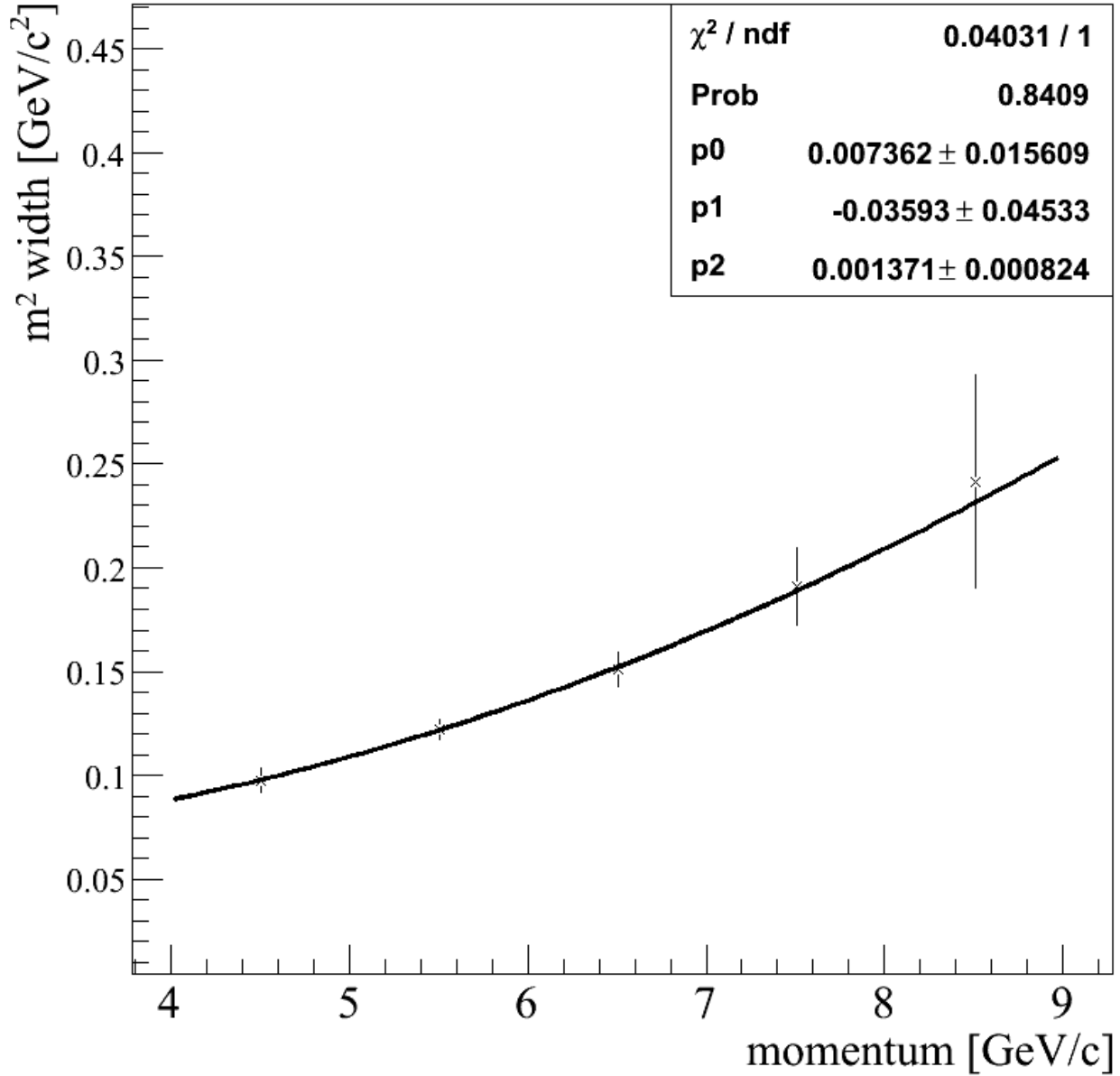

Figure D.2: The obtained width of each slice fitted to eq. 4.5.

---

[12]actually six slices are made, however the lowest p slice is empty

Appendix E

The Reaction Plane

In this appendix an illustration of the reaction plane is shown.

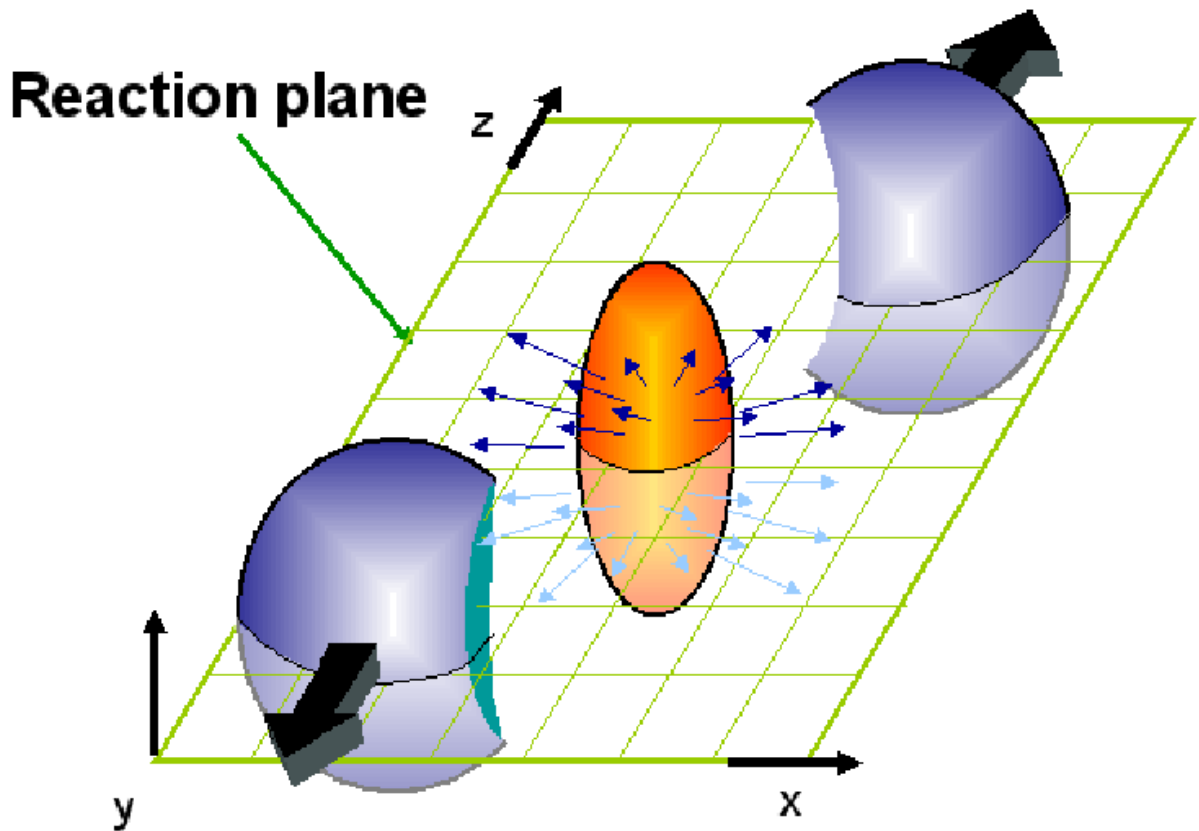Figure E.1: The reaction plane illustrated. Figure taken from [73].

Appendix F

Kinematics

In this appendix the kinematics of heavy ion collisions is described. To get a thorough description two reference frames are used, the laboratory frame and the center of mass frame. We label the center of mass variables with the subscript 'CM' and the laboratory frame with the subscript 'lab'. As the two reference frames coincide for a collider, e.g. RHIC, we will only use these labels in this appendix. Consider a system of two colliding particles with energies E_1 and E_2 and momenta p_1 and p_2 in the lab frame. For simplicity only one-dimensional collisions are considered. It is well known from the formalism of 4-vectors that the 4-momentum is conserved and that the square of the 4-momentum is invariant. Furthermore we have:

$$P_{lab} = (E_{lab}, \vec{p}_{lab}) = (E_{lab}, 0, 0, p_{lab})$$

$$P_{CM} = (E_{CM}, 0, 0, 0)$$

Thus by evaluating the total 4-momentum of the system in the CM frame and the lab frame we get:

$$P_{CM}^2 = P_{lab}^2 \Leftrightarrow E_{CM}^2 = E_{lab}^2 - p_{lab}^2 \tag{F.1}$$

By defining $s_{NN} \equiv E_{CM}^2$ and inserting the total energy and momentum of the system we get:

$$\sqrt{s_{NN}} = \sqrt{E_{lab}^2 - p_{lab}^2} = \sqrt{(E_1 + E_2)^2 - (p_1 + p_2)^2} \tag{F.2}$$

In an accelerator system where an incoming beam of particles hits a stationary target this reduces to (assuming the mass of the particles in the beam is equal to the mass of the particles in the target) :

$$\sqrt{s_{NN}} = \sqrt{2m(E_{beam} + m)} = \sqrt{\frac{2m}{\sqrt{1 - (tanh(y_p))^2}}} \tag{F.3}$$

Here y_p is the beam rapidity. For the collider system, where $p_1 \equiv -p_2$, we obtain the simple expression:

$$\sqrt{s_{NN}} = 2E_{beam} = 2m(\frac{1}{\sqrt{1 - (tanh(y_p))^2}} - 1) \tag{F.4}$$

Our main interest in the report is the central rapidity region where $y \approx 0$. Therefore the relevant energy to consider in this region is $\sqrt{s_{NN}}$ because the CM frame is the frame where

$y = 0$. Thus $\sqrt{s_{NN}}$ is the energy available for particle production in the central rapidity region. From this it is obvious why a collider is a far more powerful tool than an accelerator in unlocking the secrets of nature. The SPS, while using a beam of energy 158 GeV, only reaches $\sqrt{s_{NN}} = 17GeV$ whereas the RHIC utilising two 100 GeV beams is able to reach a whopping $\sqrt{s_{NN}} = 200GeV$.

Appendix G

The Glauber Model

In the Glauber model three assumptions are made [7]:

1. Nucleons are distributed according to a density function (e.g. Woods Saxon).

2. Nucleons travel in straight lines and are not deflected by interactions.

3. Nucleons interact with the inelastic cross section σ_{NN} measured in p+p collisions at the same initial energy even after multiple interactions.

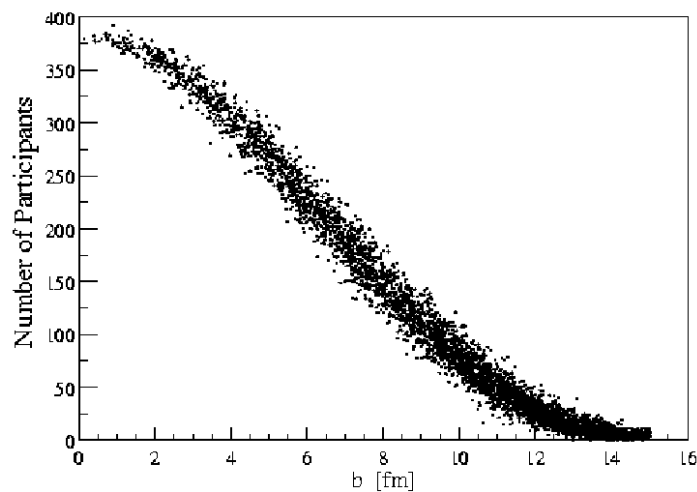Presented in fig. G.1 is the correlation between N_{part} and b in Au + Au collsions, based on the Glauber model.

Figure G.1: N_{part} versus impact parameter using the Glauber model. Picture taken from [52].

G.1 Lorentz Invariance of dy

The Lorentz transformation is given by:

$$
\begin{aligned}
E* &= \gamma E - \gamma \beta p_z \\
p_z* &= -\gamma \beta E + \gamma p_z
\end{aligned}
\tag{G.1}
$$

Here β velocity of the frame from which we view the collision and γ is defined as $\gamma = \frac{1}{\sqrt{1-\beta^2)}}$

The transformation is done by inserting the transformations of E and p_z into the definition of the rapidity:

$$
\begin{aligned}
y* &= \frac{1}{2}ln\frac{E*+p_z*}{E*-p_z*} \\
&= \frac{1}{2}ln\frac{\gamma E - \gamma \beta p_z - \gamma \beta E + \gamma p_z}{\gamma E - \gamma \beta p_z + \gamma \beta E - \gamma p_z} \\
&= \frac{1}{2}ln\frac{E+p_z}{E*-p_z} + \frac{1}{2}ln\frac{\gamma - \gamma \beta}{\gamma + \gamma \beta} \\
&= y + \frac{1}{2}ln\frac{\gamma - \gamma \beta}{\gamma + \gamma \beta}
\end{aligned}
\tag{G.2}
$$

$$
\tag{G.3}
$$

This means that:

$$
dy* = y*_2 - y*_1 = y_2 - y_1 = dy
\tag{G.4}
$$

Thus rapidity differences are Lorentz invariant.

Bibliography

[1] M. Kaku, Hyperspace, Oxford University Press, 1995, p.263.

[2] J. .M. Crespo *et al.* (ALEPH Collaboration), Phys. Lett. **B235**, 399-411, 1990.

[3] S. Eidelman *et al.*, Phys. Lett. **B592**, 1 (2004).

[4] J. Schwinger (editor), Selected Papers on Quantum Electrodynamics, Dover Publications, 1958.

[5] F. Halzen and A. D. Martin, Quarks and Leptons: An Introductory Course in Modern Particle Physics, John Wiley & Sons, Inc., 1984.

[6] M. E. Peskin and D. V. Scroeder, An Introduction to Quantum Field Theory, Westview Press, 1995.

[7] P. H. L. Christiansen, Stopping in central $\sqrt{s_{NN}} = 200\,\mathrm{GeV}$ Au+Au Collisions at RHIC, Ph.D dissertation, Niels Bohr Institute, 2003.

[8] B. Povh, K. Rith, C. Scholz and F. Zetsche, Particles and Nuclei, 4th edition, Springer-Verlag.

[9] T. R. Klassen, Phys. Rev. **D51** (1995) 5130.

[10] C. O. E. Jørgensen, Charged Particle Production in Au+Au Collisions at $\sqrt{s_{NN}} = 130\,\mathrm{GeV}$, Master thesis, University of Copenhagen, 2001.

[11] I. Arsene *et al.* (BRAHMS collaboration), Nucl.Phys. **A757** (2005).

[12] Z.Fodor and S.D. Katz, JHEP 0203, 014 (2002).

[13] J. Letessier and J. Rafelski, Camb. Monogr. Part. Phys. Nucl. Phys. Cosmol., **18**, 1-397, 2002.

[14] K. S. Krane, Introductory Nuclear Physics, John Wiley % Sons, Inc., 1988.

[15] J. D. Bjorken, Phys. Rev. **D27** (1983) 140.

[16] J. Jia, High-p_T Charged Hadron Suppression in $Au - Au$ Collisions at $\sqrt{s_{NN}} = 200\,\mathrm{GeV}$, Ph.D. dissertation, State University of New York at Stony Brook, 2003.

[17] L. D. Landau, Izv. Akad. Nauk. SSSR Ser. Fiz. **17**, 51-54, 1953.

[18] I. Arsene *et al.* (BRAHMS Collaboration), Phys. Rev. Lett. **91**, 072305, 2003.

[19] B. Sahlmueller (for the PHENIX Collaboration), Quark Matter 2006 proceedings.

[20] C. Adler *et al.* (STAR Collaboration), Phys. Rev. Lett. **90**, 082302, 2003.

[21] J. Adams *et al.* (STAR Collaboration), Phys. Rev. Lett. **91**, 072304, 2003.

[22] J. Adams *et al.* (STAR Collaboration), Nucl. Phys. **A757**, 1-2, 102-183, 2005.

[23] A. G. Hansen, Light Nuclei Production in Ultra Relativistic Heavy Ion Collisions, Ph.D. dissertation, University of Copenhagen, 1999.

[24] S. Voloshin and Y. Zhang, Z. Phys. **C70**, 665-672, 1996.

[25] C. O. E. Jørgensen, High p_T Charged Hadron Production at RHIC, Ph.D dissertation, Niels Bohr Institute, 2004.

[26] A. Adare *et al.* (PHENIX Collaboration), Phys. Rev. Lett. **98**, 162301, 2007.

[27] B. B. Back *et al.* (PHOBOS Collaboration), Nucl. Phys. **A757**, 1-2, 28-101, 2005.

[28] P. F. Kolb and U. W Heinz, nucl-th/0305084.

[29] O. Barannikova *et al.* (STAR Collaboration), nucl-ex/0403014.

[30] F. Videbaek and O. Hansen, Phys. Rev. **C52**, 2684, 1995.

[31] I. G. Bearden *et al.* (BRAHMS Collaboration), Phys. Rev. Lett. **93**, 102301, 2004.

[32] H. .H. Dalsgaard and C. Nygaard, Nuclear Stopping in Central $\sqrt{s_{NN}} = 62.4\,\mathrm{GeV}$ Au-Au Collisions at RHIC, University of Copenhagen, 2006.

[33] S. T. Butler and C. A. Pearson, Phys. Rev. **129**, (1963) 836.

[34] A. Schwarzschild and C. Zupancic, Phys. Rev. **129** (1963)854.

[35] L. P. Csernai and J. I. Kapusta, Phys. Rept. **131** (1986) 223-318.

[36] T. A. Armstrong *et al.* (E864 Collaboration), Phys. Rev. Lett. **85**, 2685-2688, 2000.

[37] R. Bond, P. J. Johansen, S. E. Koonin and S. Garpman, Phys. Lett. **71B**, 43-47, 1977.

[38] S. Das Gupta and A. Z. Mekjian, Phys. Rep. **72**, 131-183, 1981.

[39] H. Sato and K. Yazaki, Phys. Lett. **98B**, 153-157, 1981.

[40] A. Polleri, Probing Collective Effects in Heavy Ion Collisions by Nucleon Coalescence at Freeze-out, Ph.D. dissertation, University of Copenhagen, 1999.

[41] I. G. Bearden *et al.* (NA44 Collaboration), Phys. Rev. Lett. **78**,2080 (1997).

[42] M. Germinario, Deuteron and anti-Deuteron Coalescence in Au+Au Collisions at $\sqrt{s_{NN}} = 200\,\text{GeV}$, Master thesis, University of Copenhagen, 2003.

[43] T. Abbott *et al.*, (E802 Collaboration), Phys. Rev. **C50**, 1024, (1994).

[44] H. Hahn *et al.*, Nucl. Inst. Meth. **A499**, 245 (2003).

[45] K. H. Ackermann *et al.* (STAR Collaboration), Nucl. Inst. Meth. **A499**, 624-632 (2003).

[46] K. Adcox *et al.* (PHENIX Collaboration), Nucl. Inst. Meth. **A499**, 469-479 (2003).

[47] B. B. Back *et al.* (PHOBOS Collaboration), Nucl. Inst. Meth. **A499**, 603-623 (2003).

[48] M. Adamczyk *et al.* (BRAHMS Collaboration), Nucl. Inst. Meth. **A499**, 437-468 (2003).

[49] R. Debbe *et al.*, Nucl. Inst. Meth., **A371** ,(1996) 327-329.

[50] R. Karobowicz, Study of Nuclear Modification Factor in Au-Au Collisions at $\sqrt{s_{NN}} = 200\,\text{GeV}$, Ph.D dissertation, Jagiellonian University, 2006.

[51] H. Ito, Charged Particle Production in Au-Au Collisions at $\sqrt{s_{NN}} = 130\,\text{GeV}$ and $\sqrt{s_{NN}} = 200\,\text{GeV}$, Ph.D dissertation, University of Kansas, 2002.

[52] D. Ouerdane, Charged Pion and Kaon Production in Central Au+Au Collisions at $\sqrt{s_{NN}} = 200\,\text{GeV}$, Ph.D dissertation, Niels Bohr Institute, 2003.

[53] C. adler *et al.*, Nucl. Inst. Meth. **A470**, 488 (2001).

[54] Official ROOT webpage (http://root.cern.ch).

[55] I. G. Bearden *et al.* (BRAHMS Collaboration), Phys. Lett. **B523**, 227-233, 2001.

[56] T. M. Larsen, (title not finally decided yet), Ph.D. dissertation, University of Copenhagen, 2007.

[57] Official GEANT webpage (http://wwwasd.web.cern.ch/wwwasd/geant/)

[58] I. G. Bearden *et al.* (NA44 Collaboration), Nucl. Phys. **A661**, 387c-390c, 1999.

[59] Official HIJING webpage (http://www-nsdth.lbl.gov/ xnwang/hijing).

[60] S. S. Adler *et al.* (PHENIX Collaboration), Phys.Rev. **C69**, 034909, 2004.

[61] X. N. Wang and M. Gyulassy, Phys. Rev. **D44**, 3501, 1991.

[62] K. Adcox *et al.* (PHENIX Collaboration), Phys. Rev. Lett. **89**, 092302, 2002.

[63] J. Adams *et al.* (STAR Collaboration), Phys. Rev. Lett. **92** (2004) 112301.

[64] J. Adams *et al.* (STAR Collaboration), Phys. Rev. Lett. **98** (2007) 062301.

[65] W. Broniowski and W. Florkowski, Phys. Rev. **C65**, 064905, (2002).

[66] M. F. Gammeltoft, Master Thesis, University of Copenhagen, 2002.

[67] P. R. Bevingtion and D. K. Robinson, Data Reduction and Error Analysis for the Physical Sciences, 2nd ed., McGraw-Hill, Inc., 1992.

[68] S. S. Adler *et al.* (PHENIX Collaboration), Phys. Rev. Lett. **94** (2005) 122302.

[69] C. Adler *et al.* (STAR Collaboration), Phys. Rev. Lett. **87**, 262301, 2001.

[70] S. Wang *et al.*, Phys. Rev. Lett. **74**, 2646, 1995.

[71] S. Albergo *et al.* (E896 Collaboration), Phys. Rev. **C65**, 034907, 2002.

[72] T. Anticic *et al.* (NA49 Collaboration), Phys. Rev. **C69**, 024902, 2004.

[73] J. Hamblen, Presentation from talk given at DNP 2004, 2004.